Diss. ETH No. 18258

EARTHQUAKE SOURCE IMAGING USING A BAYESIAN APPROACH TO UNCERTAINTY ESTIMATION

A dissertation submitted to

ETH ZURICH

for the degree of

DOCTOR OF SCIENCES

presented by

DAMIANO MONELLI

Laurea in Fisica,

Universita' degli Studi di Bologna

born July 7, 1981

citizen of Italy

accepted on the recommendation of

Prof. Dr. Domenico Giardini, examiner

Dr. P. Martin Mai, co-examiner

Dr. Sigurjon Jónsson, co-examiner

Dr. Massimo Cocco, co-examiner

2009

a Giuseppe.

Contents

Riassunto

In questa tesi si presenta un metodo per la stima dei parametri di rottura cinematici di un terremoto attraverso l'inversione di dati di spostamento del suolo basato su di un approccio di tipo Bayesiano. Attraverso l'utilizzo di un approccio Bayesiano il metodo e' in grado di fornire stime complete delle incertezze sui parametri di rottura. La capacita' di quantificare la risoluzione dei parametri di rottura risponde alla richiesta di quantificare la non unicita' delle stime dei parametri di rottura. Infatti i modelli di rottura per uno stesso terremoto, sviluppati da ricerche indipendenti, mostrano spesso grandi differenze. Parte di questa variabilita' e' certamente dovuta a differenze nella modellazione e nella strategia di inversione dei dati. Tuttavia ragioni intrinseche limitano la capacita' di ricostruire il processo di rottura di un terremoto a partire dai dati osservati: incertezze presenti sia nella modellazione che nei dati e mancanza di risoluzione dovuta all'utilizzo di un numero sempre finito di osservazioni. Il lavoro presentato in questa tesi e' indirizzato alla comprensione di quanto questi fattori intrinsechi limitino la capacita' di stimare i parametri di rottura cinematici di un terremoto e come queste incertezze possano influire sulla stima dei corrispondenti parametri dinamici.

Si presenta il metodo considerando inizialmente un test sintetico. Attraverso l'inversione di dati *strong motion* generati da un modello di rottura cinematico di una faglia, si prova esplicitamente come diversi ulteriori modelli siano in grado di riprodurre i dati generati dal modello *vero*, mostrando chiaramente la necessita' di una quantificazione rigorosa delle incertezze sui parametri di rottura. Si confrontano inoltre le stime delle incertezze ottenute attraverso l'approccio Bayesiano con quelle ottenute utilizzando solamente un algoritmo di ottimizzazione. Si mostra come i due metodi diano sistematicamente stime diverse, e in particolare come l'algoritmo di ottimizzazione sottostimi le incertezze reali.

Si considera successivamente un caso reale, il terremoto di Western Tottori avvenuto nel 2000 in Giappone. Questo evento offre condizioni favorevoli per l'osservazione del processo di rottura, grazie all'abbondanza di dati di alta-qualita' di tipo strong motion e GPS nel campo vicino.

Inferenze sui parametri cinematici di rottura mostrano una zona ad alto scorrimento localizzata tra l'ipocentro e il bordo superiore della faglia. Questa asperita' e' stata identificata da tutti gli studi precedenti. A differenza di alcuni studi precedenti non si identifica tuttavia scorrimento significativo alla base della faglia. Inferenze ottenute utilizzando dati strong motion e strong motion+GPS confermano entrambe la presenza di un'asperita' superficiale. Nelle altre regioni della faglia si osserva

che l'aggiunta di dati GPS riduce la probabilita' associata ad alti valori di slip. In altre parole, i dati GPS aiutano a ridurre la presenza di scorrimento spurio, cioe' non vincolato dai dati strong motion. Questa riduzione ha un forte effetto sulla stima del momento sismico.

Si analizza inoltre l'effetto delle incertezze sui parametri cinematici sulla stima dei parametri dinamici. Considerando il terremoto di Tottori, si stima l'incertezza su parametri dinamici quali la caduta di sforzo statica, lo sforzo di taglio e l'energia sismica irradiata. Si osserva che in corrispondenza di alti valori di scorrimento, la distribuzione dei valori di caduta di sforzo assume una distribuzione di tipo Gaussiano con valori medi positivi, indicando percio' un indebolimento della faglia. I valori di deviazione standard sono tuttavia dello stesso ordine di grandezza dei valori medi, indicando percio' grandi incertezze sulla stima della caduta di sforzo. Si mostra come tali incertezze siano dovute ad un'anti-correlazione tra valori di caduta di sforzo in punti vicini della faglia, la quale a sua volta e' dovuta ad un'anti-correlazione tra i corrispondenti valori di scorrimento. Si mostra cosi' come una correlazione tra parametri cinematici limiti la precisione sulla misura di parametri dinamici. Nonostante la bassa precisione nella stima di parametri di rottura locali, si mostra invece come la misura di parametri di rottura globali, quali l'energia irradiata, sia caratterizzata da una maggiore precisione.

Si deriva infine un modello dinamico del processo di rottura per il terremoto di Tottori. Assumendo una legge costitutiva di tipo *linear slip-weakening*, si stimano i corrispondenti parametri dal campo di sforzo generato sulla faglia dal modello cinematico medio, in cui l'evoluzione temporale della velocita' di scorrimento viene assunta seguire la funzione regolarizzata di Yoffe. Il modello dinamico ottenuto e' in grado di spiegare i parametri cinematici stimati e di riprodurre lo spostamento del suolo osservato ad un livello confrontabile con quello prodotto dal modello cinematico ottimale. Si considera quest'ultimo risultato di particolare utilita' pratica, poiche' il modello dinamico e' stato ricavato senza utilizzare una particolare procedura di ottimizzazione, ma piuttosto interpretando un modello cinematico medio per mezzo di una funzione sorgente consistente con un modello di rottura dinamica.

Abstract

In this thesis I present a method for the estimation of kinematic earthquake rupture parameters based on a Bayesian approach through fitting of ground motion data. By using a Bayesian approach the method can provide comprehensive estimates of rupture parameters uncertainties. The capability of the method to quantify rupture parameters resolution responds to the quest for quantifying the non-uniqueness of rupture parameters estimates. Indeed, earthquake source images developed by different research teams for the same earthquake often show large differences. Part of this variability is certaintly due to different modeling and parameter estimation approaches. However, intrinsic reasons limit the imaging of earthquake source: uncertainties in both data and modeling, and lack of resolution due to the use of finite data-sets. The work presented in this thesis aims at understanding how much these intrinsic factors limit our ability in estimating kinematic earthquake rupture parameters and how much these uncertainties may affect also the estimation of dynamic rupture parameters.

I present the methodology by considering initially a synthetic test. By fitting strong motion waveforms generated by a synthetic kinematic fault rupture I show explicitly how multiple models may produce very similar level of fit, proving clearly the need for a rigorous quantification of the parameter uncertainties to assess model robustness. I also compare uncertainty estimates given by the Bayesian approach with those derived by using only an optmization algorithm. I show how the two methods give sistematically different results, with the optimization algorithm underestimating the actual uncertainties.

I then consider a real event: the 2000 Western Tottori (Japan) earthquake. Thanks to the abundance of high-quality near-field strong motion and GPS data, this event provides favorable conditions for the observation of the earthquake rupture process.

Inferences on kinematic parameters show that the best resolved feature of the rupture process is a major slip patch located between the hypocenter and the top edge of the fault. The presence of this shallow slip patch is common to all previous studies. In contrast to previous works I do not identify any significant slip at the bottom of the fault. I compare inferences from both strong motion and GPS data with results based on strong motion data only. In both cases the shallow slip patch is identified. At other locations, the main effect of GPS data is in reducing the probability associated with high values of slip. GPS data reduce the presence of spurious fault slip and therefore strongly influence the resulting final seismic moment.

Additionaly, I investigate how uncertainties in kinematic rupture parameters affect the estimation of dynamic parameters. Still considering the Tottori earthquake, I analyse resolution of static stress drop, shear stress, and radiated energy. I find that on the same locations where stable high slip is inferred, frequency distributions of static stress drop values have an approximately Gaussian shape with positive mean values, indicating that these locations undergo a weakening process on average. However, I find standard deviation values of the same order of magnitude of the estimated mean values indicating therefore large uncertainties in the actual intensity of static stress drop. I show how these large uncertainties are due to a correlation between stress drop values in neighbouring points of the fault which is inherited from a correlation between slip values. This shows how a correlation between kinematic parameters limits the resolution of dynamic parameters. Despite the difficulty in constraining the rupture process locally on the fault, I find that a global quantity like radiated energy can be well inferred.

I finally derive a dynamic rupture model for the 2000 Western Tottori earthquake by estimating linear slip-weakening parameters from the spatio-temporal evolution of on-fault stress generated by the mean kinematic slip model, in which the slip-velocity time history is assumed to follow a regularized Yoffe function. I obtain a dynamic model able to explain the observed kinematic parameters and that provides a level of fit with the observed strong motion and GPS data comparable to that of the best-fitting model. This last result should be considered of particular practical importance, because the dynamic model has been obtained without an explicit optimization procedure, but rather interpreting a mean slip model using a dynamically consistent source time function.

Introduction

The destructive power of large earthquakes is a significant threat in those regions of the Earth where active seimogenic sources are located near or within large populated areas. Seismic hazard must therefore be communicated to stimulate the adoption of preventive measures to reduce the harmful effects of strong ground shaking produced by large earthquakes. However, seismic hazard can be correctly estimated and improved only through a continuous scientific effort aimed at a quantitative understanding of the physical processes governing the Earth's seismicity.

Earthquakes are one of the many phenomena through which the Earth shows itself as a dynamically evolving system. Indeed, the Earth's interior interacts with the upper lithosphere and the transmitted stresses can cause the brittle parts of the Earth's crust to rupture dynamically, causing the emission of seismic waves. Seismicity can be therefore considered as the short-timescale phenomenon of brittle tectonics [Scholz, 2002].

Crustal earthquakes are therefore associated with the notion of dynamically propagating ruptures occuring in geological structures known as faults, which can be considered as "weak" zones of the Earth's crust. Although the theory of plate tectonics can explain well the spatial distribution of earthquakes in the Earth's crust, the physical processes governing the nucleation and propagation of the earthquake rupture are still far from being completely revealed and quantitatively understood. Indeed, the earthquake rupture is a complex phenomenon involving various non-linear dissipation processes coupled over a wide range of spatial and temporal scales. No theoretical solutions are available today for a physically consistent description of the earthquake rupture dynamics based on a accurate representation of the physics of dissipation processes occurring at different scales [Cocco & Tinti, 2008].

Earthquake source physics is therefore an active research field, where different approaches are required to investigate the multi-scale nature of the earthquake source. For instance, geological investigations can shed light into the structure of real fault zones, and on microscale processes and dynamic weakening mechanisms occuring during earthquake ruptures (Chester et al. [1993], Chester & Chester [1998], Wibberly & Shinamoto [2003]). However, geological investigations provide us with a "static" picture of the earthquake source, and no information is given about the "dynamics", that is the physical laws governing the spatio-temporal evolution of the earthquake rupture. A possible way to get insights into the dynamics of the earthquake source is through laboratory experiments mimicking shear ruptures in fault zones. Indeed, from laboratory experiments fault constitutive laws can be derived, that is, physical laws describing how the fault weakening occurs (Dieterich [1979], Ohnaka & Yamashita [1989], Beeler et al. [1994], Goldsby & Tullis [2002], Di Toro et al. [2004]). However, these constitutive laws are derived at a laboratory scale, and using experimental set-ups which only mimic real faults. Their validity in natural faults has to be proved.

To achieve a more complete understanding of the earthquake source, geological and laboratory-scale studies must be integrated with a seismological analysis, which is the only one that can provide observational constrains on the rupture process of real-Earth faults. The study of the earthquake source through the analysis of the radiated wavefield is usually indicated with the term “earthquake source imaging”. Indeed, by inversion of the observed ground motion generated by an earthquake, it is possible to derive rupture models which can be considered as images of the earthquake source.

A key point in all earthquake imaging studies is how the rupture process is parameterized. Geological investigations show that the most common type of crustal earthquakes is generated by a sudden slip in a “fault zone”. Field observations suggest that slip in individual events may be extremely localized, and may occur primarily within a thin shear zone, which is perhaps only <1-5 mm thick. This localized shear zone lies within a finely granulated fault core of typically tens to hundreds millimeter thickness. The core itself fits within a much broader damage zone of granulated or incompletely cracked rocks, perhaps several meters thick [Rice, 2006].

When using seismic and geodetic data to image the earthquake rupture, the “fault zone” is usually approximated with a “fault surface”, with no thickness. This because for most seismological applications the fault zone width is much less than the minimum considered wavelength. The main consequence of this approximation is that seismologically-derived quantities characterizing the rupture process should be considered in a macroscopic sense. For instance, slip should be interpreted as the relative displacement between the walls of the fault zone [Cocco et al., 2006].

Assuming the “fault surface” approximation, the earthquake source can be described from two points of view: kinematic and dynamic. In the kinematic approach the slip process is seen as a dislocation: that is a displacement discontinuity. In a kinematic model no source physics is invoked. On the contrary, in a dynamic model the slip process is seen as the result of a shear rupture. What controls the rupture is the friction law (the constitutive law), and the elastodynamics equations are solved for a given friction law on the fault surface.

Both kinematic and dynamic models are defined in terms of a number of parameters. In a kinematic model the dislocation process on each location on the fault surface must be defined. This is done usually in terms of maximum slip (or slip-velocity), rake angle (i.e. the slip direction), rise time (i.e. the slip duration), and rupture time (i.e. the slip onset time). In a dynamic model the basic required parameters are the initial applied stress, the yield stress (i.e. the static friction level which must be overcomed to rupture the fault), and the dynamic friction level (i.e. the stress value during fault sliding). Moreover, depending on the assumed friction law, additional parameters are required to describe the weakening process (e.g. the slip-weakening distance in a linear slip-weakening model).

Due to the large computational demand required by dynamic rupture simulations, most earthquake source imaging studies are performed assuming a kinematic model for the earthquake source. Within this approach, kinematic rupture parameters define the slip function on each location on the fault and relate with the observed ground motion through the representation theorem [Aki & Richards, 2002].

Although the slip vector is linearly related to the observed ground motion, the remaining parameters (rise time and rupture time) are not. Therefore, the kinematic imaging of the earthquake source is, in general, a non-linear inverse problem. Without the computational power needed to solve non-linear inverse problems, early studies assumed a priori values for rise time and rupture time on the fault surface, and solved only for the slip distribution by using the linear least-square method (Olson & Apsel [1982], Hartzell & Heaton [1983]). This methodology requires the inversion of the forward modeling operator. Because of uncertainties in both data and theory and limited data coverage, this is often an ill-posed and ill-conditioned problem (multiple solutions may exist due to the presence of a null space in the model space and small change in the data may lead to large variations in the parameter estimates). Damping parameters are therefore additionaly required in order to get a unique solution.

As already mentioned, relaxing the assumptions on rupture time and rise time render the inversion non-linear. Under these conditions a linearized inversion can be used to infer, together with slip, rupture time [Beroza & Spudich, 1988] and also rise time values [Cotton & Campillo, 1995]. The main drawback of this approach is that the inversion results depend on the starting model and, requiring the computation of the generalized inverse, damping parameters are again needed.

As computational resources improved, optimization methods like simulated annealing (Hartzell et al. [1996]; Bouchon et al. [2000]; Delouis et al. [2002]; Salichon et al. [2003]; Liu & Archuleta [2004]), neighbourhood [Vallee & Bouchon, 2004] and genetic [Emolo & Zollo, 2005] algorithms started to be adopted in earthquake source imaging studies. With such methods no assumptions on the objective function are made and good data-fitting models are found by directly searching the model space. Only the forward modeling operator is computed and no matrix inversion is needed (hence no damping parameters are required).

A key issue in any parameter-estimation technique is the assessment of uncertainties which affect the inferred model parameters. In linear or linearized least-square inversions the objective function is a quadratic function with a single minimum. Uncertainties on model parameters can be obtained by computing the curvature of this function around the minimum [Menke, 1989].

In non-linear inversions the structure of the objective function is actually unknown and it may presents multiple (and even degenerate valley-like) minima. Using optimization algorithms we can efficiently identify good data-fitting models but we cannot directly estimate uncertainties. For this purpose, some strategies have been recently proposed. Emolo & Zollo [2005] used a genetic algorithm to search the model space and estimated resolution by making a Gaussian approximation of the objective function around the best-fitting model. In this approach uncertainties are estimated only locally, in the neighbourhood of the best fitting model, forcing the objective function to be Gaussian around it. Other approaches estimate uncertainties by statistically analyzing the set of models visited during the search of the model space. From the set of models produced by a neighbourhood algorithm, Peyrat & Olsen [2004] selected 19 models that fit the data almost equally well, and then computed the standard deviation for each model parameter from this ensemble. Piatanesi et al. [2007] computed weighted mean and standard deviation for each model parameter considering the whole ensemble of models produced by a simulated annealing algorithm. The main limitation of these approaches is that they derive resolution estimates by statistically analyzing the ensemble (or sub-ensemble) of models produced by an optimization algorithm without taking into account that this ensemble does not reflect in general the actual uncertainties, that is the topology of the misfit function, but rather the operators adopted by the search algorithm. Moreover all these techniques assume uncertainties to be Gaussian, which is generally not true for non-linear problems.

Accurate estimates of uncertainties are needed in order to asses the reliability of the inverted solutions. As it has been pointed out by different authors (Cohee & Beroza [1994]; Beresnev [2003]; Ide et al. [2005]) and is also represented in the online database of earthquake rupture models (http://www.seismo.ethz.ch/srcmod), for the same earthquake, acceptable fit to the data can be provided by different rupture models. The discrepancies between models may be due to the different choices adopted during the inversion concerning the forward modeling, the model parametrization, the inversion methodology, the type of data set and processing used. However, independently of the particular approach, intrinsic reasons render imaging the earthquake source a problem with multiple solutions: uncertainties in data and in forward modeling (which allow multiple models to be considered acceptable) and lack of resolution (due to the always limited data coverage).

The quantification of uncertainties in kinematic rupture parameters is also important for assessing uncertainties in dynamic rupture parameters. Indeed, kinematic slip models derived from the inversion of ground motion data can be used to determine the spatio-temporal evolution of on-fault stress (e.g. Ide & Takeo [1997], Bouchon [1997], Dalguer et al. [2002], Tinti et al. [2005b]), and from that some estimates of dynamic parameters such as stress drop, strength excess (relative fracture strength), and linear slip-weakening distance (in the framework of slip weakening friction models). As already mentioned, multiple kinematic rupture models may satisfy the observations for a given earthquake and therefore uncertainties in kinematic parameters propagate into the estimation of dynamic parameters.

Kinematic and dynamic images of earthquake ruptures are used also for earthquake source physics studies (e.g. Mai & Beroza [2002], Tinti et al. [2005b], Woessner et al. [2006]), and for ground motion prediction of future earthquakes (Olsen et al. [2006], Olsen et al. [2008], Olsen et al. [2009]). Understanding what are the current limits in inferring kinematic and dynamic parameters is important therefore for constraining what can be learnt from seismic data about the earthquake source, and what can be the variability in ground motion prediction given the uncertainties in the definition of an earthquake rupture model.

Given that most earthquake imaging studies largely ignored or over-simplified the analysis of uncertainties, together with the importance of assessing the reliability of earthquake images, especially in view of their application in earthquake source physics studies and hazard estimates, the main goal of this thesis is the development of a methodology for the estimation of kinematic earthquake rupture parameters together with their associated uncertainties.

The methodology presented in this thesis in based on a Bayesian approach. With a Bayesian approach, inferences on model parameters are expressed in terms of marginal probability density functions (PDFs) derived from a "posterior" PDF, representing the conjunction of "prior" information on model parameters, and information derived through fitting observations. Resolution on each model parameter is investigated comparing prior and posterior marginal PDFs. By using a Bayesian approach, it is possible to overcome the main limitation of optmization based inversions, which can only identify good-data fitting models, but which cannot provide information on the actual resolution of model parameters. By expressing model parameters estimates in terms of PDFs, rather than by computing a single best-fitting model, or few good data-fitting models, it is possible to obtain a more robust understanding of which degree of detail a model can be interpreted, without drawing conclusions from unstable or unresolved features.

The general organization of the thesis is as follows:

In Chapter 1 I present the Bayesian inference method in the context of an earthquake source imaging problem. To avoid complexities arising from considering a real event, I study a synthetic kinematic fault rupture process. Data consist of strong motion waveforms only. I estimate kinematic rupture parameters by using a two step procedure. First, I explore the model space by using an evolutionary algorithm to identify good data fitting regions. Second, by using a neighbourhood algorithm and considering the entire ensemble of models found during the exploration stage, I compute a geometric approximation of the posterior probability density function that is used to generate a second ensemble of models from which Bayesian inference is performed.

I apply the Bayesian inference method to a real case in Chapter 2. I consider the 2000 Western Tottori earthquake. Data consist of strong motion waveforms and surface static offsets derived from GPS measurements. Bayesian inference is performed by using a Markov Chain Monte Carlo (MCMC) method, based on the Metropolis algorithm. I study how resolution of kinematic rupture parameters changes depending on two different data sets: strong motion only, and strong motion plus GPS.

From kinematic parameters it is possible to estimate dynamic parameters by solving the elastodynamics equation with the kinematic slip model as a boundary condition. In Chapter 3 I investigate how the estimation of dynamic parameters is affected by uncertainties in the kinematic source model. Still considering the 2000 Western Tottori earthquake, I map the uncertainties in kinematic parameters estimated in Chapter 2 into uncertainties in dynamic parameters. I quantify resolution of static stress drop, shear stress, and radiated energy.

In Chapter 4 I derive a dynamic rupture model for the 2000 Western Tottori earthquake aimed at explaining the most prominent features observed in kinematic images. By using a mean kinematic slip model, and a dynamically consistent source time function (regularized Yoffe function), I estimate linear slip-weakening parameters. I validate the obtained dynamic model by comparing the predicted ground motion with near-field strong motion and GPS data.

The thesis ends with a summary of the main findings, along with an outline of potential future research directions.

Chapter 1

Bayesian inference of kinematic earthquake rupture parameters through fitting of strong motion data

Published in Geophysical Journal International as:
Monelli, D., and Mai, P. M. (2008), Bayesian inference of kinematic earthquake rupture parameters through fitting of strong motion data, Geophys. J. Int., 173, 220-232

Abstract

Due to uncertainties in data and in forward modeling, the inherent limitations in data coverage and the non-linearity of the governing equation, earthquake source imaging is a problem with multiple solutions. The multiplicity of solutions can be conveniently expressed using a Bayesian approach, which allows to state inferences on model parameters in terms of probability density functions. The estimation of the posterior state of information, expressing the combination of the a priori knowledge on model parameters with the information contained in the data, is achieved in two steps. First, we explore the model space using an evolutionary algorithm to identify good data fitting regions. Secondly, using a neighbourhood algorithm and considering the entire ensemble of models found during the search stage, we compute a geometric approximation of the true posterior that is used to generate a second ensemble of models from which Bayesian inference can be performed. We apply this methodology to infer kinematic parameters of a synthetic fault rupture through fitting of strong motion data. We show how multiple rupture models are able to reproduce the observed waveforms within the same level of fit, suggesting that the solution of the inversion cannot be expressed in terms of a single model but rather as a set of models which show certain statistical properties. For all model parameters we compute the posterior marginal distribution. We show how for some parameters the posterior does not follow a Gaussian distribution rendering the usual characterization in terms of mean value and standard deviation not correct. We compare the posterior marginal distributions with the 'raw' marginal distributions computed from the ensemble of models generated by the evolutionary algorithm. We show how they are systematically different proving therefore that the search algorithm we adopt cannot be directly used to estimate uncertainties. We also analyze the stability of our inferences comparing the posterior marginals computed by different independent ensembles. The solutions provided by independent explorations are similar but not identical because each ensemble searches the model space differently resulting in different reconstructed posteriors. Our study illustrates how uncertainty estimates derive from the topology of the objective function, and how accurate and reliable resolution analysis is limited by the intrinsic difficulty of mapping the 'true' structure of the objective function.

1.1 Introduction

Current earthquake source imaging studies use different data sets (strong motion, teleseimic, GPS, InSAR) and inference methods (linear or linearized data inversions, direct search techniques) to retrieve kinematic rupture parameters. A fault rupture can be described, kinematically, as a shear dislocation propagating along a surface within an elastic medium. Using seismic data the dislocation process at each point on the fault is usually parametrized in terms of slip (or slip-velocity), rake angle (direction of slip), rupture time (time at which the slip process starts) and rise time (duration of slip). These parameters enter in the slip function which in turn determines the ground motion through the representation theorem [Aki & Richards, 2002].

The mathematical parametrization of the slip function is not unique in inverse modeling studies, although the chosen functional form has important implications from the dynamic point of view. It determines in fact the traction evolution over the fault surface [Piatanesi et al., 2004]. Two main methods are used for representing the slip function: the multi-time window and the single time-window approach. In the former, the slip function is not prescribed a priori but is expanded into a number of basis functions (Olson & Apsel [1982]; Wald & Heaton [1994]; Ide et al. [1996]; Sekiguchi et al. [2000]; Delouis et al. [2002]; Salichon et al. [2003]). In the latter the slip function is forced to assume a predefined functional form, like a triangle [Hartzell & Heaton, 1983], a boxcar [Emolo & Zollo, 2005] or a more complex form involving, for instance, trigonometric [Hartzell et al., 1996] or power-law [Liu & Archuleta, 2004] functions.

Fixing, for each location on the fault, rise time and rupture time (for a multi time-window approach, rise time and rupture time for each basis function), the relation between slip and ground motion becomes linear. A solution can then be obtained using the linear least-square method (Olson & Apsel [1982]; Hartzell & Heaton [1983]; Wald et al. [1991]; Ide et al. [1996]; Sekiguchi et al. [2000]; Sekiguchi & Iwata [2002]). This methodology requires the inversion of the forward modeling operator. Because of uncertainties in both data and theory and limited data coverage, this is often an ill-posed and ill-conditioned problem (multiple solutions may exist due to the presence of a null space in the model space and small change in the data may lead to large variations in the parameter estimates). Damping parameters are therefore additionaly required in order to get a unique solution. Possible constrains are: moment minimization, smoothing of slip and filtering of singular values [Hartzell & Heaton, 1983].

Relaxing the assumptions on rupture time and rise time render the inversion non-linear. Under these conditions a linearized inversion can be used to infer, together with slip, rupture time [Beroza & Spudich, 1988] and also rise time values [Cotton & Campillo, 1995]. The main drawback of this approach is that the inversion results depend on the starting model and, requiring the computation of the generalized inverse, damping parameters are again needed.

As computational resources improved, optimization methods like simulated annealing (Hartzell et al. [1996]; Bouchon et al. [2000]; Delouis et al. [2002]; Salichon et al. [2003]; Liu & Archuleta [2004]), neighbourhood [Vallee & Bouchon, 2004] and genetic [Emolo & Zollo, 2005] algorithms started to be adopted in earthquake source imaging studies. With such methods no assumptions on the objective function are made and good data-fitting models are found by directly searching the model space. Only the forward modeling operator is computed and no matrix inversion is needed (hence no damping parameters are required). Despite these benefits, these randomized search techniques require a certain number of tuning parameters to guide the search, but no general theories are available that help to chose optimal values [Mosegaard & Sambridge, 2002]. Each problem often requires its own tuning parameters values. Moreover, even if some algorithms are guaranteed to converge to the global minimum (like some simulated annealing algorithms with certain cooling schedules, [Sen & Stoffa, 1995]), this convergence is only asymptotic, i.e. the true global minimum is found only after an infinite number of iterations. Practically, finite computational resources limit our ability in searching the model space so that the solution found can never be proved to be optimal.

A key issue in any parameter-estimation technique is the assessment of uncertainties which affect the inferred model parameters. In linear or linearized least-square inversions the objective function is a quadratic function with a single minimum. Uncertainties on model parameters can be obtained by computing the curvature of this function around the minimum [Menke, 1989].

In non-linear inversions the structure of the objective function is actually unknown and it may presents multiple (and even degenerate valley-like) minima. Using optimization algorithms we can efficiently identify good data-fitting models but we cannot directly estimate uncertainties. For this purpose different strategies have been proposed. Emolo & Zollo [2005] used a genetic algorithm to search the model space and estimated resolution making a Gaussian approximation of the objective function around the best-fitting model. In this approach uncertainties are estimated only locally, in the neighbourhood of the best fitting model, forcing the objective function to be Gaussian around it. Other approaches estimate uncertainties by statistically analyzing the set of models visited during the search of the model space. From the set of models produced by a neighbourhood algorithm, Peyrat & Olsen [2004] selected 19 models that fit the data almost equally well, and then computed the standard deviation for each model parameter from this ensemble. Piatanesi et al. [2007] computed weighted mean and standard deviation for each model parameter considering the whole ensemble of models produced by a simulated annealing algorithm. The main limitation of these approaches is that they derive resolution estimates by statistically analyzing the ensemble (or sub-ensemble) of models produced by an optimization algorithm without taking into account that this ensemble does not reflect in general the actual uncertainties, that is the topology of the misfit function, but rather the operators adopted by the search algorithm. Moreover all these techniques assume uncertainties to be Gaussian, which is generally not true for non-linear problems.

The major goal of this paper is to estimate resolution on kinematic earthquake rupture parameters taking into account the full non-linearity of the problem, without invoking any approximation on the objective function and hence allowing for possible non-Gaussian uncertainties. We consider a synthetic test so that we can control uncertainties in data and in forward modeling. In order to express the multiplicity of the solutions we adopt a Bayesian approach [Tarantola, 2005]. Inferences on inverted parameters are derived from the posterior probability density function. It is obtained as the conjunction of "states of information" (expressed in terms of probability densities) reflecting our prior information on model parameters, data and their correlation (the physical law governing the forward modeling). We compute the posterior using the strategy proposed by Sambridge [1999]. First, using a direct search algorithm, we explore the model space to discover the structure of the posterior probability density function and to identify good data fitting regions. In this study we use an evolutionary algorithm [Beyer, 2001] to perform this task. Secondly, using a neighbourhood algorithm and considering the whole ensemble of models produced during the search stage, we compute a geometric approximation of the true posterior from which samples are generated and Bayesian inference performed. Hence, the solution we provide for each model parameter is stated in terms of a marginal probability density function from which uncertainty estimates can be derived.

1.2 The Bayesian approach

The general idea of a Bayesian approach to inverse theory is that a certain amount of information or knowledge about the physical system under investigation (represented by the model parameter vector $\mathbf{m}$) and the data ($\mathbf{d}$) is available before the inversion, and can be expressed in terms of a probability density function. Together with this 'a priori' knowledge, another source of information is given by the correlation between model parameters and data expressed by a physical law ($\mathbf{d} = \mathbf{g}(\mathbf{m})$). The solution of the inverse problem is then obtained by combining these two states of information. The main difficulty in computing the solution is in extracting information contained in the correlation between $\mathbf{d}$ and $\mathbf{m}$, in particular when $\mathbf{m}$ is defined in a large dimensional space and the forward modeling operator $\mathbf{g}$ is computationally expensive. Under these conditions computing the equation $\mathbf{d} = \mathbf{g}(\mathbf{m})$ on a regular grid of points in the model space is unfeasible and one is forced to use randomized techniques in order to evaluate the above equation in a limited number of points which should be representative of the most important regions of the model space (where the correlation between $\mathbf{d}$ and $\mathbf{m}$ is high). However, finite computation time and finite computing resources will always limit our ability in extracting this information. The consequence is that the solution of these types of inverse problems will be, for any realistic large scale problem, incomplete and always subject to a certain amount of variability that decreases as the exploration of the model space becomes more and more extensive.

1.2.1 The posterior state of information

In presenting the Bayesian approach, we follow the theoretical formulation of Tarantola [2005]. We assume the M-dimensional model space and D-dimensional data space, $\mathbb{M}$ and $\mathbb{D}$ respectively, to be linear spaces. Indicating with $\rho_M(\mathbf{m})$ and $\rho_D(\mathbf{d})$ the prior probability density functions on model parameters and data respectively, while with $\theta(\mathbf{d}|\mathbf{m})$ the conditional probability density representing the correlation between $\mathbf{d}$ and $\mathbf{m}$, the posterior state of information on the model space is given by:

$$\sigma_M(\mathbf{m}) = k\rho_M(\mathbf{m})L(\mathbf{m}) \tag{1.1}$$

where k is a normalization constant and $L(\mathbf{m})$ is the likelihood function:

$$L(\mathbf{m}) = \int_{\mathbb{D}} d\mathbf{d}\, \rho_D(\mathbf{d})\theta(\mathbf{d}|\mathbf{m}) \tag{1.2}$$

Assuming that our a priori knowledge on model parameters consists of the only information that each model parameter is strictly bounded by two values m^{α}_{min} and m^{α}_{max}, where $\alpha \in I_M, I_M = \{1, ..., M\}$, we write:

$$\rho_M(\mathbf{m}) = \prod_{\alpha_M \in I_M} \rho_\alpha(m^\alpha) \tag{1.3}$$

where

$$\rho_\alpha(m^\alpha) = \begin{cases} \frac{1}{m^{\alpha}_{max} - m^{\alpha}_{min}} & \text{for } m^{\alpha}_{min} \le m^\alpha \le m^{\alpha}_{max} \\ 0 & \text{otherwise} \end{cases}$$

is the prior marginal for each model parameter (that is a uniform probability density function).

In our synthetic test we add Gaussian noise to the seismograms produced by the true model. Our prior information on the data can therefore be expressed through a Gaussian probability density function. Defining $\mathbf{r} = \mathbf{d} - \mathbf{d}^{obs}$ (where $\mathbf{d}$ are the actual data and $\mathbf{d}^{obs}$ are the observed data, i.e. actual data contaminated with noise), we write:

$$\rho_D(\mathbf{d}) = ((2\pi)^D \det\mathbf{C}_D)^{-1/2} \exp\left[-\frac{1}{2}\mathbf{r}^T\mathbf{C}_D^{-1}\mathbf{r}\right] \tag{1.4}$$

where $\det\mathbf{C}_D$ is the determinant of the data covariance matrix.

In our synthetic test we do not introduce any modeling uncertainties; the correlation between data and model parameters is therefore represented by a Dirac delta function:

$$\theta(\mathbf{d}|\mathbf{m}) = \delta(\mathbf{d} - \mathbf{g}(\mathbf{m})) \tag{1.5}$$

Substituting eqs (1.5), (1.4) into eq (1.2), and the result of the integration together with eq (1.3) into eq (1.1), we obtain:

$$\sigma_M(\mathbf{m}) = \begin{cases} k \exp\left[-\frac{1}{2}\mathbf{r}^T\mathbf{C}_D^{-1}\mathbf{r}\right] & m^{\alpha}_{min} \le m^\alpha \le m^{\alpha}_{max} \\ 0 & \text{otherwise} \end{cases} \tag{1.6}$$

where now $\mathbf{r} = \mathbf{g}(\mathbf{m}) - \mathbf{d}^{obs}$. Eq (1.6) represents, for our synthetic test, the solution of the inverse problem. Being a multidimensional probability density function it can be characterized in terms of its properties in the model space. We can identify the maximum likelihood model (in our case corresponding to the best fitting model). We can also compute the mean model:

$$\langle\mathbf{m}\rangle = \int_{\mathbb{M}} d\mathbf{m}\, \mathbf{m}\sigma_M(\mathbf{m}) \tag{1.7}$$

and the covariance matrix:

$$\mathbf{C}_M = \int_{\mathbb{M}} d\mathbf{m}\, (\mathbf{m} - \langle\mathbf{m}\rangle)(\mathbf{m} - \langle\mathbf{m}\rangle)^T\sigma_M(\mathbf{m}) \tag{1.8}$$

Equations 1.7 and 1.8 give useful results only if σ_M is Gaussian. In a Bayesian approach this is possible only if $\rho(\mathbf{m})$, $\rho(\mathbf{d})$ and $\theta(\mathbf{d}|\mathbf{m})$ are Gaussian and the equation $\mathbf{d} = \mathbf{g}(\mathbf{m})$ is linear. In case these conditions are not satisfied, we can still look at the information provided on a single parameter computing its corresponding marginal probability density function:

$$M(m^\alpha) = \int ... \int \sigma_M(\mathbf{m}) \prod_{\substack{k=1 \\ k\neq\alpha}}^{M} dm^k \tag{1.9}$$

Eq 1.9 involves computing the integral of the posterior probability density function in all the dimensions of the model space except the one corresponding to the parameter of interest.

If additional knowledge on model parameters is available, this methodology allows to introduce more complex a priori distributions and if the Gaussian assumption for data uncertainties is not valid also different norms can be used. We emphasize that eq (1.6) has been derived assuming no uncertainties in the forward modeling. This may be valid for a synthetic test. For a real case where uncertainties and approximations are present in the modeling, and if these effects can be quantified, the correlation between model parameters and data can be represented in terms of a more complex probabilistic correlation rather then a simple Dirac delta function.

1.2.2 Computing the posterior

In practise, solving an inverse problem from a Bayesian viewpoint implies computing integrals in a multidimensional space (eq 1.7, 1.8, 1.9). This can be done using Monte Carlo techniques which basically require generating samples according to the posterior probability density function. A variety of sampling methods can be used for this purpose (for a review, see for instance Tarantola [2005]). The applicability of each of these algorithms depends on the problem (if a small or large model space is considered, if an analytical, explicit expression of the posterior is available or not). Here, rather than directly using a sampling algorithm, we address the problem adopting a two stage procedure [Sambridge, 1999]: first, using an optimization algorithm, we explore the model space, possibly identifying its good data fitting regions. Secondly, using the whole ensemble of models found during the search stage, we compute a geometric approximation of the true posterior that is used for generating a new ensemble of models from which Bayesian inference can be performed. Sambridge [1999] validate this methodology using both a neighbourhood and a genetic algorithm to perform the search of the model space. Here we use an evolutionary algorithm [Beyer, 2001]. In principle any other direct search method can be used. Whitin this approach we can exploit the efficency of optimization algorithms in identifying good data-fitting regions of the model space and compute the forward modeling operator only during the search stage and not during the sampling process which usually requires larger number of evaluations (in this study 160100 models have been visited during the search stage, whereas the sampling process required generating 475000 models).

Searching the model space

The optimization algorithm we use to explore the model space is an evolutionary algorithm (EA) [Beyer, 2001]. EA is the current denomination used to identify all those population-based stochastic optimization methods inspired by the Darwinian paradigm of evolution. Among EAs there are genetic algorithms, evolutionary strategies and evolutionary programming techniques. According to these methods an optimization problem is considered similar to the process of evolution of a population of individuals that, through an evolutionary loop defined by a series of mechanisms like recombination, mutation and selection, improve their characteristics (fitness) in order to better survive in the environment where they are located. In our problem an individual is a model belonging to the model space and its "fitness" is given by the misfit value $(\mathbf{g}(\mathbf{m}) - \mathbf{d}^{obs})^T \mathbf{C}_D^{-1}(\mathbf{g}(\mathbf{m}) - \mathbf{d}^{obs})$ expressing the discrepancy between predictions and observations.

Among the many EAs available, we use, following the notation of Beyer [2001], a $(\mu/\mu_D, \lambda)$–Evolutionary Strategy[1]. According to this algorithm, the exploration of the model space starts with generating an initial population, corresponding to the generation $g = 0$, of μ $parent$ models $\mathcal{P}_\mu^{(0)}$:

$$\mathcal{P}_\mu^{(0)} := \{\mathbf{m}_1^{(0)}, \mathbf{m}_2^{(0)}, ..., \mathbf{m}_\mu^{(0)}\} \tag{1.10}$$

This set of models, obtained through uniform random sampling of the model space, then evolves through the subsequent repeated application of three operators: $Dominant$ μ-recombination, $Gaussian$ mutation and $Truncation$ selection.

The aim of the first two operators is to generate, from the current parent population, a new set of λ models, the $offsprings$ population. In the $Dominant$ μ-recombination, every ith component of the offspring $\tilde{\mathbf{m}}$ is obtained by uniform random selection from the μ i-components of the current parents. At each generation g we have:

$$\tilde{\mathbf{m}}_j^{(g)} := \sum_{i=1}^{M} (\mathbf{e}_i^T \mathbf{m}_{k_i}^{(g)})\mathbf{e}_i, \;\; j = 1, ..., \lambda \tag{1.11}$$

where k_i is an integer uniform random number between $\{1, ..., \mu\}$ and the symbol $\mathbf{e}_i$ stands for the unit vector in the ith direction of the model space. The scalar product gives the ith component of the uniformly random selected parent $\mathbf{m}_{k_i}$.

In the $Gaussian$ mutation an additional perturbation is added using a normal distribution $\mathcal{N}$ with zero expectation value:

$$\hat{\mathbf{m}}_j^{(g)} := \tilde{\mathbf{m}}_j^{(g)} + (\sigma_1 \mathcal{N}(0,1), ..., \sigma_M \mathcal{N}(0,1)) \tag{1.12}$$

where $j = 1, ..., \lambda$ and $\mathcal{N}(0,1)$ represents a normal random number with zero expectation value and unit standard deviation. The final offspring $\hat{\mathbf{m}}$ is therefore

[1]In this notation μ denotes the number of parents and λ the number of offsprings. The comma symbol "," indicates that the μ parents for the next generation are selected among the only λ offsprings of the current generation. Note that this implies $\lambda \geq \mu$. The notation μ/μ_D denotes that all the μ parents are used for $Dominant$ (D) recombination.

obtained around the parental recombination result $\tilde{\mathbf{m}}$ through the addition of a Gaussian random vector. The mutation can be isotropic, that is for all the parameters the standard deviation is the same, or anisotropic (in case model parameters have different physical meanings therefore requiring different standard deviations). The aim of the selection operator is to choose among the final set of offsprings a new ensemble of models to be used as a parent population for the next generation. In the $Truncation$ selection this is done in a deterministic way. The new parent population is formed by selecting the μ best fitting models among the only λ offsprings. This requires $\lambda \geq \mu$. This series of steps is repeated until a stop criterion is reached (e.g. a stationary level of fit). Evidently, the last step of the algorithm is the most expensive in terms of computation time because it requires the calculation of the misfit function for each offspring. Great improvement can be achieved parallelizing the computation, i.e. distributing the calculation of the misfit over several processors and, once collected the results, performing the selection.

The EA requires a certain number of parameters to be tuned. The number of parents and offsprings, μ and λ respectively, and the standard deviations for the mutation operator. Unfortunately no general theory is available that helps to choose optimal values for these parameters, essentialy because the performance of the algorithm is strictly dependent on the unknown "fitness landscape". However, some guidelines are available. The ratio μ/λ determines the tradeoff between exploration/exploitation. Clearly the condition $\mu = \lambda$ basically means pure exploration (no selection among offsprings) and as the ratio μ/λ decreases the exploitation tendency increases. For the mutation operator, the algorithm allows to choose a different standard deviation for each model parameter. To limit the number of tuning parameters, we choose to use different standard deviations only for those parameters that represents different physical quantities. The "strength" of the mutations (the magnitude of the standard deviations) is another important factor. They should not be too small, to ensure population diversity, and not too large, to allow convergence towards good data fitting regions of the model space. However, following these guidelines is not sufficient to properly set the algorithm's parameters, and additional trial and error work is usually required.

Appraising the ensemble

The models produced by the evolutionary algorithm cannot be used directly for Bayesian inference, because they are not generated according to the posterior probability density function. However all these models, together with their corresponding values of $\sigma_M(\mathbf{m})$ (easily computed knowing the value of the misfit, eq 1.6) constitute an important source of information about the structure of the actual posterior; this can be used to compute a geometric approximation of it, from which samples can be drawn. This is the basic idea behind the appraising methodology developed by Sambridge [1999].

The ensemble of models found during the search stage constitute an irregular distribution of points in the model space. Around each of these points a nearest-neighbor region can be calculated using a geometrical construct known as Voronoi cell. For any distribution of irregular points in any number of dimensions, Voronoi cells are unique, space-filling, convex polyedra, whose size and shape are automatically adapted to the distribution of the point set. This implies that the size (volume) of each cell is inversely proportional to the density of the points. A geometric approximation of the true posterior is then calculated setting the known value of the posterior of each model to be constant inside its Voronoi cell.

A new ensemble of models generated according to the approximated posterior is produced using a Gibbs sampler. A Gibbs sampler generate samples performing a random walk in the model space. From a given starting point, the algorithm sequentially performs a step along each parameter axis generating a random deviate from the conditional probability density function of the approximated posterior along the considered direction. An iteration is completed when all dimensions have been cycled through once, and a new model has been generated. After many iterations, the random walk will generate models with a distribution that tends towards the target distribution, that is the approximated posterior.

The practical applicability of this methodology is limited by the memory and computation time needed to perform this appraising step. The storage S required by the algorithm is controlled by the number of models constituting the ensemble N_e and the number of dimensions of the model space M:

$$S \propto N_e M \tag{1.13}$$

Computation time T is additionally dependent on the resampled ensemble N_r, that is by the set of models sampled from the approximated posterior:

$$T \propto N_r N_e M \tag{1.14}$$

As in the in the search stage, computational time can be greatly decreased distributing the resampling process on several processors.
For the synthetic test we present, the dimension of the model space is $M = 38$, the number of models visited during the search is $N_e = 160100$. The number of models constituting the resampled ensemble is $N_r = 475000$. The resulting computation time (on a 20 CPUs Linux cluster) is $T \sim 1$ day.

1.3 A synthetic test

To control uncertainties in data and in forward modeling we consider a synthetic test. The kinematic rupture model we use as “true” model is shown in fig 1.1. We represent the fault as a 32 km long and 12 km deep, vertically dipping, plane surface. The fault’s upper edge is at 2.75 km depth. The rupture process is characterized by a heterogeneous distribution of peak slip-velocity, whereas rake angle and rise time are constant ($0°$ degrees, 0.8 s respectively). Peak slip-velocity values are defined on a 4 by 4 km grid (nodes represented by black dots). The time evolution of the rupture process is prescribed in terms of a circular front that propagates from the hypocenter (12.5 km deep) with constant rupture velocity ($V_r = 2.7$ km/s).

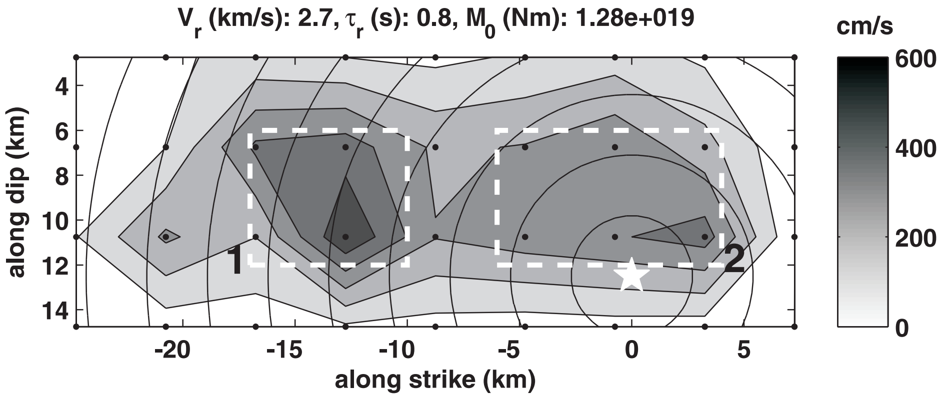

Figure 1.1: The "true" kinematic rupture model . Only the maximum slip-rate is heterogeneous. Rake angle is everywhere zero (pure left-lateral strike slip event) and rise time is constant, $\tau_r = 0.8$ s. Rupture times are given by the arrival times of a circular rupture front expanding from the hypocenter (white star) with constant rupture velocity $V_r = 2.7$ km/s. The corresponding seismic moment is $M_0 = 1.28e19$ Nm. Black dots represent locations where peak slip-velocity values are defined. Dashed white rectangles delimit the two main large-slip regions characterizing the slip distribution. In the article we will refer to them as asperity 1 (the one on the left) and asperity 2 (the one on the right).

The observational network we use for the inversion is depicted in fig 1.2. The fault strikes at $150°$, station locations and velocity model are adapted from the 2000 Western Tottori earthquake [Semmane et al., 2005]. All stations are located within 60 km from the epicenter.

We compute ground velocities using the frequency-domain representation theorem [Spudich & Archuleta, 1987]:

$$\dot{u}_m(\mathbf{y}, \omega) = \iint_\Sigma \dot{\mathbf{s}}(\mathbf{x}, \omega) \cdot \mathbf{T^m}(\mathbf{x}, \omega; \mathbf{y}, \mathbf{0})\, \mathbf{d\Sigma} \tag{1.15}$$

where $\dot{u}_m$ is the m component of ground velocity at the receiver location $\mathbf{y}$, $\dot{\mathbf{s}}$ is the slip-velocity function, $\mathbf{T^m}$ is the traction exerted across the fault surface Σ at point $\mathbf{x}$ generated by an impulsive force applied in the mth direction at the receiver and $\omega = 2\pi f$ is the angular frequency.

Tractions $\mathbf{T^m}$ are computed, up to a frequency of 2 Hz, using a Discrete Wavenumber / Finite Element method (Compsyn package, [Spudich & Xu, 2002]), for a 1D flat layered Earth model without attenuation. A trapezoidal-rule quadrature of the product $\dot{\mathbf{s}} \cdot \mathbf{T^m}$ is performed separately for each frequency, with the quadrature points being the sample points where $\mathbf{T^m}$ have been computed. Peak slip-velocity values at integration points are derived through bilinear interpolation of values of surrounding grid nodes. The slip-velocity function is assumed to be an isosceles triangle. With this parametrization, the maximum slip-rate corresponds to the hight of the isosceles triangle and the rise time to the base length. Each computed synthetic seismogram contains 4096 data points, from 0 to 40.95 s, with a time sampling of

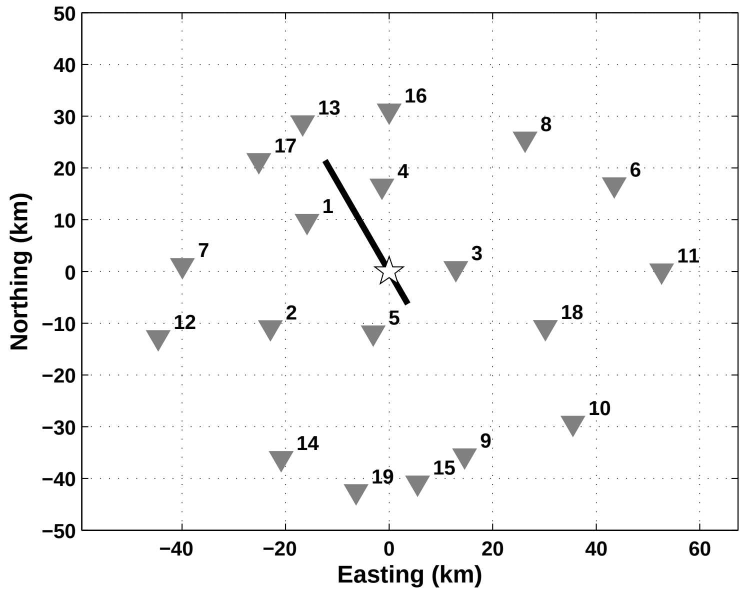

Figure 1.2: The observational network. 19 stations (gray triangles) are located near the fault strike (black solid line) within 60 km from the epicenter (white star).

0.01 s.

We do not introduce any uncertainties in the forward modeling but we perturb synthetic seismograms produced by the true model with Gaussian noise so that a data covariance matrix C_D can be computed. We assume noise statistics to be the same for each waveform and without correlation between different stations and between different components of the same station. Thus, the covariance matrix for the whole set of data reduces to a block diagonal matrix where each block matrix represent the covariance matrix for each single waveform. To compute the covariance matrix we follow the approach of Gouveia & Scales [1998]. We treat each synthetic seismogram produced by our true model as a "mean" seismogram s^{mean}. We then compute several realizations of noisy seismograms s^{noise} simply adding to the mean seismogram a Gaussian time series s^{gauss} with zero mean and fixed standard deviation ($\mathrm{s}^{noise} = \mathrm{s}^{mean} + \mathrm{s}^{gauss}$). If N is the number of realizations, an estimate of the covariance matrix for each waveform is given by:

$$\hat{C}_D = \frac{1}{N}\sum_{i=1}^{N}(\mathbf{s}_i^{noise} - \mathbf{s}^{mean})(\mathbf{s}_i^{noise} - \mathbf{s}^{mean})^T = \mathbf{s}_i^{gauss}(\mathbf{s}_i^{gauss})^T \tag{1.16}$$

from which we see that $\hat{C}_D$ is the same for all inverted seismograms depending on the Gaussian time series only. For our synthetic test we generate Gaussian time series with zero mean and standard deviation equal to 1 cm/s which are then filtered in the frequency range 0.1-0.5 Hz. The resulting standard deviation of the noise is very

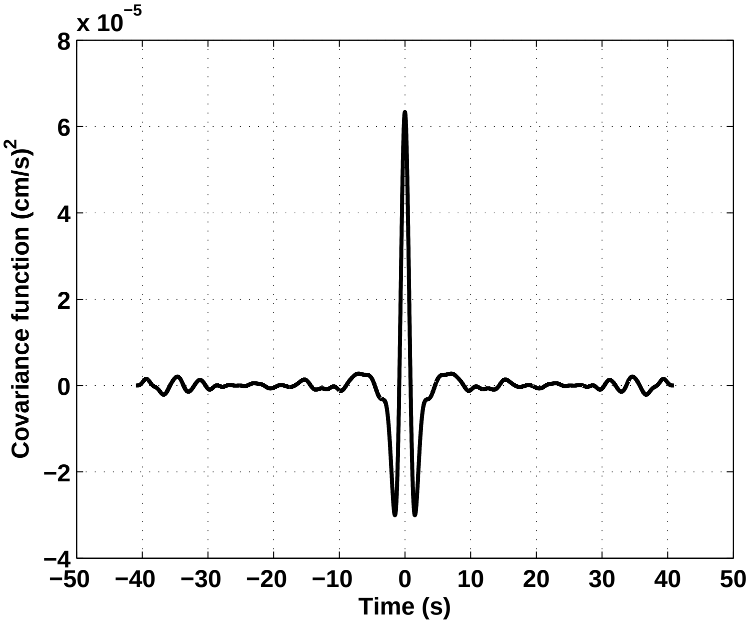

Figure 1.3: The noise covariance function. The correlation is almost zero after 10 s. This is consistent with the fact that the covariance matrix has been estimated considering Gaussian time series filtered in the frequency range [0.1 0.5] Hz, containing therefore periods between 2 and 10 s.

small, about 0.01 cm/s. The corresponding signal-to-noise ratio (SNR) (calculated as the ratio between the maximum value of the signal and the maximum value of noise) varies depending on the waveforms. The minimum SNR observed is about 7. We performed $N = 500$ noise realizations and the resulting $\hat{C_D}$ was smoothed by replacing each element with the average of its diagonal. In fig 1.3 we show the resulting noise covariance function (i.e. the cross diagonal terms). Note how the filtering has introduced a certain level of correlation in the noise that almost disappears after 10 s, consistent with the fact that noise below 0.1 Hz has been filtered out.

We invert all components for all stations in order to retrieve peak slip-velocity values at grid points, rupture velocity and rise time. Rake angle and hypocenter location are fixed to their true values. We define peak slip-velocity values on the same grid used for calculating the true seismograms. As we mentioned in section 1.2.1, for each model parameter the prior marginal is uniform, inside a predefined range of values. Model parameter ranges are [0 600] cm/s for peak slip-velocity, [2 3] km/s for rupture velocity and [0.5 1.5] s for rise time. The total number of model parameter we invert for is therefore 38.

The fitness function used during the search is calculated as the reduced χ^2_ν value of the data fit, where ν is the number of degrees of freedom (number of data minus number of parameters):

$$\chi^2_\nu = \frac{1}{\nu}(\mathbf{g}(\mathbf{m}) - \mathbf{d}^{obs})^T \mathbf{C}_D^{-1}(\mathbf{g}(\mathbf{m}) - \mathbf{d}^{obs}) \tag{1.17}$$

Equation 1.17 contains the inverse of the covariance matrix $\mathbf{C}_D^{-1}$. In our case each waveform contains 4096 data points so that the covariance matrix for each waveforms is a 4096×4096 matrix. As a first order approximation we consider, in the calculation of the misfit, only the main diagonal (i.e. the variance of the noise).
From equation 1.17 we also see that the misfit value depends, through $\mathbf{d}^{obs}$, on the particular noise realization added to the "mean" seismograms. In this study we present results obtained using a single data realization. Clearly a different data realization would produce, for the same model, a different value of fit. However it is beyond the scope of this paper to investigate the effect of different noise realizations in the computed posterior.

1.4 Inversion results

1.4.1 The maximum likelihood model

As explained in section 1.2.2 the first step in our inversion consists of searching the parameter space. After several trial inversions the evolutionary algorithm parameters have been fixed to the following values: $\mu = 100$, $\lambda = 4000$. The standard deviations for the mutation operator, for peak slip-velocity, rupture velocity and rise time are, respectively: $\sigma_{A_{max}} = 10$ cm/s, $\sigma_{V_r} = 0.3$ km/s and $\sigma_{\tau_r} = 0.3$ s. We do not expect these values to be optimal (in rendering the search the most efficient) and as already stated in section 1.2.2, even if some guidelines are available trial and error work is usually required to set these parameters.

In fig 1.4 we show the best fitness function value for each generation versus the generation number. After about the 20th generation the misfit reaches an approximately stationary level that lasts until the search is stopped. The total number of models visited is 160100. On a 20-CPU Linux cluster the search required about 1 day of computation time.

The first result of the search we may look at is the maximum likelihood model (corresponding to the best fitting model in our problem, the one with the lowest χ^2_ν value). We show it in fig 1.5. Comparing with the true model (fig 1.1) we can see that the general characteristics of the rupture process are retrieved. The locations of the two slip patches are correctly imaged and also rupture velocity and rise time values are close to the true ones. These similarities produce also a corresponding seismic moment near the true value. However, we can also see that even if the large scale features are correctly imaged, the details are not, e.g. at the bottom of the fault the peak slip-velocity is significantly over estimated. Despite these differences the corresponding level of fit is visually very good (Fig 1.6 and 1.7). Numerically it corresponds to $\chi^2_\nu \simeq 118$. This high value (for uncorrelated noise $\chi^2_\nu > 1$ means that predicted data are not able to reproduce, in average, the observed data whitin the assumed standard deviation) is basically due to the very small uncertainties we consider in measuring the data-fit (we recall that the standard deviation of noise is ~ 0.01 cm/s).

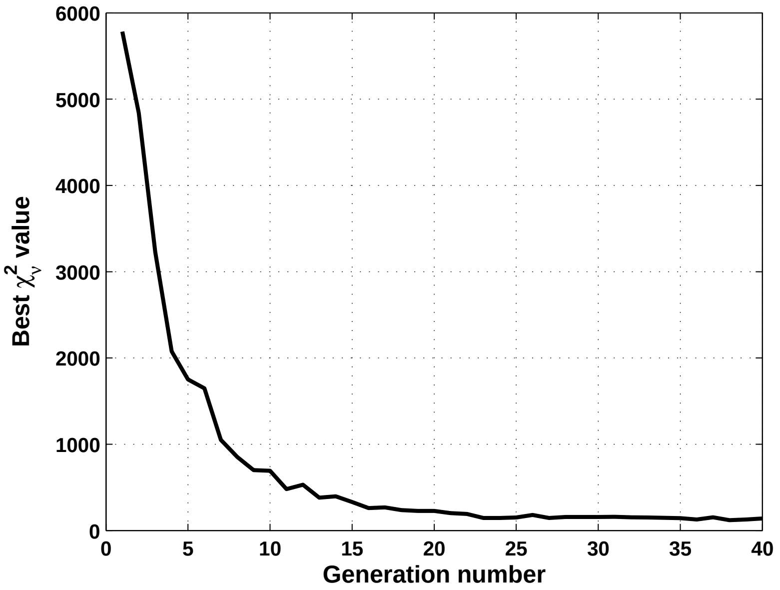

Figure 1.4: χ^2_ν reduction during the search. The best fitness function value for each generation versus generation number is shown. After about the 20th generation the misfit reaches an approximately stationary level.

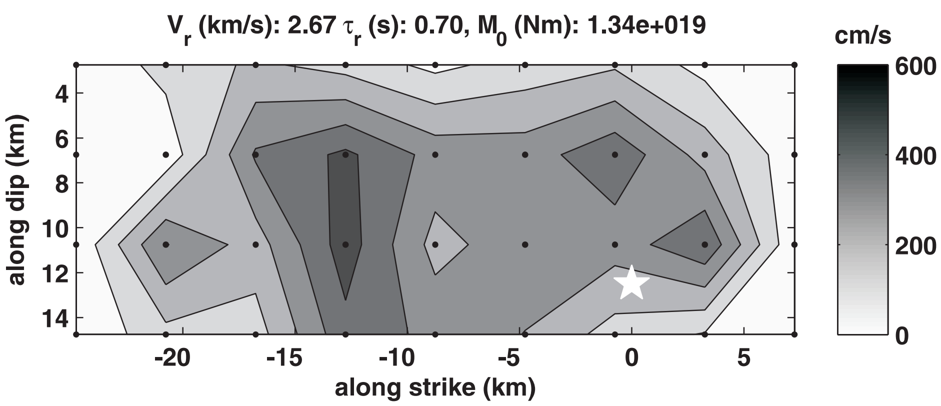

Figure 1.5: The maximum likelihood model (corresponding to the lowest χ^2_ν value). The general shape of the slip distribution is correctly retrieved and rupture velocity, rise time and seismic moment values are close to the true ones. However the maximum slip-rate is over estimated at the bottom of the fault.

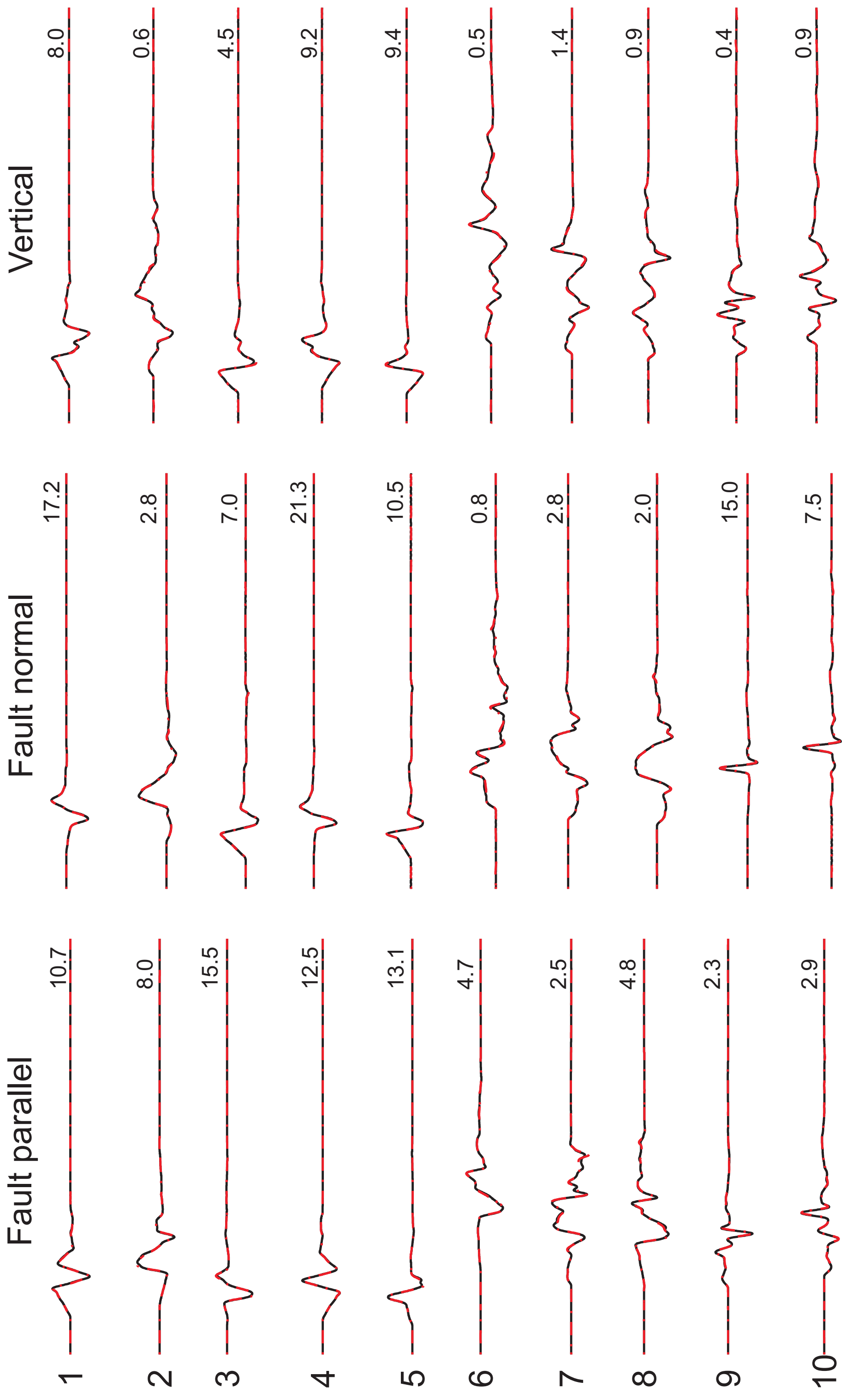

Figure 1.6: Data fit between data-prediction (solid black) and observed data (dash-dot red) for the maximum likelihood model. For each waveform the maximum amplitude (cm/s) of the observed ground velocity is shown.

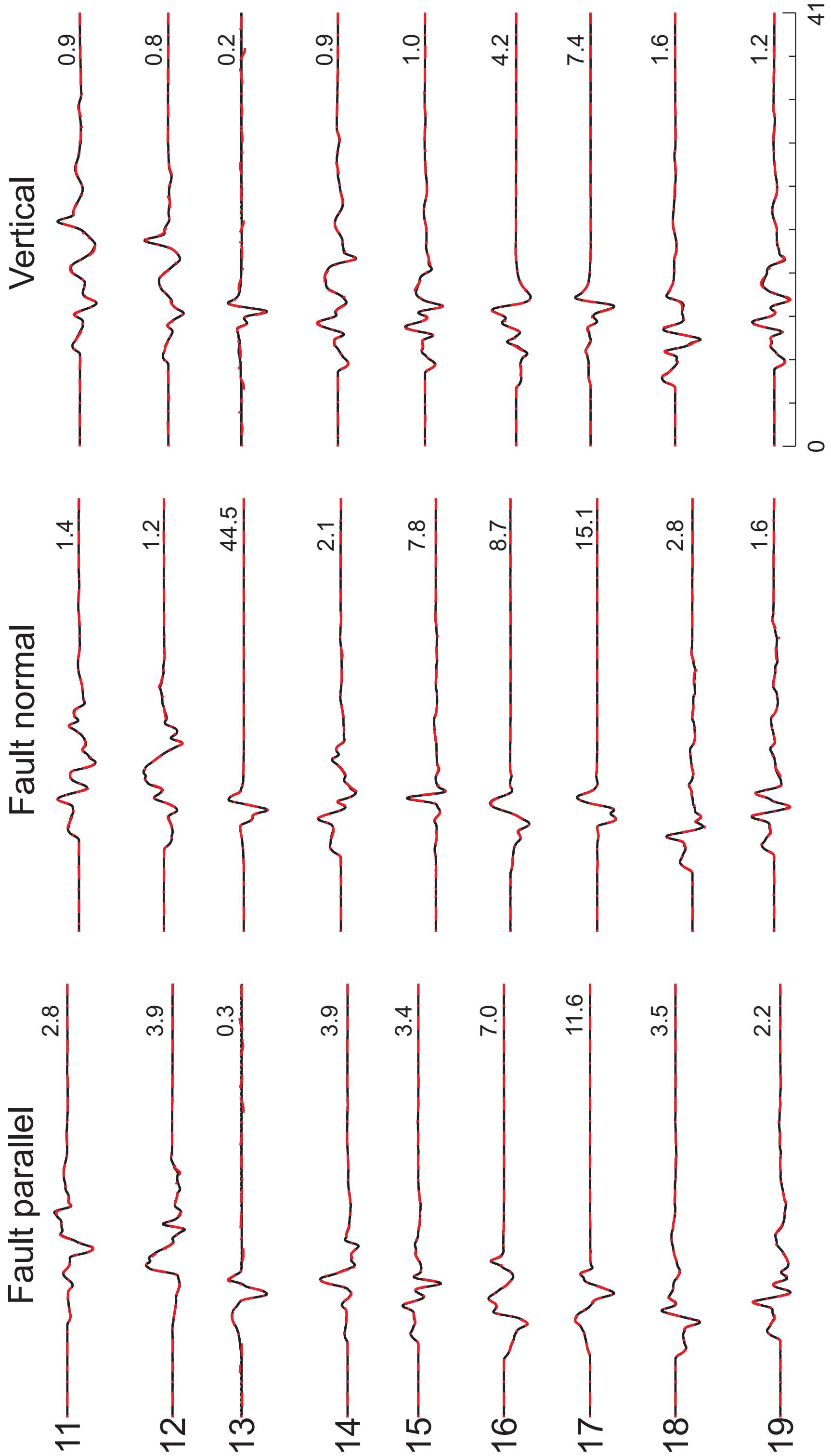

Figure 1.7: Continuation of Fig 1.7

1.4.2 Uncertainties estimates

The need for estimating uncertainties comes from the fact that the maximum-likelihood model is not the only model that produces a good level of fit to the data. In fig 1.8 we show peak-slip velocity distributions for 40 models, found during the search, with a $\chi^2_\nu \leq 1000$. The visual analysis of the peak slip-velocity distributions shows that all these models share some large scale features also present in the best-fitting solution: low slip-rate at the top, right and left borders of the fault and near the hypocenter; a major slip patch located between -20 and -10 km along strike; and a second slip patch above the hypocenter. Despite this common characteristics, the details of each peak slip-velocity distribution varies from model to model. In fig 1.9 and 1.10 we show the level of fit produced by all these models. They all generate waveforms very similar to the observed ones. From this example it can be seen that, within a certain level of fit, the inverted data cannot constrain a single model but rather a set of models which are different one from another but share some common properties. Quantifying and expressing these common properties is the ultimate goal of the inversion.

Following the methodology described in section 1.2.2 we compute for each model parameter its corresponding 1D posterior marginal probability density function. In fig 1.11 we show the posterior and the prior marginals for the peak slip-velocity, together with the true value, for each grid node on the fault surface. We also plot the raw marginals computed from the ensemble of models generated by the evolutionary algorithm. Each subplot corresponds to a node position. We indicate node's coordinates (along strike, along dip) in km, with respect to a reference system centered at the epicenter and pointing toward southeast. The hypocenter is at (0,12.5). For each posterior marginal we compute mean value (μ) and standard deviation (σ). All marginals are normalized to unit area so that relative information can be compared.

Comparing raw and posterior marginals we see that they are in general different, that is, they do not follow the same distribution. The raw marginals often present a much better defined peak then the posterior suggesting therefore better resolution then the actual one (see for instance posteriors at (-20.75,2.5), (-16.75,2.5)). This shows that the statistical properties of the ensemble of models produced by the evolutionary algorithm do not represents the actual uncertainties affecting model parameters.

We also notice that in general posteriors do not show a Gaussian shape (especially for those parameters for which the true value is close to 0 or to the maximum boundary value, like the posteriors at (-24.75,2.5) and (-12.75,10.5)). For these cases, the standard characterization in terms of mean value and standard deviation is not really meaningful: the mean value would not correspond to the maximum likelihood value and the standard deviation cannot be interpreted as a symmetric error bar on the mean value. For these parameters we therefore cannot use the Gaussian uncertainty hypothesis.

Without the support of the Gaussian assumption resolution on model parameters can be better understood by looking at the difference between priors and posteriors.

Figure 1.8: Peak slip-velocity distributions (cm/s) for a set of models, found during the search, with $\chi^2_\nu \leq 1e3$. Simple visual analysis shows that all models share some large scale features. Low slip-rates at top, left and right borders of the fault and near the hypocenter. Two main slip patches, the one on the left characterized by higher values (between 400-600 cm/s).

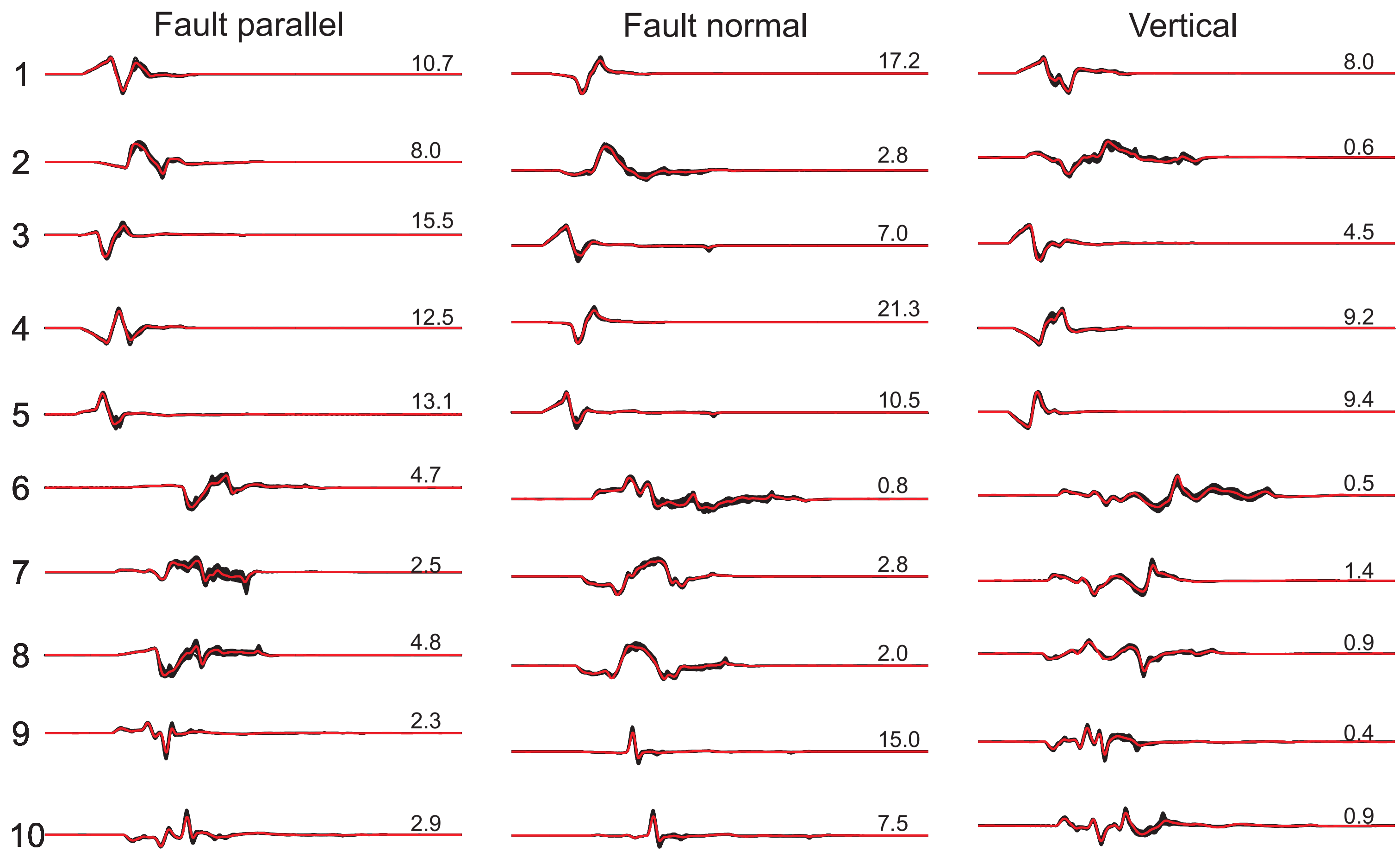

Figure 1.9: The level of fit produced by the rupture models shown in figure 1.8 (black data-predictions, red observed). For each waveform the maximum observed ground velocity (cm/s) is shown.

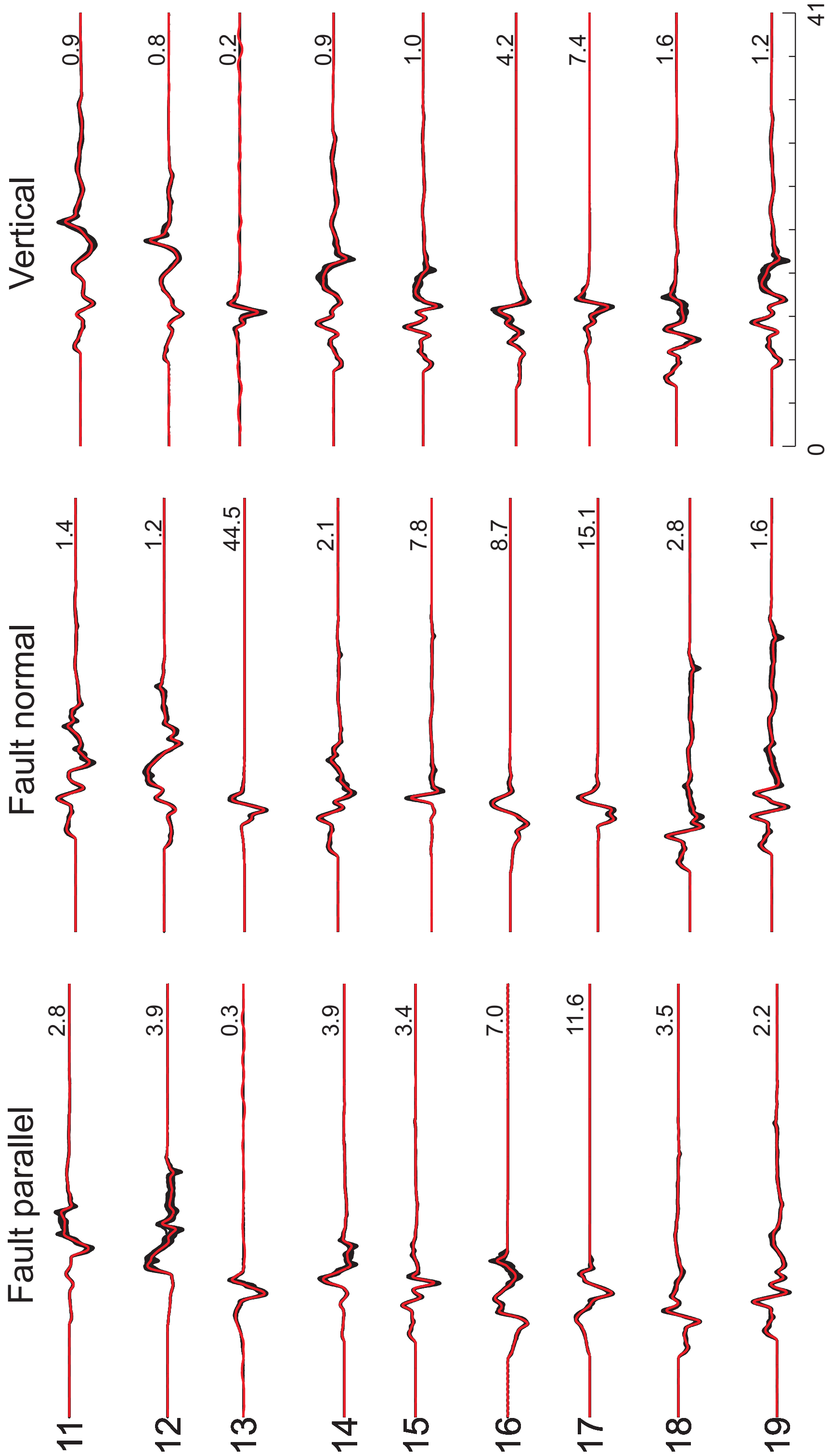

Figure 1.10: Continuation of Fig 1.9

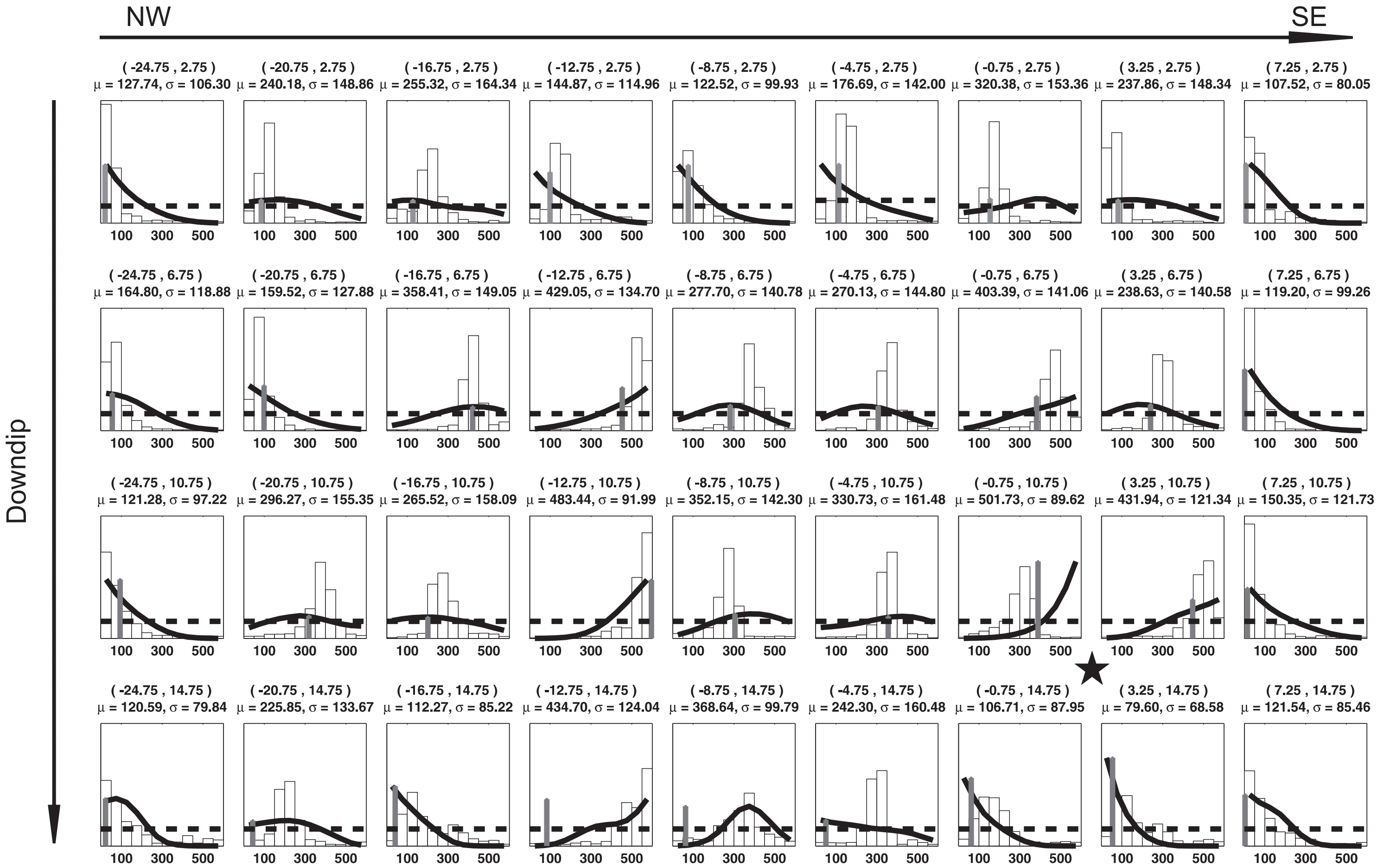

Figure 1.11: 1D posterior (black solid line) and prior (black dashed line) marginal probability density functions for peak slip-velocity at grid nodes on the fault surface. Each subplot corresponds to a node position. True values are represented by vertical gray bars. White histograms represent 'raw' marginals produced by the evolutionary algorithm. The black star represents the hypocenter location.

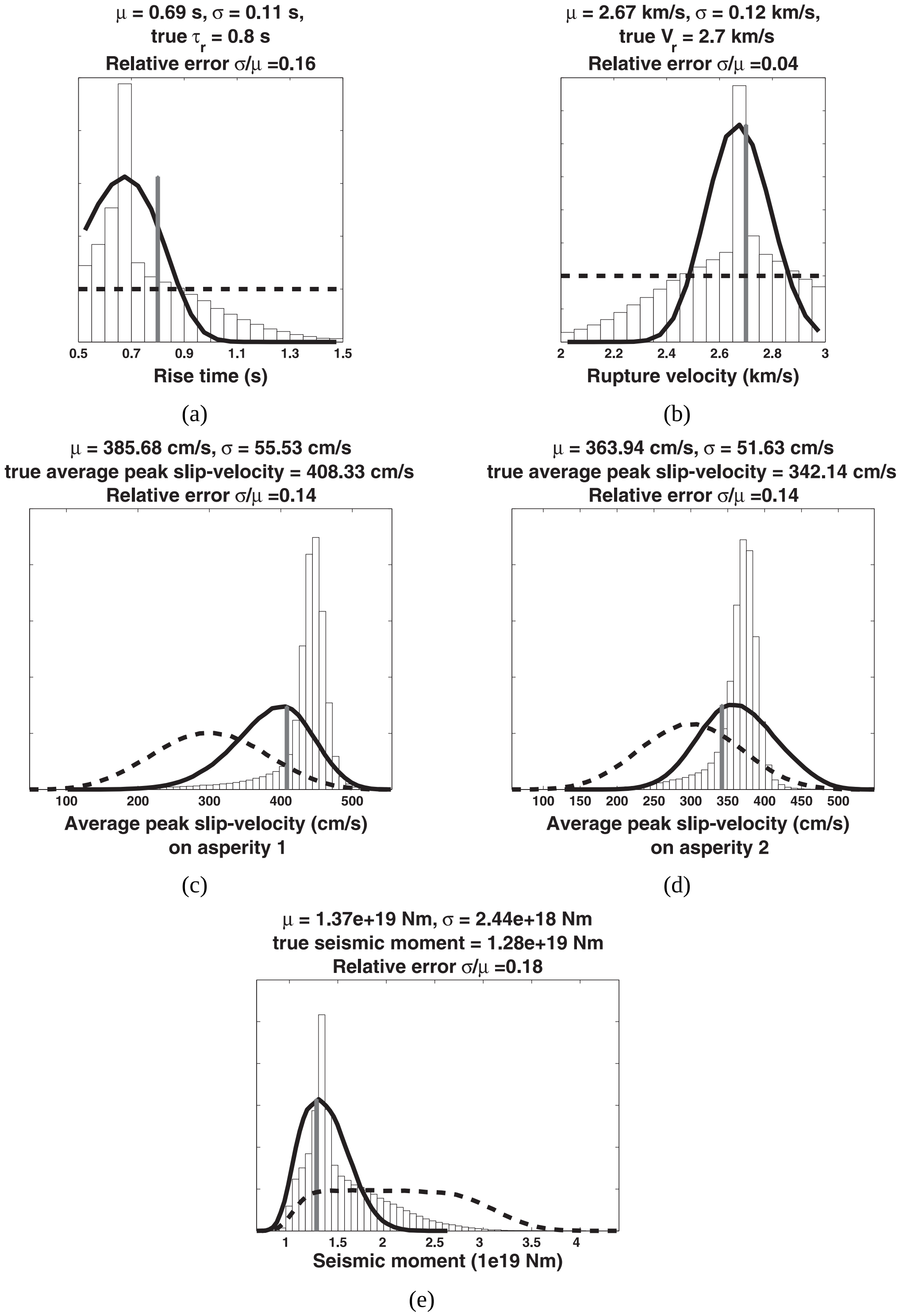

Figure 1.12: 1D posterior (black solid line) and prior (black dashed line) marginal probability density functions for rise time (a), rupture velocity (b), average peak slip-velocity on asperity 1 (c), and 2 (d), and seismic moment (e)

At some fault locations a single well defined peak in the posterior can be identified (at the right and left sides of the fault surface, for instance), at some others locations there is little difference with respect to the uniform prior (see posteriors at (-20.75,2.5), (-16.75,2.5), (-20.75,10.5), (16.75, 10.5) for instance), suggesting therefore poor resolution.

We can also see that at the lower edge of the fault (nodes at (-12.75,14.75), (-8.75,14.75)) and at node (-0.75,10.75) the true value is located on the tail of the computed marginal posterior. For these parameters the posterior seems to miss the true value. A tentative explanation for these results can be that for these parameters the search algorithm did not reach the true values but got locked into a solution prematurely. Assuming these parameters to be very poorly resolved (something that we can expect for nodes located in the bottom part of the fault) the "fitness" landscape for those parameters will be something similar to a valley. If then the search is stopped before exploring the entire valley and therefore without reaching the true values, the reconstructed posterior will be incomplete and will contain that valley only partially. Therefore, even if the true posterior is constant for these parameters, the approximated posterior will be peaked only around the best-fitting models found during the search. This is important to bear in mind. The reconstructed posterior reflects only what the search algorithm illuminated. This implies that the reconstructed posterior may not completely reflect the true, data-determined posterior. A similar behaviour can also be find in the results provided by Sambridge [1999]. In the synthetic reciver function problem he considers, the marginal posterior for the thickness of the bottom layer completely misses the true value (figure 7, pag. 738).

We present also the 1D marginals for rise time and rupture velocity (1.12 (a) and (b)). Again, a well defined single peak of the raw marginals contrasts with a smoother and broader a posteriori distribution. For these two parameters the posteriors shows approximately a Gaussian shape so that they can be characterized in terms of mean value and standard deviation. The mean rise time underestimates the true value of about 0.1 s. The true rupture velocity is inside one standard deviation (about 0.1 km/s) from the estimated mean rupture value.

Besides single model parameters, we can also analyze resolution on combination of model parameters. As we have noticed before often much more resolution is achieved on the large scale features of the slip distribution rather then on the local details. In fig 1.12 (c) and (d) we present 1D marginals for the average peak slip-velocity on the two main asperity regions characterizing the true model (asperities extensions are: 7 by 6 km for asperity 1 and 10 by 6 km for asperity 2). Here we see that our a priori marginal is not uniform anymore because it represents information on a combination of the original parameters. In both cases the true values are correctly retrieved with a good resolution (standard deviations of the order of 50 cm/s, corresponding to relative error of 14%). Good resolution is achieved also for the seismic moment (standard deviation equal to 2.44e18 Nm, relative error 18%) (fig 1.12 (e)).

1.5 Reconstructing the posterior

Our resolution analysis derives from the reconstructed posterior computed from the ensemble of models visited during the search stage. This implies that our uncertainty estimates depend on the way the search developed in the model space. To further elucidate this point we perform three independent searches, with the same settings for the evolutionary algorithm parameters, but with different seeds for the random number generator. We carry out the searches for the same number of generation. In fig 1.13 and 1.14 we show posterior marginals for all the original parameters investigated in this study considering the three independent ensembles produced. We can see some variability affecting especially the marginal probability densities for local peak slip-velocity parameters, but the general features of the inverse solution are maintained. The variability we observe comes from the fact that these three ensembles search the model space in different ways so that each of them provides different approximation of the actual posterior. This is an inherent difficulty because an exhaustive search is unfeasible and we are forced to explore the parameter space only in a limited number of points. This is especially true for large dimensional model spaces. Merging the set of models produced by independent searches into one single ensemble can be a good strategy to increase the results' stability. However one has to bear in mind that, for this kind of analysis, memory requirement and computation time scale with the size of the ensemble (see eq 1.13 and 1.14).

1.6 Discussion

Accurate estimates of uncertainties are needed in order to asses the reliability of the inverted solutions. As it has been pointed out by different authors (Cohee & Beroza [1994]; Beresnev [2003]; Ide et al. [2005]) and is also represented in the online database of earthquake rupture models (http://www.seismo.ethz.ch/srcmod), for the same earthquake, acceptable fit to the data can be provided by different rupture models. The discrepancies between models may be due to the different choices adopted during the inversion concerning the forward modeling, the model parametrization, the inversion methodology, the type of data set and processing used. However, independently of the particular approach, intrinsic reasons render imaging the earthquake source a problem with multiple solutions: uncertainties in data and in forward modeling (which allow multiple models to be considered acceptable) and lack of resolution (due to the always limited data coverage). For a linear or linearized inversion, these factors render the problem ill-conditioned and ill-posed. For instance, Graves & Wald [2001], considering a linear slip inversion, explicitly showed that uncertainties in Green's funtions increase ill-conditioness of the problem, requiring increasing value of damping parameter (smoothing of slip in their case) to stabilize the matrix inversion.

In the context of earthquake source inversions real waveforms are contaminated with ambient noise and also by uncertainties in the alignment of the recording sen-

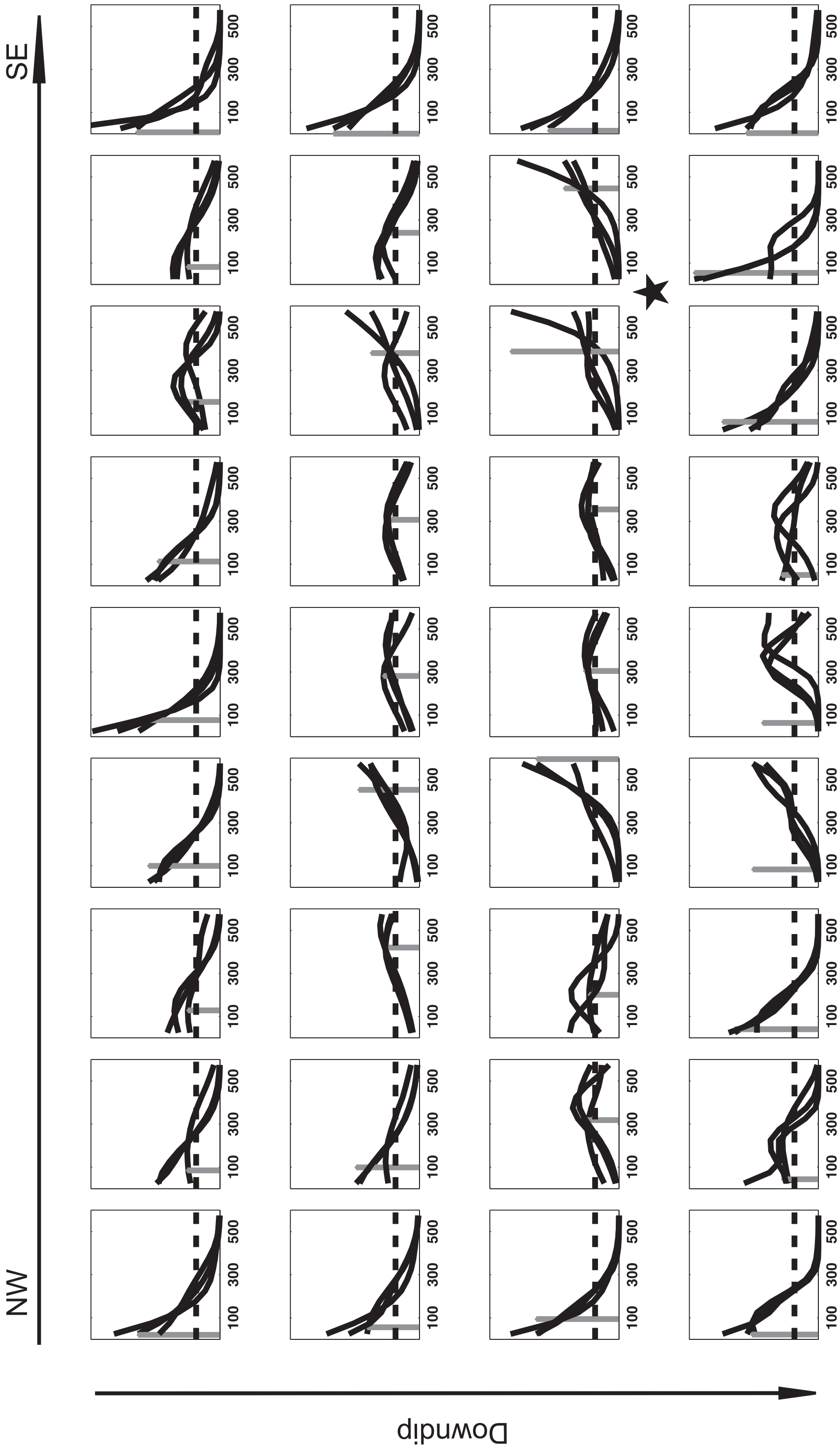

Figure 1.13: 1D posterior marginals (black solid lines) for peak slip-velocity at grid's nodes computed considering threee independent ensembles.

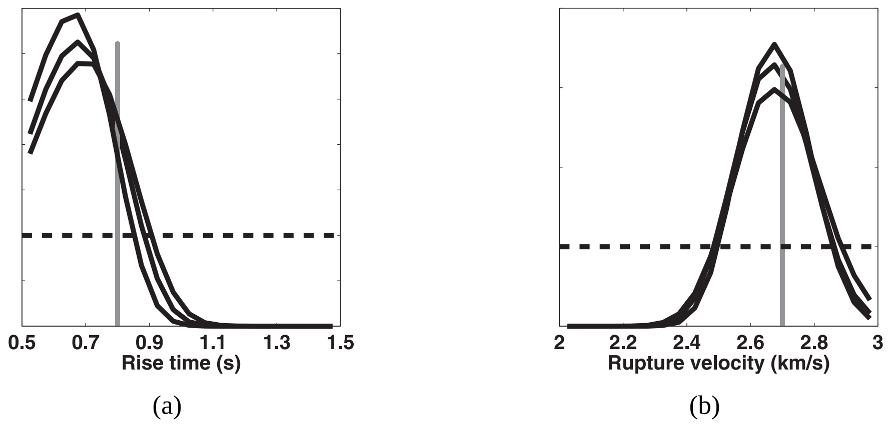

Figure 1.14: 1D posterior marginals (black solid lines) for rise time (a) and rupture velocity (b), computed considering three independent ensembles.

sors. More important, in our opinion, are the uncertainties due to approximations in the forward modeling. Real waveforms often show complexities (due to source, path and site effects) which the adopted modeling is not able to explain. The best-fitting model (the model which provides the best numerical fit to the data) is therefore not so meaningful because we do not know precisely to what extent the best-fitting model is reproducing the modeled part of the data rather than the unmodeled one. Providing the best-fitting model as an image of the earthquake source can be therefore misleading. We suggest therefore that a better way to show results of an earthquake source estimation is to provide multiple models which are able to reproduce the data within a certain level of fit (determined by the accuracy of our data and modeling). In such a way we can visually identify what are the main features of the inverted solutions whitout trying to draw conclusions from the unstable details.

Lack of resolution is another important factor to bear in mind. The fact that linear inversions practically always require damping parameters implies the presence of a null space in the model space (or in other words of very close-to-zero singular values). In physical terms what happens is that the data we consider may contain very little information about certain parameters we want to invert for. In our methodology, which does not require any matrix inversion, we try to measure this lack of resolution rather than reducing it through the addition of damping parameters.

Considering a simple synthetic test, we point out that imaging the earthquake source implies a process of extraction of information from a set of data (in our case waveforms) which cannot be reduced to simply providing a best fitting model. Efforts should be put in estimating resolution on inverted parameters. Multiple rupture models may in fact produce very similar waveforms. We want to stress that uncertainty analysis should be carried out using an appropriate theoretical framework in order to get meaningful results. We have shown how the use of an optimization algorithm to estimate uncertainties is not suitable. We suggest that a Bayesian approach instead provides a possible way to face this problem.

The main consequence in using this approach is that our knowledge of the earthquake rupture process, as derived by the fitting of some kind of data, can be only probabilistic. In other words, available data and theoretical knowledge do not allow us to identify a single model but rather a set of models which share certain statistical properties. Identifying and quantifying these statistical properties should be the real aim of any inversion.

We used this approach considering only strong motion data. Clearly, this methodology can be applied also to investigate resolution on model parameters considering different data sets (teleseismic data, geodetic data) which all togheter can improve the quality of our inferences. Wald & Graves [2001] showed, for a linear slip inversion, that adding geodetic data to seismic data has a significant contribution. They found that features imaged by inversion of individual data sets alone may not be recognized when using combined data.

1.7 Conclusions

In this paper we address the problem of inferring kinematic earthquake rupture parameters following a Bayesian approach. Imaging the earthquake source is seen as a problem of combination of information: a priori information (available before the inversion) and information contained in the data. This combination gives the posterior state of information, represented by a probability density function over the model space. We compute the posterior using a two step procedure. First we explore the model space through an evolutionary algorithm. The search of the parameter space reveals that within the same level of fit the observed waveforms can be reproduced by multiple models. All of them, though being different one from another, share some similarities. Quantifying and expressing these similarities is the aim of the second step. We use the ensemble of models found during the search to compute a geometric approximation of the true posterior and we use it to compute marginal probability density functions for each model parameter. Each marginal represents the combination of the prior information with the information that we have been able to extract from the data. From each marginal we can derive uncertainty estimates.

We point out how this second step of the procedure is particularly important in order to correctly compute resolution on inverted parameters. The search algorithm alone, though being effective in finding good data fitting models, does not provide direct information about uncertainties. Misleading results can be obtained if simple statistical analysis of the ensemble of models is used to estimate resolution. We also point out how the information content on the inverted parameters cannot be always represented in terms of Gaussian probability density functions. We show explicitly how for some parameters the posterior marginal does not follow a Gaussian shape: for these parameters the standard characterization in terms of mean value and standard deviation is not meaningful. The fact that Gaussian uncertainty hypothesis is not valid for non-linear problems is widely known but still current non-linear source estimations adopt this approximation. We also point out how estimating resolution can be limited by our ability in reconstructing the true structure of the posterior. This is an intrinsic difficulty due to the fact that exhaustive search is unfeasible and that we are always forced to explore the model space on a limited number of points. The consequence is that uncertainties estimates will be always subject to a certain amount of variability which decreases as the exploration of the model space becomes more and more extensive.

Acknowledgments

We thank Malcolm Sambridge for providing the code for Bayesian inference. We thank Sigurjon Jonsson for reviewing the manuscript. Comments from three anonymous reviewers helped to improve the manuscript. This study was founded through ETH-grant TH-16/05-1.

Chapter 2

Bayesian imaging of the 2000 Western Tottori (Japan) earthquake through fitting of strong motion and GPS data

Published in Geophysical Journal International as:
Monelli, D., and Mai, P. M. and Jónsson, S. and Giardini, D. (2009), Bayesian imaging of the 2000 Western Tottori (Japan) earthquake through fitting of strong motion and GPS data, Geophys. J. Int., 176, 135-150

Abstract

We image the rupture process of the 2000 Western Tottori earthquake (M_w=6.6) through fitting of strong motion and GPS data. We consider an observational network of 18 strong motion and 16 GPS stations located within three fault lengths from the epicentre. We assume a planar fault and compute Green's functions for a 1D velocity model. The earthquake rupture is described as a shear dislocation parameterised in terms of peak slip-velocity, rake angle, rupture time and rise time, defined on a regular grid of nodes on the fault surface and derived at inner points through bilinear interpolation.

Our inversion procedure is based on a Bayesian approach. The solution of the inverse problem is stated in terms of a *posterior* probability density function (pdf) representing the conjunction of *prior* information with information contained in the data and in the physical law relating model parameters with data. Inferences on model parameters are thus expressed in terms of posterior marginal pdfs. Due to the non-linearity of the problem we use a Markov Chain Monte Carlo (MCMC) method based on the Metropolis algorithm to compute posterior marginals.

Except for a few cases posterior marginals do not show a Gaussian-like distribution. This prevents us from providing a mean model and from characterizing uncertainties in terms of standard deviations only. Resolution on each single parameter is analyzed by looking at the difference between prior and posterior marginal pdfs.

Posterior marginals indicate that the best resolved feature is a major slip patch (peak value of 311 ± 140 cm) located between the hypocentre and the top edge of the fault, centered at a depth of 4.5 km. This shallow slip patch is triggered about 3 s after the earthquake nucleated and required about 4 s to reach its final slip value. The presence of this shallow slip patch is common to all previous studies. In contrast to some previous studies we do not identify any significant slip (> 1 m) at the bottom of the fault.

We also compare inferences from both strong motion and GPS data with inferences derived from strong motion data only. In both cases the shallow slip patch is identified. At other locations, the main effect of the GPS data is in reducing the probability associated with high values of slip. GPS data reduce the presence of spurious fault slip and therefore strongly influence the resulting final seismic moment.

2.1 Introduction

The M_w=6.6 Tottori earthquake struck southwestern Japan on 6 October 2000, at 04:30:17.75 UTC. The hypocentre was located at 35.275 °N, 133.350 °E at a depth of 9.6 km [Fukuyama et al., 2003]. The best-fitting double-couple focal mechanism estimated by Fukuyama et al. [2003] indicates an almost pure left-lateral strike-slip event with a strike angle of 150° and a dip of 85° (Fig 2.1). No clear surface rupture was observed near the epicentre although some cracks oriented parallel to the estimated fault were found on a paved road [Umeda, 2002]. Systematic displacement of 10-20 cm was also found in a concrete lining, in a tunnel 200 m below the surface

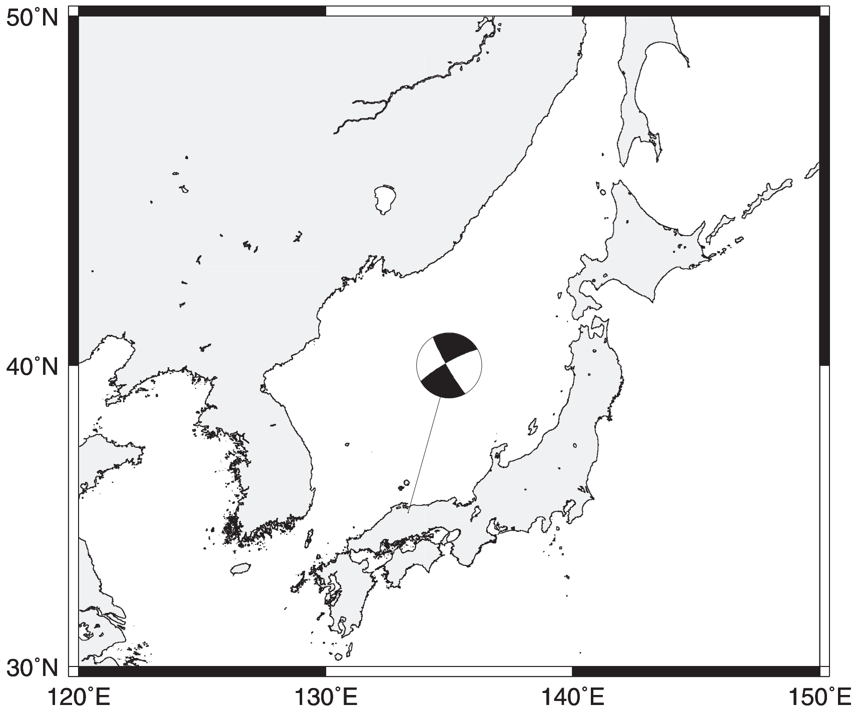

Figure 2.1: Location and focal mechanism for the 2000 Western Tottori earthquake [Fukuyama et al., 2003].

near the source region.

To reveal the details of the earthquake rupture process a number of studies derived kinematic images. Using a linearized frequency-domain method and an initial slip model obtained through GPS data inversion, Semmane et al. [2005] inverted strong motion data to infer values of slip amplitude, rupture time and rise time. They proposed different rupture models that all show a major slip patch located near the top edge of the fault (elongated towards southeast). Using strong motion data only and a backprojection method, Festa & Zollo [2006] inferred two major slip patches: one located above the hypocentre, close to the surface, extending southwards to the bottom of the fault; a second one located north of the hypocentre at depths between 10 and 18 km. Fitting simultaneously strong motion and GPS data and using a direct search method based on a simulated annealing algorithm, Piatanesi et al. [2007] estimated peak slip-velocity, rise time, rupture time and rake angle. They confirm the presence of a major slip patch between the hypocentre and the surface, but also identify an additional slip patch (2-2.5 m) located at the bottom of the fault.

A dynamic model of the rupture process has also been derived for the Tottori earthquake. Assuming constant upper yield stress and uniform slip-weakening distance, and using a direct search method based on the neighbourhood algorithm, Peyrat & Olsen [2004] inferred the distribution of stress drop over the fault surface by fitting strong motion data. The resulting slip pattern again shows that most of the slip is concentrated in the uppermost part of the fault.

All these proposed images are similar in their general features: They all show a high slip patch near the surface. However, the presence of slip at the bottom of the fault is ambiguous: it has been recognized by Festa & Zollo [2006] and Piatanesi et al. [2007], but not by Semmane et al. [2005]. Also the Peyrat & Olsen [2004] model does not require any slip at depth to fit the data, even though they consider a fault with a smaller depth extent compared to the ones used to obtain kinematic images.

One more aspect that has been investigated by both Semmane et al. [2005] and Piatanesi et al. [2007] is the rise time distribution on the fault surface. The model by Semmane et al. [2005] shows a highly heterogeneous pattern of rise time values that vary mostly between 0.5 and 2 s. Piatanesi et al. [2007]'s model shows a distribution that is instead more homogeneous (probably due to a coarser grid discretization and because they present a mean model) with rise time values varying mostly between 2.5 and 3.5 s. Clearly, these discrepancies can partially be due to the different approaches and parametrizations. However, no common features can be identified between the rise time distributions presented in these two studies, highlighting the intrinsic difficulty in imaging rise time in finite source inversions.

The Tottori earthquake is one of several examples where multiple rupture models have been proposed to explain the observed data. All models are similar in some aspects but their obvious differences require a better understanding of where this variability comes from. Are these discrepancies in the source images only due to different approaches and modeling assumptions or do they reveal some more fundamental lack of resolution?

Rupture-parameter estimates depend on how the inverse problem is stated, a well-known fact since the initial works of Olson & Apsel [1982] and Hartzell & Heaton [1983] who showed that results of linear slip inversions depend on the stabilization constraints and the data-set used. More recently, considering the 2004 Parkfield earthquake, Custodio et al. [2005] analyzed how kinematic rupture parameters depend on the chosen data-set, while Hartzell et al. [2007] showed how source-inversion results may depend on the definition of the misfit function, the bounds on model parameters, and the size of the model fault plane.

However, once a model parametrization, an inversion method and a data-set are chosen, uncertainties on model parameters are determined by errors in data, modeling, and finite data coverage. All these factors influence the topology of the misfit function and therefore its minimum. Every minimum is characterized by a certain local topology which determines the uncertainties on the corresponding model parameters. This is evident for the linear least-square problem where the covariance matrix for model parameters is proportional to the inverse of the 2^{nd} derivative of the misfit function at the minimum [Menke, 1989]: The sharper the minimum, the smaller the uncertainties. In case of non-linear problems the minimization problem may even have multiple solutions because the misfit function may have multiple (or degenerate) minima.

To estimate these uncertainties some methods have been proposed. Emolo &

Zollo [2005] used a genetic algorithm to search the model space and estimated resolution on the best-fitting model by defining a Gaussian probability density function centered around it. For each model parameter they derived a marginal probability density function by computing the objective function in the neighbourhood of the best-fitting model varying the parameter of interest but keeping all the remaining parameters fixed to their best-fitting values. With this approch the posterior probability density function is forced to be Gaussian around the best-fitting model and, more importantly, the computed marginals do not take into account the correlation between different model parameters. Peyrat & Olsen [2004], Corish et al. [2007] and Piatanesi et al. [2007] derived uncertainty estimates by statistically analyzing models generated by the optimization algorithm minimizing the misfit. The main drawback of this approach is that the statistical properties of a set of models, produced by optimization, do not necessarily represents the actual uncertainties (Sambridge [1999], Monelli & Mai [2008]), but rather the tuning parameters and the operators adopted by the algorithm.

The aim of this paper is to investigate the rupture process of the Tottori earthquake focusing on determining resolution on model parameters using a Bayesian approach (Mosegaard & Tarantola [1995], Tarantola [2005]). A Bayesian approach allows one to estimate uncertainties taking into account the non-linearity of the problem. It requires defining a posterior probability density function (pdf) on the model space representing the conjunction of our prior information with information contained in the data (strong motion and GPS data in this case), and in the physical law relating model parameters with data. Inferences on model parameters are then expressed in terms of posterior marginal pdfs. Due to the non-linearity and large-dimensionality of the problem, we use a Markov Chain Monte Carlo (MCMC) method based on the Metropolis algorithm to compute posterior marginals. Resolution on each model parameter is analyzed by looking at the difference between the corresponding prior and posterior pdfs. With this approach we can identify which regions of the fault surface are better illuminated by the data and which features of the rupture process can be considered well resolved.

2.2 The observational network

The observational network we use consists of 18 strong motion and 16 GPS stations located within about 90 km from the epicentre (Fig 2.2). Among the strong motion stations, we use 11 K-net stations and 7 KiK-net borehole stations (SMNH01 and SMNH02 at 101 m depth, TTRH04 at 207 m depth, OKYH07, OKYH08, OKYH09, OKYH14 at 100 m depth).

The strong motion data (available at http://www.kik.bosai.go.jp/) come as raw accelerations with absolute time. We band-pass filter the waveforms in the frequency range 0.1-1 Hz using a 1^{st} order band-pass Butterworth filter applied both in the forward and reverse directions to preserve phase. We then integrate the filtered waveforms to obtain ground velocities which we resample to a sampling interval

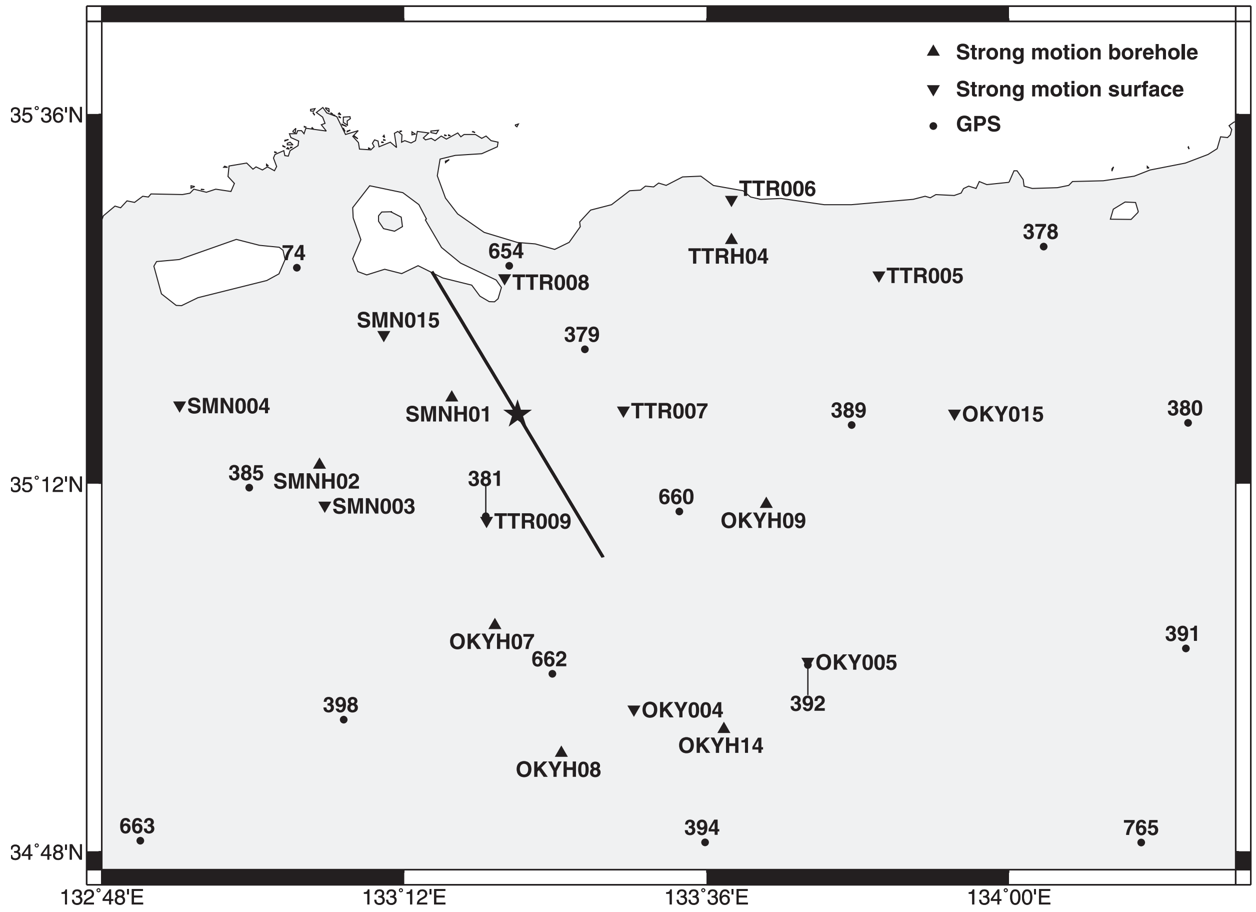

Figure 2.2: The observational network consists of 18 strong motion stations (black triangles) and 16 GPS stations (black dots) located within about 90 km from the epicentre (black star). We use 7 borehole stations (upward-pointing triangles) and 11 surface stations (downward-pointing triangles). The black solid line indicates the assumed fault strike (150°).

Table 2.1: Seismic velocity and density model for the Tottori region [Fukuyama et al., 2003].

$Depth\ (km)$	$V_p\ (km/s)$	$V_s\ (km/s)$	$\rho\ (g/cm^3)$
0.0	3.00	1.73	2.3
1.0	4.00	2.31	2.5
3.0	6.00	3.46	2.7
30.0	8.00	4.62	2.9

of 0.015 s. The horizontal components of station OKYH14 have been also rotated by 76° anticlockwise to correct for sensor misalignment. Each waveform lasts for 61.425 s and contains 4096 data points. Considering all components at all stations, the total number of waveform data points is therefore 221184.

The GPS stations belong to the GEONET array operated by the Geographical Survey Institute of Japan [Sagiya, 2004]. At each station, we define the coseismic static offset as the difference between the mean values of daily positions during the five days before and the five days after the earthquake. We also compute the corresponding standard deviations that we then propagate to compute the error on the final static displacement. For each station we consider both the two horizontal components and the vertical component, resulting in a total number of GPS data points of 48.

2.3 The forward modeling

We adopt a 1D piecewise-linear velocity- density-depth distribution based on the velocity model used by Fukuyama et al. [2003] for the mainshock location (Table 2.1). S-wave velocities are assumed to be $1/\sqrt{3}$ of the P-wave speed. Density values are deduced from P-wave velocities using the Gardner's relationship [Gardner et al., 1974].

We represent the fault as a 40 km long and 20 km deep, vertically dipping, plane surface with a strike of $150°$. The same strike and dip has been used by Peyrat & Olsen [2004], Festa & Zollo [2006] and Piatanesi et al. [2007]. The fault's upper edge is at 0.5 km depth, because coseismic surface rupture was essentialy absent. On the fault surface we define a regular grid of nodes with a spacing of 4 km along strike and along dip. The total number of nodes on the fault is therefore 66. At each node we define four parameters: peak slip velocity, rise time, rupture time and rake angle.

We compute ground velocities using the frequency-domain representation theorem [Spudich & Archuleta, 1987]:

$$\dot{u}_m\left(\mathbf{y},\omega\right)=\iint_{\Sigma}\dot{\mathbf{s}}\left(\mathbf{x},\omega\right)\cdot\mathbf{T^m}\left(\mathbf{x},\omega;\mathbf{y},\mathbf{0}\right)\mathbf{d\Sigma} \tag{2.1}$$

where $\dot{u}_m$ is the m^{th} component of ground velocity at the receiver location $\mathbf{y}$, $\dot{\mathbf{s}}$ is the slip-velocity function, $\mathbf{T^m}$ is the traction exerted across the fault surface Σ at point $\mathbf{x}$ generated by an impulsive force applied in the m^{th} direction at the receiver ($\omega = 2\pi f$: angular frequency). Tractions $\mathbf{T^m}$ are computed, up to a frequency of 1 Hz, using a Discrete Wavenumber / Finite Element method [Compsyn package, [Spudich & Xu, 2002]], for a 1D flat layered Earth model without attenuation. A trapezoidal-rule quadrature of the product $\dot{\mathbf{s}} \cdot \mathbf{T^m}$ is performed separately for each frequency, with the quadrature points being the sample points where $\mathbf{T^m}$ have been computed. Rupture-parameter values at integration points are derived through bilinear interpolation of values at surrounding grid nodes, similar to the approach taken by Liu & Archuleta [2004] and Piatanesi et al. [2007].

In this study we assume the slip-velocity function to be an isosceles triangle. With this parametrization the peak-slip velocity corresponds to the height of the triangle and the rise time to the base length. Rupture time corresponds to the first point of the base segment. With this parametrization rise time and rupture time are non-linearly related to ground velocity. Previous studies used different parametrizations, like a smooth ramp [Semmane et al., 2005] or a box-car function [Piatanesi et al., 2007].

Following Eq 2.1, we convolve tractions with the assumed slip-velocity function to compute ground velocity at the strong motion station locations. We compute GPS data predictions by integrating ground velocities to ground displacements and then selecting the final static offsets.

2.4 The Bayesian approach

In a Bayesian approach, inferences on model parameters (e.g. mean values, standard deviations, 1D/2D marginals) are derived from a posterior pdf defined on the model space. In section 2.4.1 we introduce the general equations defining the posterior pdf. We then apply these equations to our specific case, defining two different posteriors: one considering strong motion data only, and one considering both strong motion and GPS data. Our aim is to compare inferences from these two posteriors and analyze how GPS data influence the results. In section 2.4.2 we define the model space. We pay special attention to defining a physically consistent model space to avoid considering unrealistic models. Finally, we present the numerical scheme used to derive inferences on the model parameters (section 2.4.3).

2.4.1 The posterior pdf

We assume the M-dimensional model space and D-dimensional data space, $\mathbb{M}$ and $\mathbb{D}$ respectively, to be linear spaces. The prior probability density functions on model parameters and data are indicated with $\rho_M(\mathbf{m})$ and $\rho_D(\mathbf{d})$, respectively. $\theta(\mathbf{d}|\mathbf{m})$ denotes the conditional probability density representing the correlation between $\mathbf{d}$

and $\mathbf{m}$. The posterior pdf on the model space is given by [Tarantola, 2005]:

$$\sigma_M(\mathbf{m}) = k\rho_M(\mathbf{m})L(\mathbf{m}) \tag{2.2}$$

where k is a normalization constant and $L(\mathbf{m})$ is the likelihood function:

$$L(\mathbf{m}) = \int_{\mathbb{D}} d\mathbf{d}\; \rho_D(\mathbf{d})\theta(\mathbf{d}|\mathbf{m}) \tag{2.3}$$

which gives a measure of how well a model $\mathbf{m}$ explains the data.

In this study we assume that our prior knowledge consists only of the information that each model parameter is strictly bounded by two values m^{α}_{min} and m^{α}_{max}, where $\alpha \in I_M, I_M = \{1, ..., M\}$. We then write the prior pdf as:

$$\rho(\mathbf{m}) = \prod_{\alpha_M \in I_M} \rho_\alpha(m^\alpha) \tag{2.4}$$

where

$$\rho_\alpha(m^\alpha) = \begin{cases} \frac{1}{m^{\alpha}_{max} - m^{\alpha}_{min}} & \text{for } m^{\alpha}_{min} \leq m^\alpha \leq m^{\alpha}_{max} \\ 0 & \text{otherwise} \end{cases}$$

is the prior marginal for each model parameter (i.e. a uniform probability density function [Monelli & Mai, 2008]).

The common approach to define the likelihood function requires deriving a data covariance matrix for data uncertainties, and a modeling covariance matrix for uncertainties in the forward modeling. Assuming Gaussian uncertainties the likelihood function takes a Gaussian functional form where the associated covariance matrix is the sum of the data and modeling covariance matrices (Gouveia & Scales [1998], Tarantola [2005]).

Because we consider two different data sets (strong motion and GPS data) we define two distinct likelihood functions. For the strong motion data we do not have a complete estimate of the associated uncertainties. Strong motion data represent a single measurement of the ground motion produced by an earthquake, and we therefore have a single realization of the data errors. A possible approach to still derive a data covariance matrix would be to analyze the portion before the P-wave arrival of each trace and to assume this portion to be representative of the seismic noise. More problematic is to derive the modeling covariance matrix, which would require knowing the uncertainties in the velocity and fault models (unknown in our case) and then propagating them into the Green's functions used to compute the predicted ground motion.

Due to the difficulty of deriving a realistic covariance matrix for strong motion data, we propose an alternative approach. First, we assume a "perfect instrument" condition [Tarantola, 2005]. This assumption is valid if data uncertainties are negligible compared to modeling uncertainties. We propose this approach for the strong motion waveforms considered in this study, for which we find high signal-to-noise ratios thanks to the vicinity of the recording stations with respect to the source and the magnitude of the event. This assumption translates into the following condition:

$$\rho^{sm}_D(\mathbf{d}) = \delta(\mathbf{d} - \mathbf{d}^{obs}) \tag{2.5}$$

where $\rho_D^{sm}(\mathbf{d})$ represents prior knowledge on strong motion data and $\mathbf{d}^{obs}$ represents the observed data.

We define now the correlation $\theta(\mathbf{d}|\mathbf{m})$ between data and model parameters. Due to our lack of knowledge of the amplitude and type of uncertainites affecting our modeling we cannot derive $\theta(\mathbf{d}|\mathbf{m})$ from a formal theory. We therefore propose an empirical formulation. Using an optimization algorithm we examine which model produces the best fit given the observed data. We then use this information to define a correlation function that assigns to each model $\mathbf{m}$ a correlation value that depends on how well it fits the data with respect to the level of fit produced by the best-fitting model. Models producing a level of fit close to the one of the best fitting models should then have a higher value of correlation than models producing a worse level of fit. Indicating with $\phi(\mathbf{d}, \mathbf{m})$ the percentage difference between the misfit produced by a model $\mathbf{m}$ and the misfit produced by the best-fitting model $\mathbf{m}^{best}$ (which depends on the data $\mathbf{d}$), we obtain:

$$\phi(\mathbf{d}, \mathbf{m}) = \frac{S(\mathbf{m}) - S(\mathbf{m}^{best}(\mathbf{d}))}{S(\mathbf{m}^{best}(\mathbf{d}))} \cdot 100 \tag{2.6}$$

where S indicates the misfit function used, and $\mathbf{m}^{best}(\mathbf{d})$ represents the best-fitting model given data $\mathbf{d}$. We define the correlation between (strong motion) data and model parameter as:

$$\theta^{sm}(\mathbf{d}|\mathbf{m}) = \begin{cases} c & , \forall \mathbf{m} \in \mathbb{M} : \phi(\mathbf{d}, \mathbf{m}) < 0 \\ c \exp[-\phi(\mathbf{d}, \mathbf{m})], & \forall \mathbf{m} \in \mathbb{M} : \phi(\mathbf{d}, \mathbf{m}) \geq 0 \end{cases} \tag{2.7}$$

where c is a normalization constant. Equation 2.7 predicts that for all models producing a lower misit value then the best-fitting model the correlation assumes its maximum value. This condition accounts for the possibility that the best-fitting model found during the optimization process may not correspond to the absolute misfit minimum. For all other models the value of the correlation decreases exponentially depending on the percentage difference between the generated misfit and the minimum misfit associated with the best-fitting model. In writing eq 2.7 we follow the analogy with a Gaussian correlation function. When assuming Gaussian modeling uncertainties , the correlation function $\theta(\mathbf{d}|\mathbf{m})$ assumes an exponential functional form where the argument is the L_2 norm of the data misfit weighted by the modeling covariance matrix. In our study we keep the exponential functional form, but we substitute the argument with eq 2.6. Inserting equations 2.5 and 2.7 into equation 2.3, the integration yields:

$$L^{sm}(\mathbf{m}) = \begin{cases} c & , \forall \mathbf{m} \in \mathbb{M} : \phi(\mathbf{d}^{obs}, \mathbf{m}) < 0 \\ c \exp[-\phi(\mathbf{d}^{obs}, \mathbf{m})], & \forall \mathbf{m} \in \mathbb{M} : \phi(\mathbf{d}^{obs}, \mathbf{m}) \geq 0 \end{cases} \tag{2.8}$$

where $L^{sm}(\mathbf{m})$ represents the likelihood function for strong motion data.

For GPS data we define a data covariance matrix. As described in section 2.2, we define the observed static offset as the difference between the mean values of daily positions during the five days before and after the earthquake. By computing the corresponding standard deviations we can deduce the standard deviation on the final static displacement. Assuming uncorrelated uncertainties we then define a covariance matrix for GPS data which is a diagonal matrix of data variances. Assuming Gaussian uncertainties the prior pdf on (GPS) data is:

$$\rho_D^{gps}(\mathbf{d}) = C \exp\left[-\frac{1}{2}(\mathbf{d}-\mathbf{d}^{obs})^T \mathbf{C}_{d,gps}^{-1}(\mathbf{d}-\mathbf{d}^{obs})\right] \tag{2.9}$$

where C is a normalization constant and $\mathbf{C}_{d,gps}$ is the data covariance matrix for GPS data.

As for the strong motion data, the modeling covariance matrix for uncertainties in the predicted GPS displacement requires knowing the uncertainties in the velocity and fault models. However GPS data, measuring a static offset, reflect the zero frequency component of the wavefield which is less sensitive to complexities in the velocity model. Also, GPS data seems to be well explained even using a simple planar fault [Piatanesi et al., 2007]. We hence assume for GPS data to have neglible uncertainties in the forward modeling. This assumption translates into the following condition:

$$\theta^{gps}(\mathbf{d}|\mathbf{m}) = \delta(\mathbf{d}-\mathbf{g}(\mathbf{m})) \tag{2.10}$$

where $\mathbf{g}(\mathbf{m})$ is the forward modeling operator. Inserting equations 2.9 and 2.10 into equation 2.3, the result of the integration is:

$$L^{gps}(\mathbf{m}) = C \exp\left[-\frac{1}{2}\mathbf{r}^T \mathbf{C}_{d,gps}^{-1}\mathbf{r}\right] \tag{2.11}$$

where $L^{gps}(\mathbf{m})$ represents the likelihood function for GPS data and $\mathbf{r} = \mathbf{g}(\mathbf{m}) - \mathbf{d}^{obs}$.

Considering equation 1.1 we can define a posterior pdf representing the conjunction of our prior information with information contained in strong motion data:

$$\sigma_M^{sm}(\mathbf{m}) = k\rho_M(\mathbf{m})L^{sm}(\mathbf{m}). \tag{2.12}$$

Equation 2.12 can then be used as prior information to define a new posterior pdf for the model parameters, which also considers the GPS data:

$$\sigma_M^{sm,gps}(\mathbf{m}) = k\rho_M(\mathbf{m})L^{sm}(\mathbf{m})L^{gps}(\mathbf{m}). \tag{2.13}$$

2.4.2 The model space

The posterior pdf is defined over the model space. Inferences on model parameters are therefore dependent on the chosen model space. A correct definition of the model space is of vital importance to avoid testing unrealistic models that make the inference process ineffiicent. We thus pay special attention to defining a physically consistent model space.

In our inversion we assume the peak slip-velocity (and therefore the slip) to be zero at the fault edges. Non-zero slip at the fault boundaries would constitute a discontinuity in slip that lead to unrealistically high values of stress change at the edges. This condition is assumed to be valid also for the top edge of the fault, because no surface rupture was reported for the Tottori earthquake. For the inner nodes the peak slip-velocity is allowed to vary between 0 and 400 cm/s. With these conditions we generate peak slip-velocity distributions with non-zero values only inside the fault and tapered to zero at the edges.

The moment tensor solution for the Tottori earthquake indicates an almost pure left-lateral strike slip event [Fukuyama et al., 2003]: nevertheless we allow the rake angle to vary between -30° to +30° degrees at each node. Positive angles indicate a down-dip component whereas negative angles an up-dip component.

The range of rupture times at each grid node is defined as the time interval between the arrival times of two circular rupture fronts propagating from the hypocentre (at 9.6 km depth) at two limiting rupture velocities: 1.5 km/s and 4 km/s.

The range of possible values for rise time has been chosen according to the frequency band used in the inversion. Having band-pass filtered the waveforms in the frequency band 0.1-1 Hz we consider as minimum and maximum values for rise time 1 and 10 s respectively. However, from dynamic rupture simulations (Day [1982], Madariaga et al. [1998]) it is known that when a rupture front reaches the unbreakable boundaries of a fault it generates stopping phases that propagate inwardly and heal the slip process as they spread over the fault. As a consequence the duration of slip at fault locations is influenced by the stopping phases emitted from the edges of the fault. In our case the hypocentre is located approximately in the center of the assumed fault plane; we may therefore expect that the inner portion of the fault will start slipping earlier and will be reached by the stopping phases, later than regions near the borders of the fault. For this reason, the minimum allowed rise time is assumed to be 1 s for each node, while the maximum allowed rise time is assumed to decrease from the maximum value (10 s) according to the following equation:

$$\tau_r^{max,n} = \tau_r^{min} + (\tau_r^{max} - \tau_r^{min})(1 - \frac{d_{hyp}^n}{d_{hyp}^n + d_{bound}^n}) \tag{2.14}$$

where $\tau_r^{max,n}$ is the maximum rise time at the node n, τ_r^{min} and τ_r^{max} are the minimum and maximum rise time values allowed by the considered frequency range, d_{hyp}^n is the distance of the node n from the hypocentre, and d_{bound}^n is the minimum distance of the node n from the boundaries of the fault. This equation predicts that the maximum allowed rise time is equal to 10 s only for a node at the hypocentre ($d_{hyp}^n = 0$) and that for all the nodes on the boundaries ($d_{bound}^n = 0$) the maximum rise time corresponds to the minimum allowed rise time. For all remaining nodes the maximum rise time decreases as their distance from the boundary decreases (Fig 2.3). For the nodes having the same minimum distance (e.g. nodes 14, 15, 16, 17) the maximum allowed rise time decreases with increasing distance from the hypocentre. Eq 2.14 only predicts the maximum allowed rise time at each node and expresses the fact that long rise times are not expected near the borders of the fault simply because stopping phases are expected to reduce the duration of the slip process in these locations. The minimum rise time is everywhere 1 s. Between the minimum and maximum allowed rise time values the prior pdf assumes uni-

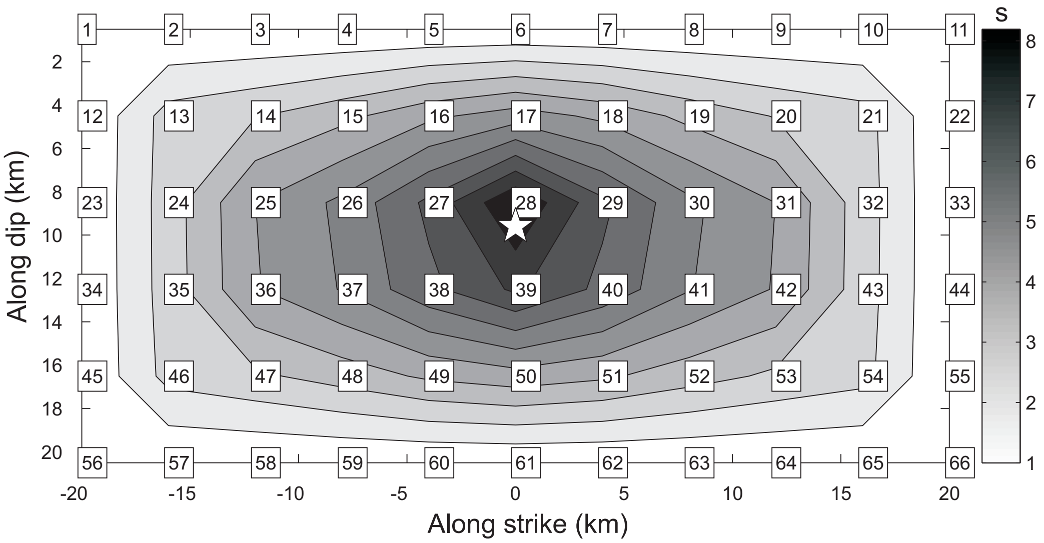

Figure 2.3: The maximum allowed rise time (s) on the fault surface. Numbered labels indicate node locations. The white star represents the hypocentre location.

form probability at each node. In other words, a crack-like rupture behaviour or a pulse-like propagation are assumed to be equally likely.

2.4.3 Sampling the posterior pdf

Once the posterior pdf and the model space are defined, information on each model parameter m^α can be quantified by computing the corresponding 1D marginal posterior pdf:

$$M(m^\alpha) = \int ... \int \sigma_M(\mathbf{m}) \prod_{\substack{k=1 \\ k \neq \alpha}}^{M} dm^k \tag{2.15}$$

Eq 2.15 involves computing the integral of the posterior pdf over all dimensions of the model space except the one corresponding to the parameter of interest. Due to the large dimensionality of the problem (204 model parameters) Eq 2.15 can be estimated only using Monte Carlo methods that generate models $\mathbf{m}$ as samples of the posterior pdf $\sigma_M(\mathbf{m})$. Once a large ensemble of such samples has been generated the 1D marginal of each parameter can be approximated by the histogram of the corresponding sampled values.

Among the different possible sampling algorithms (for a review see Tarantola [2005]), we use a Markov Chain Monte Carlo (MCMC) method based on the Metropolis algorithm (Martinez & Martinez [2002], Tarantola [2005]). A Markov chain is a sequence of random variables $\mathbf{m}_1, \mathbf{m}_2, ..., \mathbf{m}_t$, such that the next value or state of the sequence $\mathbf{m}_{t+1}$ depends only on the previous one $\mathbf{m}_t$. An MCMC method based on the Metropolis algorithm generates a Markov chain where the state of the chain at $t+1$ is obtained by sampling a *candidate point* $\tilde{\mathbf{m}}$ from a symmetric

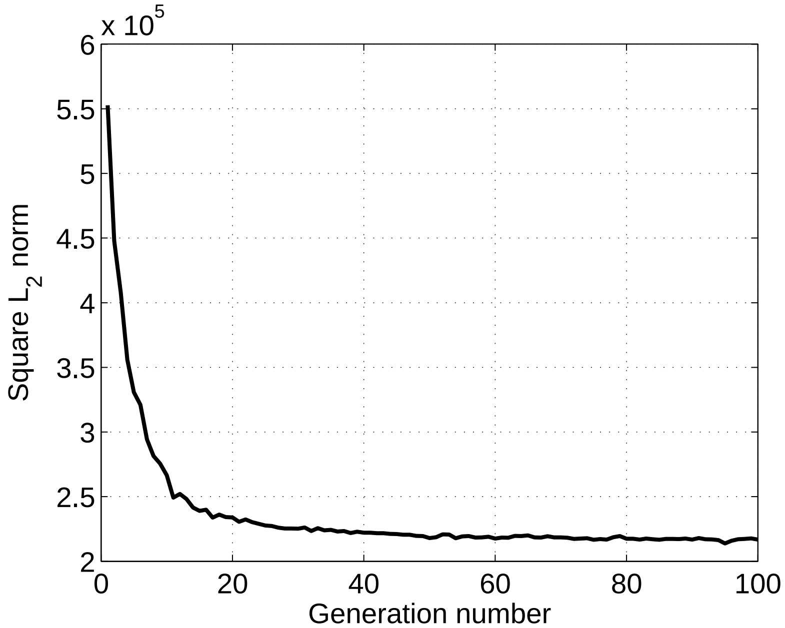

Figure 2.4: Misfit reduction during the search. After about the 40th generation the level of fit reaches an approximately stationary level.

proposal distribution $q(.|\mathbf{m}_t)$. An example of a distribution like this is the normal distribution with mean $\mathbf{m}_t$ and fixed covariance. In order to generate variables that are samples of a given pdf P, the candidate point is accepted as the next state of the chain with a probability given by:

$$\alpha(\mathbf{m}_t, \tilde{\mathbf{m}}) = min\left\{1, \frac{P(\tilde{\mathbf{m}})}{P(\mathbf{m}_t)}\right\}. \tag{2.16}$$

This means that if $P(\tilde{\mathbf{m}}) \geq P(\mathbf{m}_t)$, that is if the proposed model corresponds to an higher value of the target pdf, the move is always accepted because $\alpha(\mathbf{m}_t, \tilde{\mathbf{m}})$ will be equal to one. In the opposite case, if the move produces a lower value of the target pdf the proposed model is accepted with probability given by $\frac{P(\tilde{\mathbf{m}})}{P(\mathbf{m}_t)}$. If the point $\tilde{\mathbf{m}}$ is not accepted, then the chain does not progress and $\mathbf{m}_{t+1} = \mathbf{m}_t$.

Our aim is to generate models that are samples of the posterior pdf. In our case the posterior pdf is given by the product of several pdfs (in case of $\sigma_M^{sm,gps}(\mathbf{m})$, the prior and the likelihoods for strong motion and GPS data). Using a general notation we write:

$$\sigma_M(\mathbf{m}) = kP_1(\mathbf{m})P_2(\mathbf{m})P_3(\mathbf{m}). \tag{2.17}$$

To generate samples according to the posterior defined in equation 2.17 we use the Cascaded Metropolis algorithm [Tarantola, 2005]. We start by defining a random walk that generates samples according to the first pdf. At a given step the random walker is at point $\mathbf{m}_t$ (which is a sample of P_1). Using a proposal distribution we generate a model $\tilde{\mathbf{m}}$. We accept the new model as a next step of the random walk according to the following rules:

(a) if $P_2(\tilde{\mathbf{m}}) \geq P_2(\mathbf{m}_t)$, then go to step (c).

(b) if $P_2(\tilde{\mathbf{m}}) < P_2(\mathbf{m}_t)$, then decide randomly to go to step (c) or to reject the proposed model with a probability to go to step (c) given by $\alpha = P_2(\tilde{\mathbf{m}})/P_2(\mathbf{m}_t)$.

(c) if $P_3(\tilde{\mathbf{m}}) \geq P_3(\mathbf{m}_t)$, then accept the new model.

(d) if $P_3(\tilde{\mathbf{m}}) < P_3(\mathbf{m}_t)$, then decide randomly to accept a new model or to stay at $\mathbf{m}_t$ with a probability to accept the new model given by $\alpha = P_3(\tilde{\mathbf{m}})/P_3(\mathbf{m}_t)$.

2.5 Results

In section 2.4.1 we defined the posterior pdfs $\sigma_M^{sm}(\mathbf{m})$ (Eq 2.12), for strong motion data, and $\sigma_M^{sm,gps}(\mathbf{m})$ (Eq 2.13), for both strong motion and GPS data. We now present the corresponding estimated maximum likelihood models, and compare their predictions with the observed data (section 2.5.1). Then we compute the corresponding 1D marginals and analyze how GPS data change inference results (section 2.5.2). In section 2.5.3 we finally compute 2D marginals for a number of model parameters and investigate possible correlations.

2.5.1 The maximum likelihood models

The maximum likelihood model for $\sigma_M^{sm}(\mathbf{m})$ corresponds to the model maximizing the likelihood function $L^{sm}(\mathbf{m})$. By definition (equations 2.6 and 2.7) the maximum is attained in correspondence with the best-fitting model. Given a model $\mathbf{m}$ we measure the level of fit with strong motion data using a L2 norm of the misfit between observed and predicted waveforms in the time domain. We explore the model space to identify the best-fitting model using a direct search method based on an evolutionary algorithm (Beyer [2001], Monelli & Mai [2008]). An evolutionary algorithm is a population-based stochastic optimization method. According to this algorithm the search of the model space starts with generating an initial set of models which is obtained through a uniform random sampling of the model space. This initial population then evolves through the subsequent application of both stochastic and deterministic operators. Goal of these operators is to generate a new population of models that hopefully show better properties (i.e. lower misfit values). The creation of a new population is referred as a new generation.

We consider an initial population of 100 models from which we produce at each generation 2000 new models. The search lasts for 100 generations, and the total number of models produced is therefore 200100. The best objective function value for each generation versus the generation number is shown in Fig 2.4. We can see that after the 40th generation the level of fit reaches an approximately stationary level. The best-fitting model (generating the lowest misfit function value) is shown in figure 2.5.

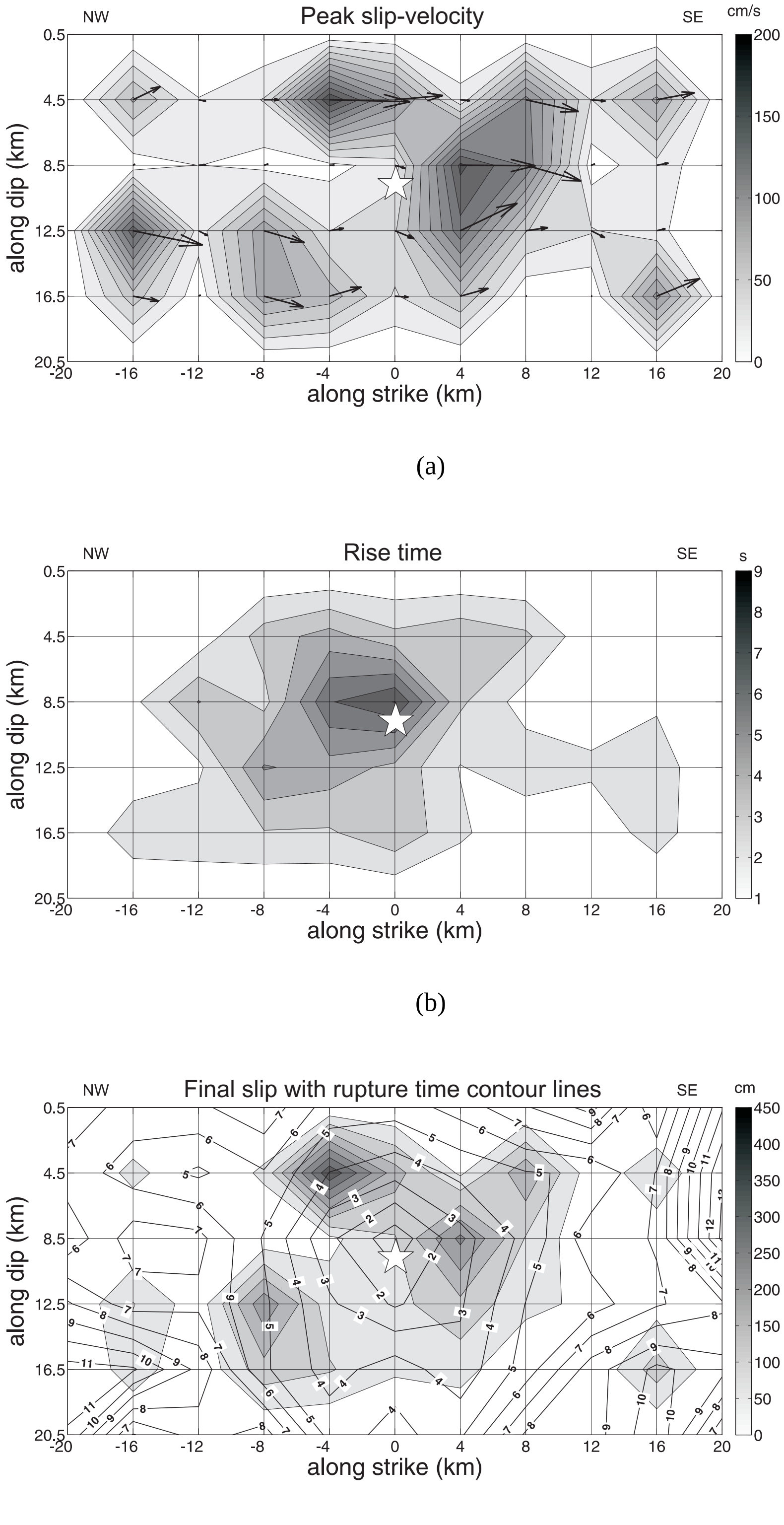

Figure 2.5: Peak slip velocity vector (cm/s) (a), rise time (s) (b) and final slip (cm) (c) distributions (with rupture time contour lines every 1 s) of the maximum likelihood models for σ_M^{sm}. The grid indicates the subfault discretization. The white star represents the hypocentre location.

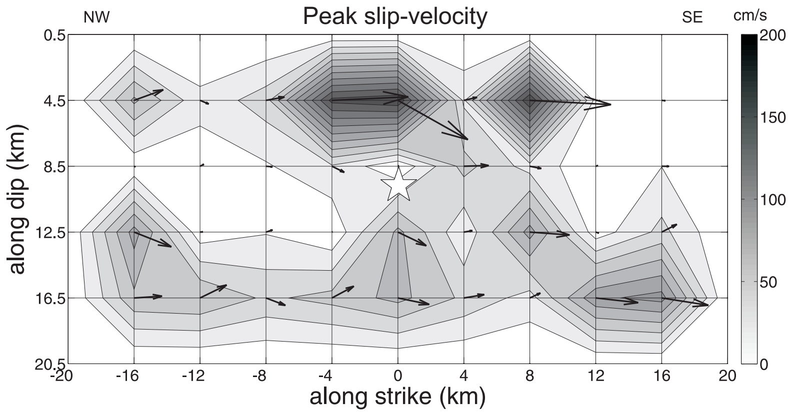

(a)

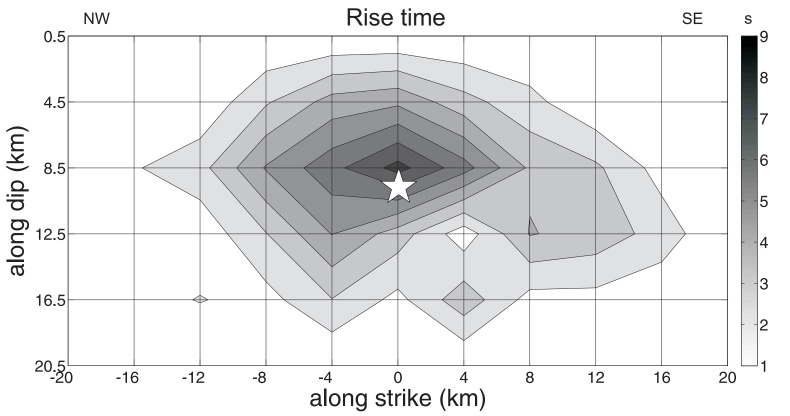

(b)

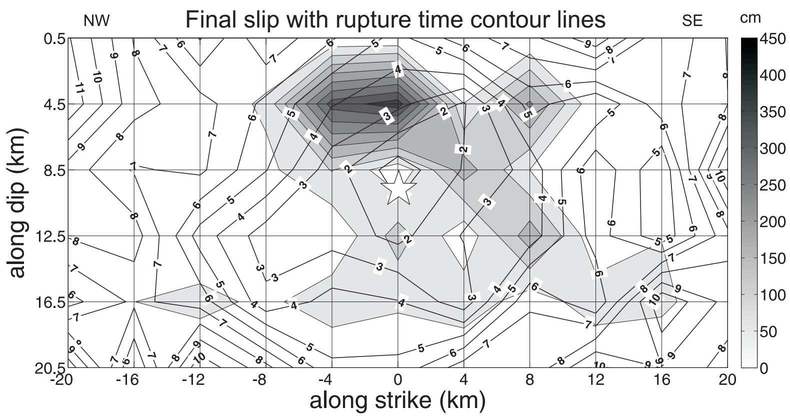

(c)

Figure 2.6: Peak slip velocity vector (cm/s) (a), rise time (s) (b) and final slip (cm) (c) distributions (with rupture time contour lines every 1 s) of the maximum likelihood models for $\sigma_M^{sm,gps}$. The grid indicates the subfault discretization. The white star represents the hypocentre location.

The maximum likelihood model for $\sigma_M^{sm,gps}$ (Fig 2.6) corresponds to the model minimizing the sum of the exponents of the two likelihood functions, $L^{sm}(\mathbf{m})$ and $L^{gps}(\mathbf{m})$. We identify it among the models visited during the sampling process which we describe in detail in section 2.5.2.

Comparing the two rupture models we can see that both of them present several high slip-velocity patches. In both cases we can identify a high slip-velocity patch between the hypocentre and the top edge of the fault (at 4.5 km depth). The maximum-likelihood model for σ_M^{sm} presents significant peak slip-velocity SE of the hypocentre, which is not observed in the maximum-likelihood model for $\sigma_M^{sm,gps}$. The latter presents also a low peak slip-velocity region NW of the hypocentre which is also visible, but less extensive, in the maximum likelihood model for σ_M^{sm}.

In both cases, the rise time pattern shows higher values near the hypocentre and lower values near the borders, following approximately the pattern of the maximum allowed rise time.

In comparing the final slip distributions, we notice in both cases a high slip patch (maximum value about 4 m) between the hypocentre and the top edge of the fault, with an elongation of the slip distribution towards SE. The major difference concerns the presence of deep slip. The maximum-likelihood model for $\sigma_M^{sm,gps}$ presents little slip at the bottom of the fault, especially in the NW, while the maximum-likelihood model for σ_M^{sm} contains instead more deep slip.

The seismic moments of the maximum-likelihood models for σ_M^{sm} and $\sigma_M^{sm,gps}$ are 1.9×10^{19} Nm and 1.6×10^{19} Nm, respectively. Semmane et al. [2005] inferred values of seismic moment between $1.5 - 1.7 \times 10^{19}$ Nm, Festa & Zollo [2006] 2.6×10^{19} Nm and Piatanesi et al. [2007] 1.7×10^{19} Nm.

In Fig 2.7 and 2.8 we show the level of fit produced by both models with the observed strong motion data. For some components both models reproduce the polarity of the first arrival and the amplitude and duration of the main phase (see fault parallel component at stations SMN003, SMN015, TTR005, SMNH01, SMNH02, TTRH04 for instance). For some other components the forward modeling does not reproduce the observed complexity (see waveforms at station TTR008 for instance). Both models produce a similar level of fit. Without any uncertainty characterization we cannot say which model is performing better in reproducing the observed strong motion data.

In Fig 2.9 we compare the horizontal static displacement produced by both models with the one deduced from GPS data. Ellipses represent 95 percent confidence level. We notice that at some stations (74, 379, 660, 662, 381) the static displacement produced by the maximum likelihood model for σ_M^{sm} lies just on or slightly outside the error ellipse. The maximum likelihood model for $\sigma_M^{sm,gps}$ instead reproduces the observed surface displacements within the estimated displacement error at all stations.

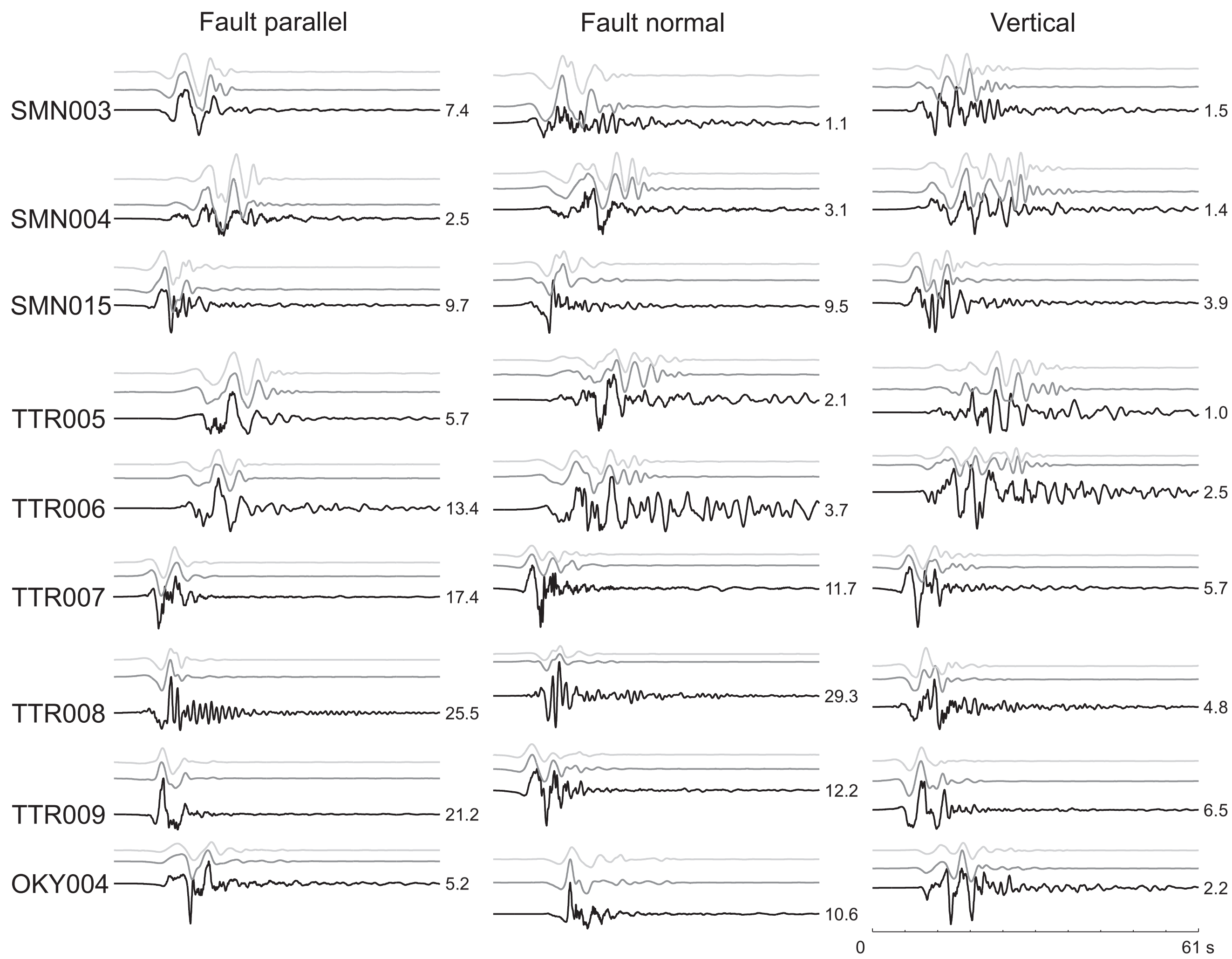

Figure 2.7: Level of fit produced by the maximum likelihood models for σ_M^{sm} (dark gray) and $\sigma_M^{sm,gps}$ (light gray) with the observed ground motion (black). The maximum observed ground velocity (cm/s) is shown at the end of each trace. Waveforms are not normalized. For each component, the vertical spacing between two subsequent traces is equal to the maximum positive amplitude of the lower trace.

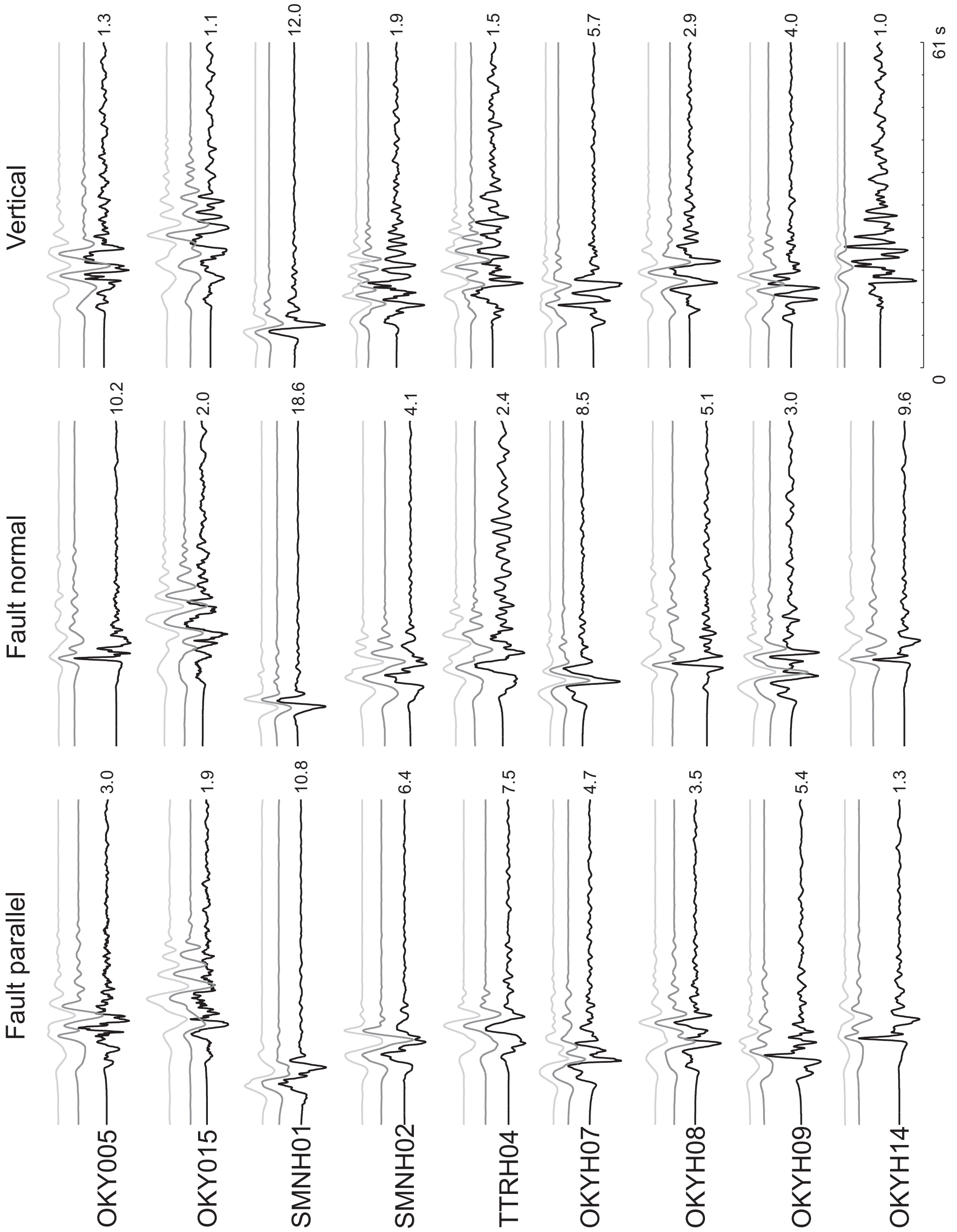

Figure 2.8: Continuation of Fig 2.7.

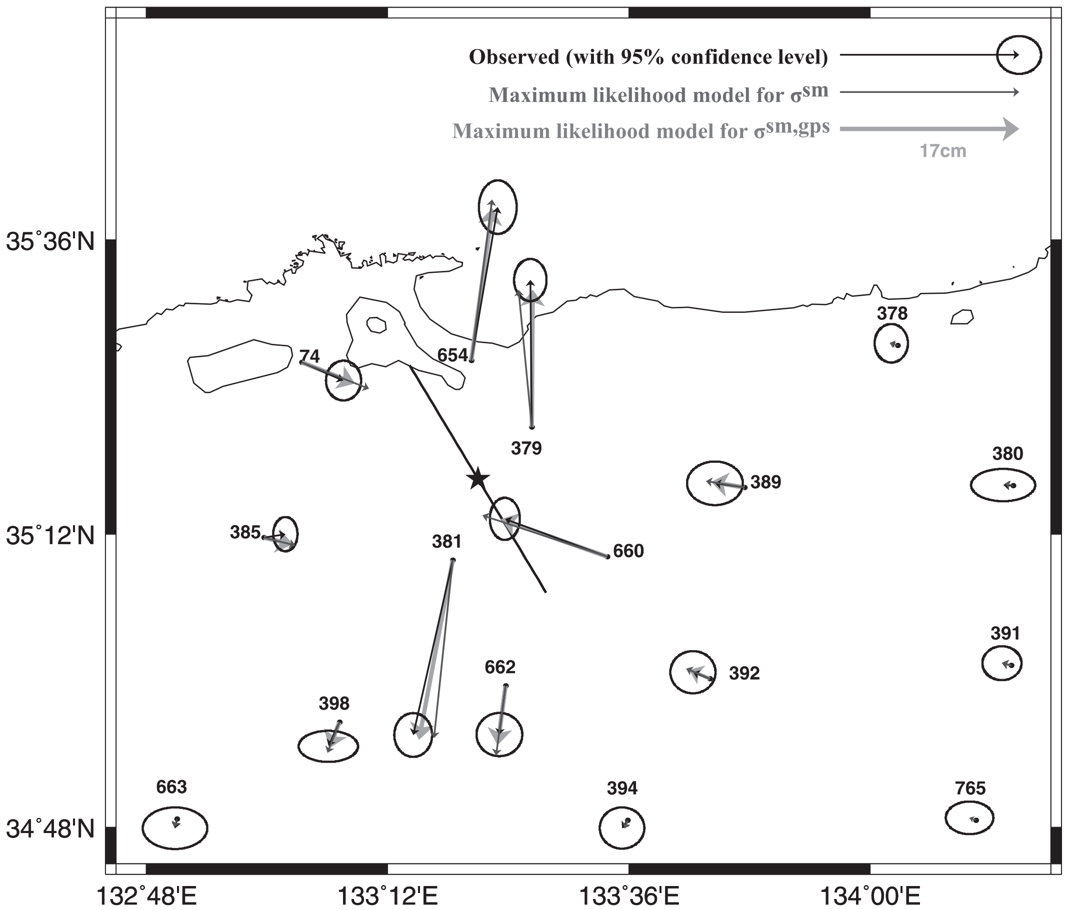

Figure 2.9: Horizontal static displacement predicted by the maximum likelihood models for σ_M^{sm} (thin dark gray) and $\sigma_M^{sm,gps}$ (thick light gray) compared with the observed one (thin black). Ellipses represent 95 percent confidence levels.

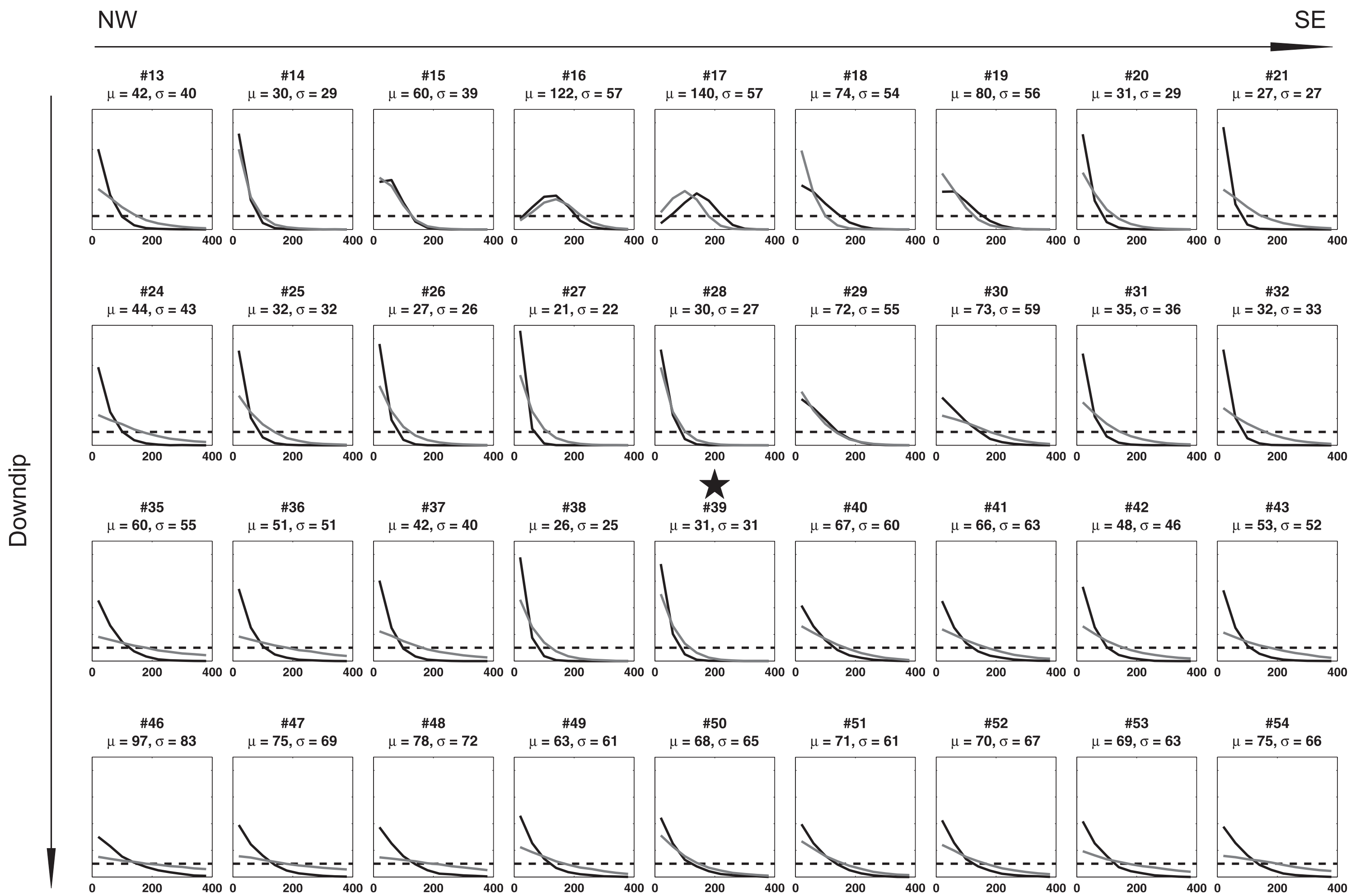

Figure 2.10: 1D marginals for peak slip-velocity (cm/s). Each subplot corresponds to a node position. Dashed lines represent priors, solid lines posterior marginals (gray from σ_M^{sm}, black from $\sigma_M^{sm,gps}$). For each subplot we indicate node number, posterior mean value (μ) and standard deviation (σ) of the posterior marginal obtained from $\sigma_M^{sm,gps}$. The black star represents the hypocentre location.

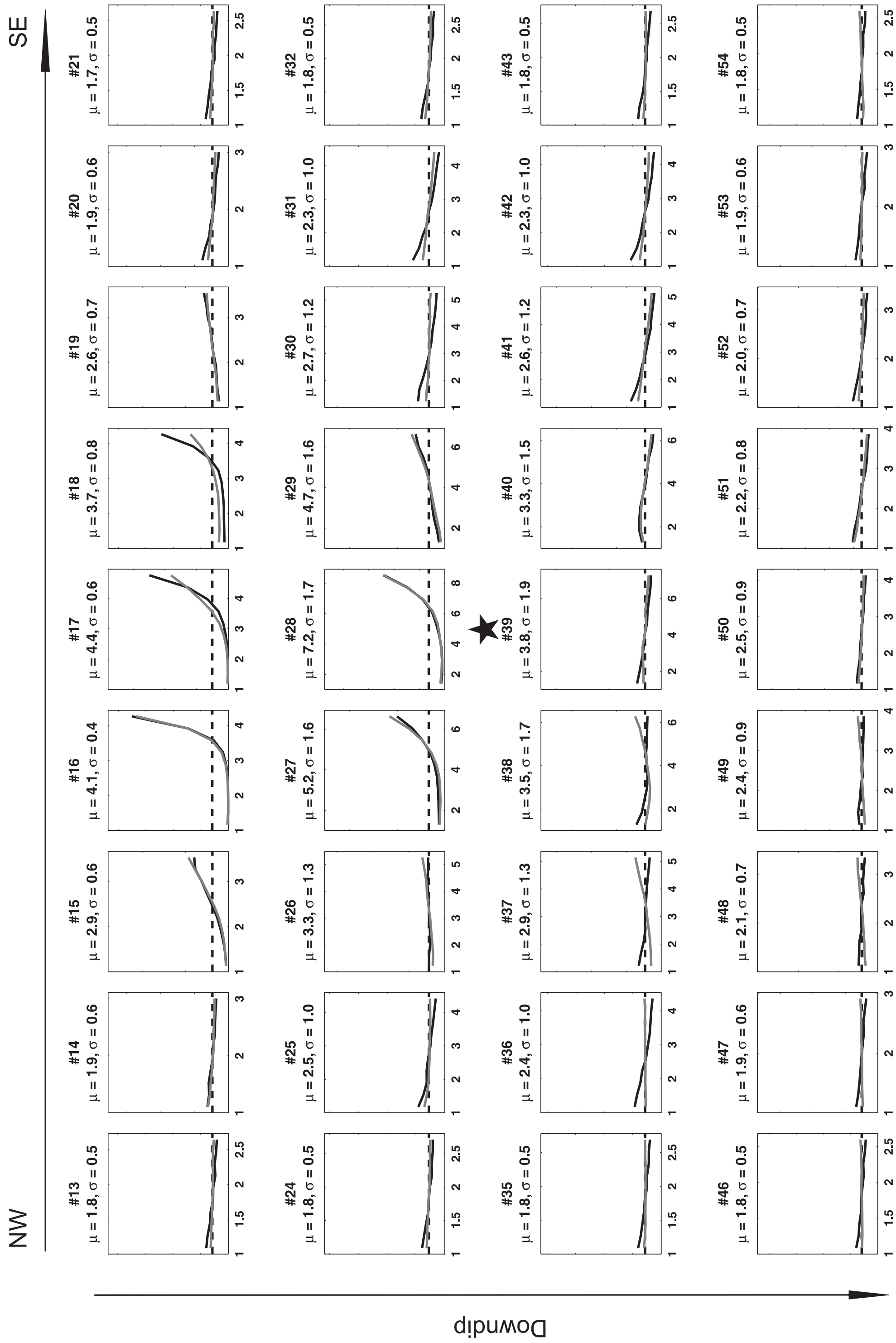

Figure 2.11: 1D marginals for rise time (s). Same notation as in Fig 2.10

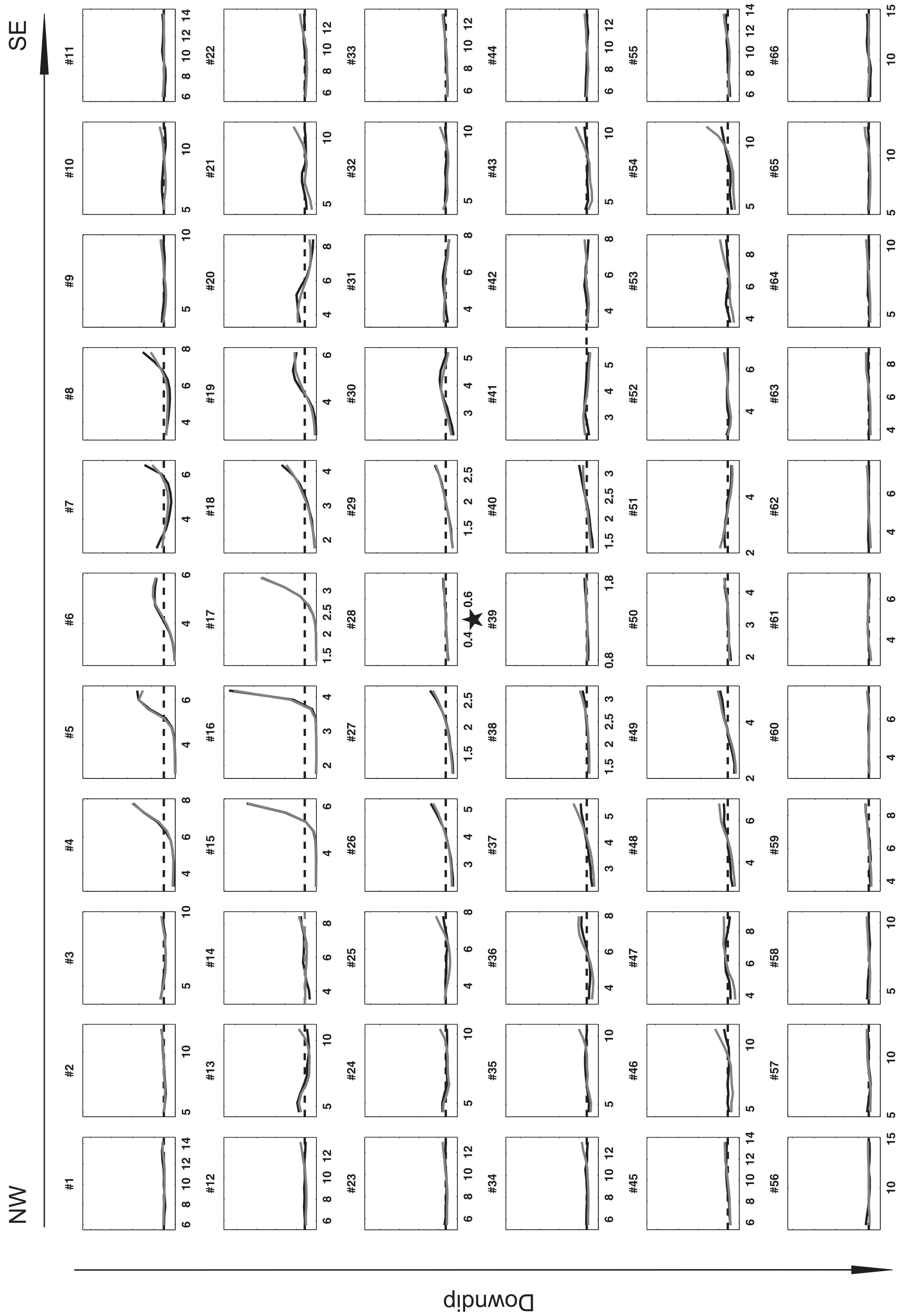

Figure 2.12: 1D marginals for rupture time (s). Same notation as in Fig 2.10

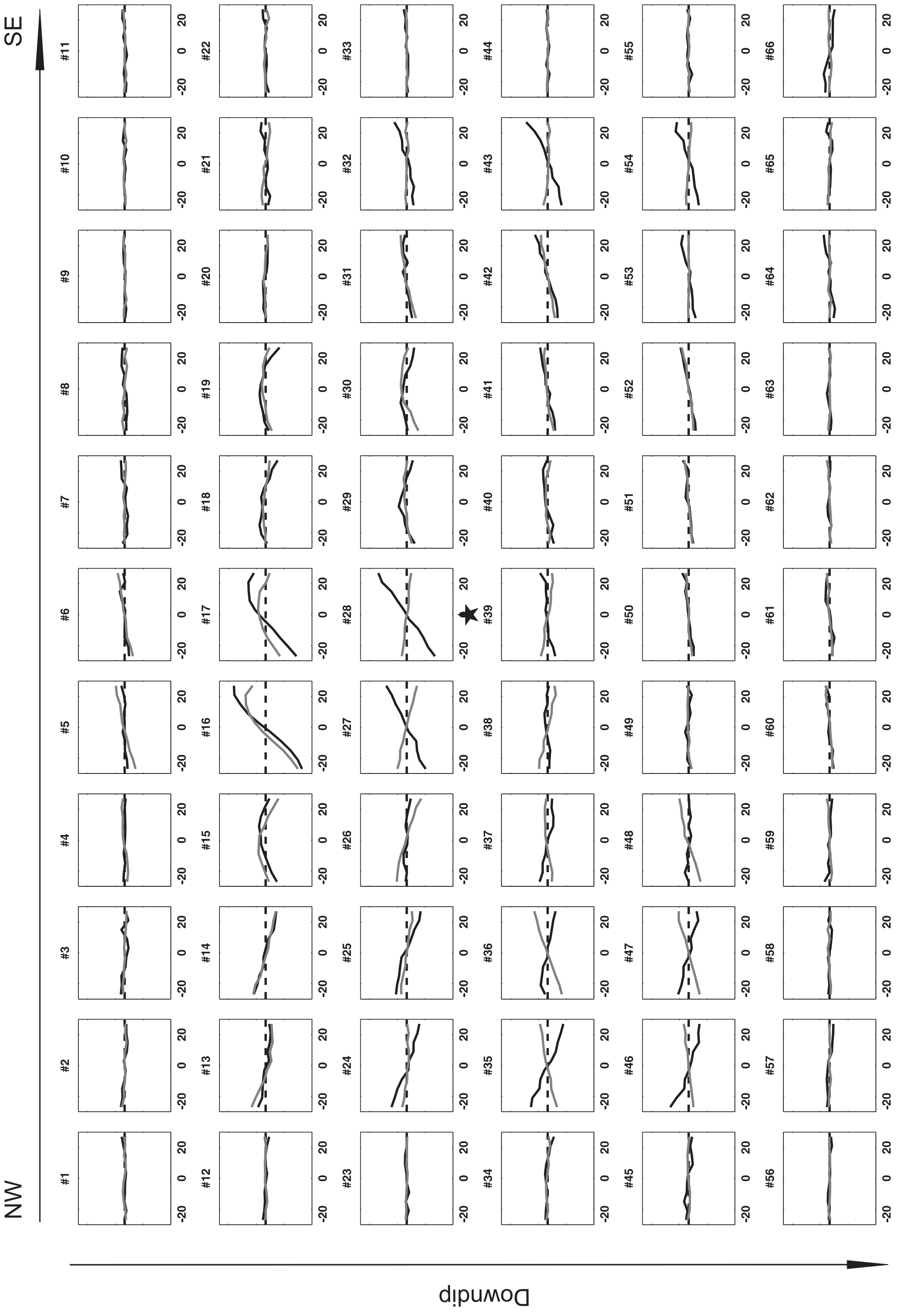

Figure 2.13: 1D marginals for rake angle (degree). Same notation as in Fig 2.10

2.5.2 The 1D marginals

According to section 2.4.3 we express our inferences on the investigated rupture parameters in terms of marginal pdfs derived from the two posterior pdfs defined in eqs 2.12 and 2.13.

Following the algorithm described in section 2.4.3 we simulated, for both cases, four random walks starting from different models obtained through uniform random sampling of the model space. Each random walk has also a different seed value for the random number generator. At each step we generate a new model using a Gaussian probability distribution with fixed covariance matrix. We assume the covariance matrix to be diagonal with standard deviations equal for parameters of the same type. After several trial random walks we fix the standard deviations for peak slip velocity, rake angle, rupture time and rise time to be 5 cm/s, 2°, 0.1 s, and 0.1 s, respectively. With these values the acceptance rate of the Metropolis algorithm (ratio between accepted and generated models) is $\sim$50 per cent when sampling σ_M^{sm} and $\sim$30 per cent when sampling $\sigma_M^{sm,gps}$. Tarantola [2005] suggests that the size of the perturbations in the model space should give an acceptance rate of $\sim$30-50 per cent.

Models produced by the Metropolis sampler are not independent samples of the posterior pdf since each model depends on the previous one. However, the estimation of the integral in equation 2.15 requires independent samples. Only with n independent samples can equation 2.15 be approximated as accurately as needed by increasing n [Martinez & Martinez, 2002]. After taking one sample, a possible strategy to generate a new independent sample is to wait a sufficient number of moves before collecting a new sample, such that the random walk has "forgotten" the previous sample. Unfortunately no general rule exists that helps to set the number of moves that should be done before collecting a new sample [Tarantola, 2005]. From a practical point of view, this parameter is also dependent on the computation time available. After some experimentation we decided to collect samples every 100 steps.

To generate samples according to σ_M^{sm}, we ran each random walk for 1000000 steps and collected samples every 100 moves. Each random walk produced therefore 10000 approximately independent samples. We ran the 4 random walks in parallel, each of them requiring a single processor. The computation time needed was $\sim$40 days on a Linux cluster based on AMD Opteron 64-bit CPUs. We then merged all ensembles produced by the different random walks into a single ensemble which we finally used to estimate marginals.

To generate samples according to $\sigma_M^{sm,gps}$ the sampling algorithm requires solving the forward modeling for the GPS data prediction. With this additional calculation, each random walk produced 300000 models in approximately the same computation time ($\sim$ 35 days). From each random walk we extracted 3000 approximately independent samples, which we then merged to estimate the corresponding marginals. Even with a smaller number of samples we observed that each single random walk was able to produce approximately the same marginal, indicating therefore an acceptable convergence.

In Fig 2.10 we present 1D marginals for peak slip-velocity at grid points, displaying only inner grid points because on the fault plane boundaries peak slip velocity is assumed to be zero (section 2.4.2). For each node we present the 1D prior marginal, the posterior obtained from σ_M^{sm} and the one from $\sigma_M^{sm,gps}$.

The most important feature to note is that the posteriors generally do not show a Gaussian shape but rather a skewed distribution. The only two posterior marginals with a Gaussian-like distribution corresponds to nodes number 16 and 17. For these two nodes the posteriors from $\sigma_M^{sm,gps}$ predict a peak slip velocity of 122 ± 57 and 140 ± 57 cm/s, respectively. The relative error for both these two nodes is about 47 and 41 per cent, respectively. These two posteriors confirm the presence of a near-surface high slip-velocity patch as imaged in the maximum likelihood models (Fig 2.5, Fig 2.6).

For all the remaining nodes posteriors show a distribution skewed towards the minimum allowed peak-slip velocity value (0 cm/s). Note that the skeweness depends on the node location. As a general trend we find that the skeweness, and therefore the posterior peak, become less clear from the top edge of the fault towards the bottom (see subplots along the columns). This is particularly evident for posteriors from strong motion data only. This implies that the resolution power of the data sets (measured at each node by the difference between posterior and prior pdfs) follows the same trend and decreases with increasing depth.

Comparing posterior marginals obtained from σ_M^{sm} and $\sigma_M^{sm,gps}$, we find that GPS data have a noticeable effect in constraining the peak slip-velocity distribution. In fact, GPS data are sensitive to the final slip distribution. In our modeling the final slip at each fault location is directly proportional to peak slip-velocity (assuming an isosceles triangle as source time function, final slip = (peak slip-velocity $\times$ rise time)/2). Looking at nodes 16 and 17, we see that GPS data confirm the presence of a high slip-velocity patch. However, for node 17, GPS data suggest an even higher value of peak slip-velocity with respect to the one inferred when using strong motion data only. In most of the remaining locations, GPS data have an effect in reducing the tail of the posteriors obtained from σ_M^{sm}. This is evident at nodes 21, 32, 43, for instance. It is also interesting to notice that the GPS data used in this study have the same effect at the bottom of the fault (see nodes number 46, 47, 48). This shows that, at least in this case, GPS data bring useful information on the rupture process also for the deeper part of the fault.

We show 1D marginals for rise time in Fig 2.11: the posterior marginals present a well defined peak only for the nodes located near the high slip-velocity patch (nodes 15, 16, 17, 18 and 27, 28, 29). For all remaining nodes posterior marginals present very little difference with respect to the prior uniform indicating therefore very poor resolution for rise time. At node 17, corresponding to the highest inferred peak slip-velocity value, the mean rise time is about 4.4 s. We also notice that the maximum estimated mean rise time (7.2 s) corresponds to node 28, which is associated with low peak slip-velocity values [see corresponding posterior in Fig 2.10]. We could expect to have little resolution on rise time for a node associated with low slip-velocity. However, we recall that rupture parameters are defined on a coarse grid on the fault surface and then derived on a finer grid (where the actual integration is carried out) through bilinear interpolation. Even if a node is associated with a low value of peak slip-velocity, its vicinity may not have low values if a neighbouring node is associated with an high value of peak slip-velocity. Node 17, where the highest value of peak slip-velocity is inferred, is a neighbouring node of node 28. This means that between these two nodes, significant peak slip-velocity may be present. In that case, the long rise time corresponding to node 28 is needed to describe the slip process in its neighbourhood. When comparing posteriors from σ_M^{sm} and $\sigma_M^{sm,gps}$ we notice the greatest differences only at nodes 17 and 18. For these nodes GPS data increase the probability associated with larger values of rise time.

In Fig 2.12 we show 1D marginals for rupture time. In this case we consider also nodes located at the edges of the fault. Marginals from σ_M^{sm} and $\sigma_M^{sm,gps}$ are very similar, since GPS data do not contribute information about rupture timing. Again, we find that posteriors present a well defined peak with respect to the prior marginals only in the upper-most part of the fault (especially at nodes 4, 5, 6 and 15, 16, 17). Nodes 16 and 17 correspond to the nodes where the shallow high slip-velocity patch is located. Assuming mean values as estimates of the actual rupture times, the rupture front triggers the high slip-velocity patch located below the top edge of the fault (nodes 17) approximately 3.1 s after the rupture initiated. The average rupture velocity from the hypocentre in the updip direction is therefore 1.6 km/s, corresponding to 44 percent of the average shear velocity in the involved depth range. For some nodes located on the boundary of the fault (4, 5 and 6 especially) the posterior pdfs show a clear peak, although for these nodes the peak slip-velocity is assumed to be zero. The fact that data are sensitive to these parameters is an effect of the bilinear interpolation scheme. Even if these parameters correspond to nodes where the peak slip-velocity is assumed to be zero, the rupture time defined on these nodes determines the rupture time in the neighbourhood points. Hence, if these neighbourhood points are associated with well resolved slip, the rupture time in the neighbourhood nodes will also be well resolved.

Comparing 1D marginals for the rake angle (Fig 2.13) with marginals for peak slip-velocity (Fig 2.10), rise time (Fig 2.11) and rupture time (Fig 2.12) we find that the rake angle is the least resolved parameter in the considered model space. Differences between priors and posteriors are generally less accentuated than for the other parameters. We also observe that GPS data have a noticeable effect in constraining the rake angle at some locations. This is evident at nodes 16, 17, 27, 28. In these locations posterior marginals suggest that the high slip-velocity patch is associated with a positive rake angle, which implies a downdip movement in our modeling.

Fig 2.14 shows posterior marginals for final slip (derived from peak slip-velocity and rise time values). Note that prior marginals are not uniform because they represent prior information on a combination of the original model parameters. Again we find that posteriors show mostly a skewed distribution. Only posteriors at nodes 16 and 17 show a Gaussian-like shape. For these two nodes posteriors predict a final slip of 250 ± 120 cm and 311 ± 140 cm, respectively. The relative error is $\sim$48

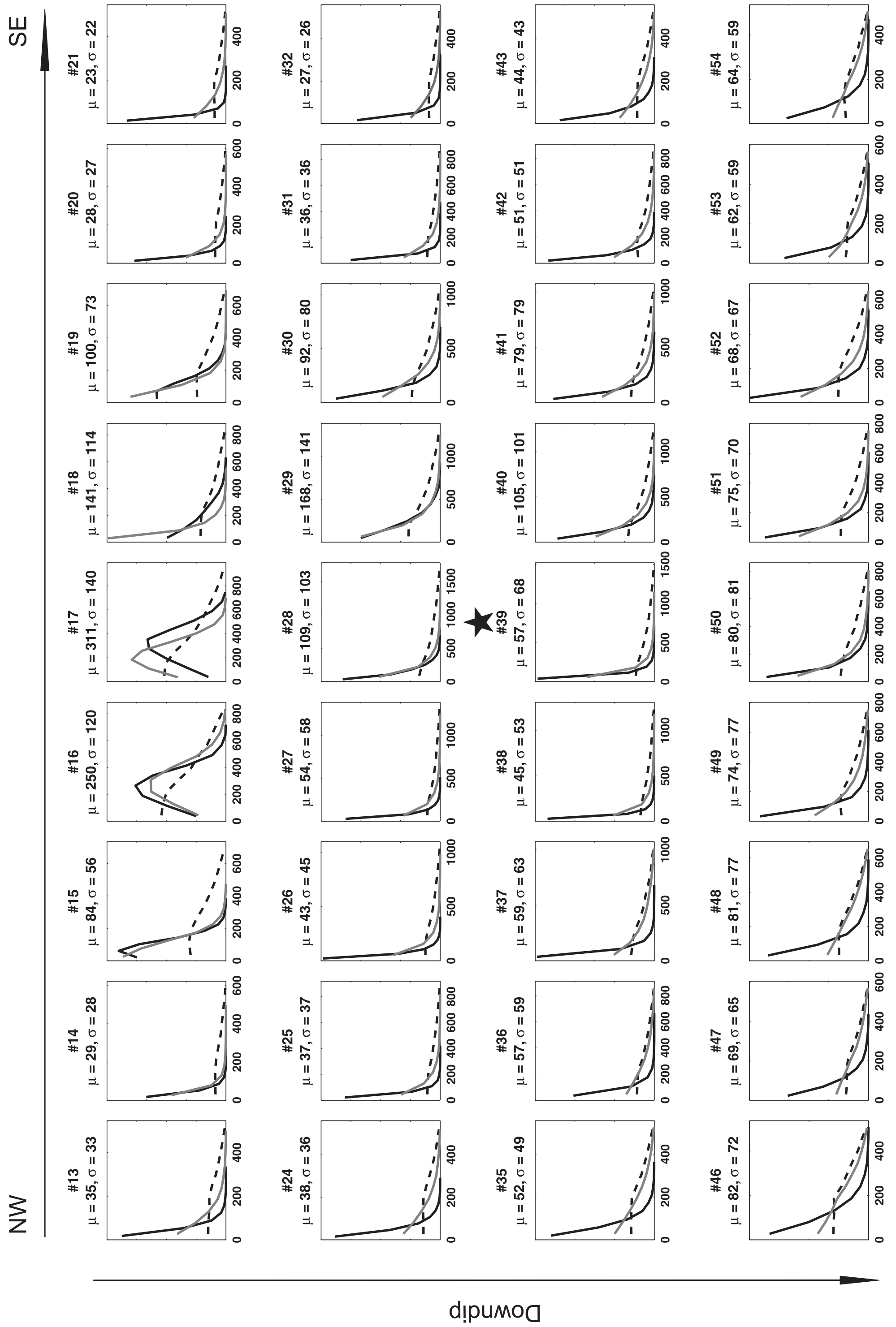

Figure 2.14: 1D marginals for final slip (cm). Same notation as in Fig 2.10

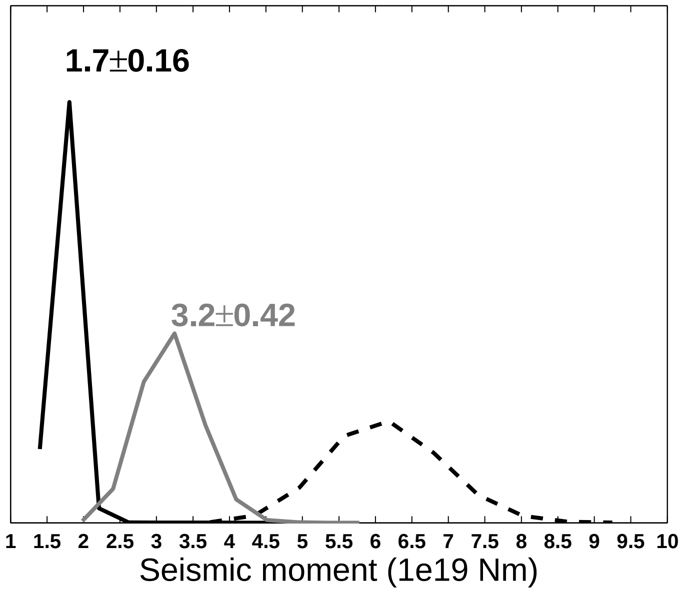

Figure 2.15: 1D marginals for seismic moment as obtained from the prior pdf (dashed), σ_M^{sm} (gray) and $\sigma_M^{sm,gps}$ (black).

and 45 per cent, respectively. We also infer a low slip region NW of the hypocentre (nodes from 24 to 27 and 35 to 38). In these locations 1D marginals present a distribution skewed towards the minimum allowed slip (0 cm) with standard deviations $\lesssim 50$ cm. SE of the hypocentre 1D marginals present instead larger standard deviations: ~ 100 cm at nodes 28 and 40 and ~ 140 cm at node 29 indicating therefore a wider range of likely values. This feature may suggest an elongation of the slip distribution towards SE. The effect of GPS data in constraining the peak slip-velocity is reflected in the marginals for the final slip. GPS data have a noticeable effect in reducing the tail of the marginals (see nodes 21, 32, 43, for instance). They help also in constraining the shallow slip (see node 16 and 17).

These changes have a strong effect when computing the posterior marginal for seismic moment (Fig 2.15). GPS data reduce the probability associated with high values of slip and produce a shift of the peak of the posterior towards lower values of seismic moment than obtained from σ_M^{sm}. From the posterior marginal from $\sigma_M^{sm,gps}$ we infer a value of seimic moment equal to $1.7 \pm 0.16 \times 10^{19}$ Nm. The corresponding relative error is about 10 percent.

In Fig 2.16 we present posterior 1D marginals (derived from $\sigma_M^{sm,gps}$ only) for seismic moment and moment rate as they evolve in time. In other words we compute moment and moment rate time histories for each sample of $\sigma_M^{sm,gps}$ and then compute at each time step the corresponding 1D marginal. In this way we obtain a 'probabilistic' image of the moment and moment rate functions where at each time step we have not a single value but rather a distribution of values. From the seismic moment time history we see that most of the seismic moment starts to be

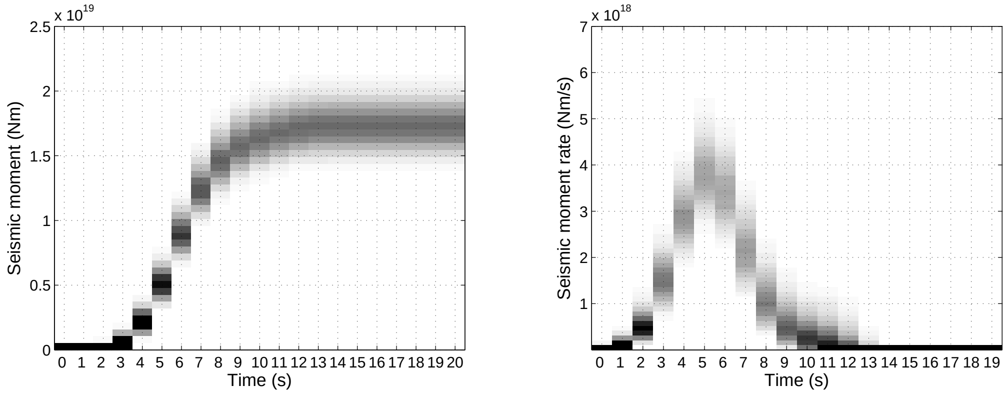

(a) (b)

Figure 2.16: 1D marginals for moment (a) and moment rate (b) (derived from $\sigma_M^{sm,gps}$ only) as they evolve in time.

released only after about 3 seconds from the origin time. This is consistent with the fact that the shallow slip patch is triggered, on average, 3 s after the earthquake initiated. The moment rate function assumes its peak value at about 5 s. Again considering node 17, we infer a value of rise time of 4.4 s [average value deduced from posterior marginal for rise time, see Fig 2.11 (b)]. In other words, at node 17, the slip-velocity reaches its peak value about 2 s after the rupture time, that is at about 5 s. We therefore see a correlation between the peak of the moment rate function and the peak of the source time function at node 17 which is associated with the highest inferred slip.

2.5.3 The 2D marginals

1D marginals represent all information we have on a single parameter. However, they do not contain any information about possible correlations with other parameters, which constitutes an integral part in any uncertainty analysis. If a pair of parameters is correlated, this implies that we cannot measure them independently. Correlations between pairs of different parameters can be analyzed computing 2D marginals.

Due to the large number of parameters (204 in this study) we did not explore all possible correlations. We focused our attention on the rupture parameters describing the shallow high slip patch, at nodes 16 and 17. We derived 2D marginals from $\sigma_M^{sm,gps}$ only because it considers all the data. We first computed 2D marginals between rupture parameters (mainly peak slip-velocity, rupture time and rise time) defined on the same node [Fig 2.17, Fig 2.18]. We do not identify any significant correlation between these parameters. In Fig 2.19 we instead present 2D marginals between rupture parameters defined on different nodes. Here, we identify a strong anti-correlation between peak slip-velocity values. In other words, if the peak slip-

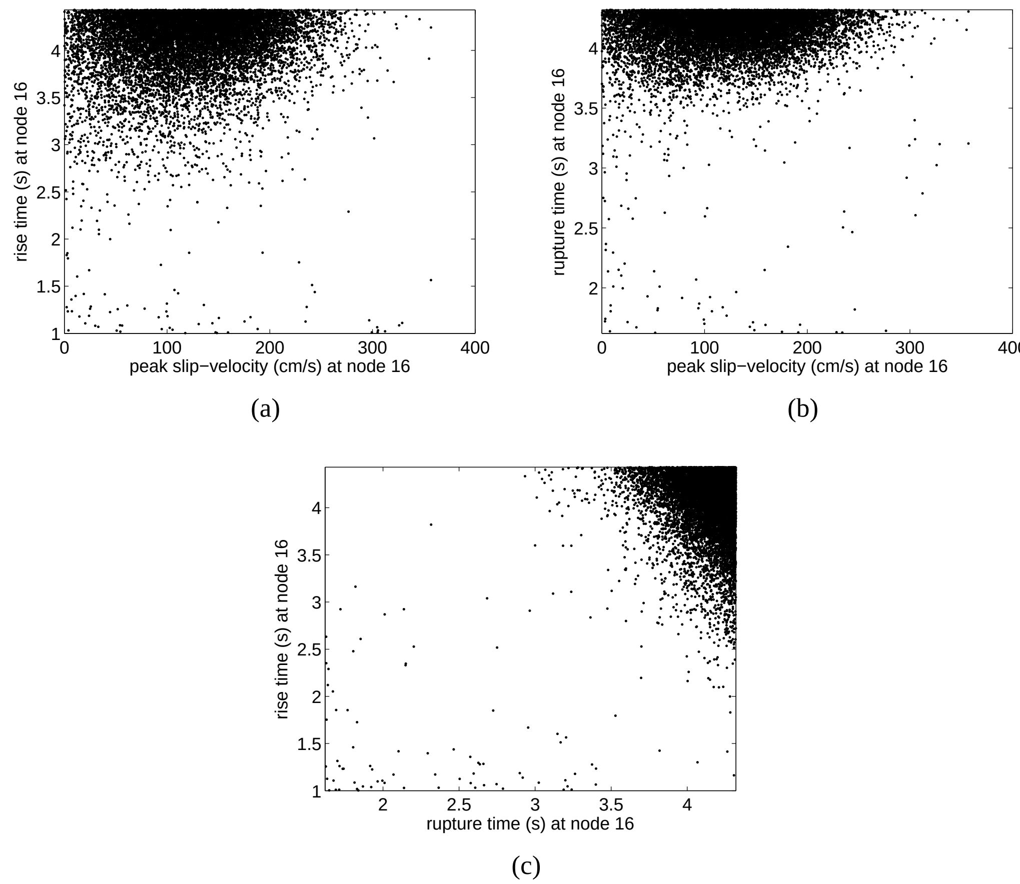

Figure 2.17: 2D marginals between peak slip velocity, rise time and rupture time values at node 16.

velocity at node 16 increases, the peak slip-velocity at node 17 will decrease, and vice versa.

2.6 Discussion

From the analysis of the 1D marginals computed from $\sigma_M^{sm,gps}$ we identify the following main features in the rupture process of the 2000 Tottori earthquake:

1. between the hypocentre and the top edge of the fault, corresponding to a depth of 4.5 km (nodes 16, 17), we find a high slip-velocity patch. Posterior marginals show a Gaussian-like shape from which we deduce values of peak slip-velocity of 122 ± 57 cm/s and 140 ± 57 cm/s.

2. in correspondence to the high slip-velocity patch the posterior marginals for rise time show a skewed distribution with the maximum attained at the maximum allowed rise time. The mean values for rise time at nodes 16 and 17 are 4.1 s and 4.4 s, respectively.

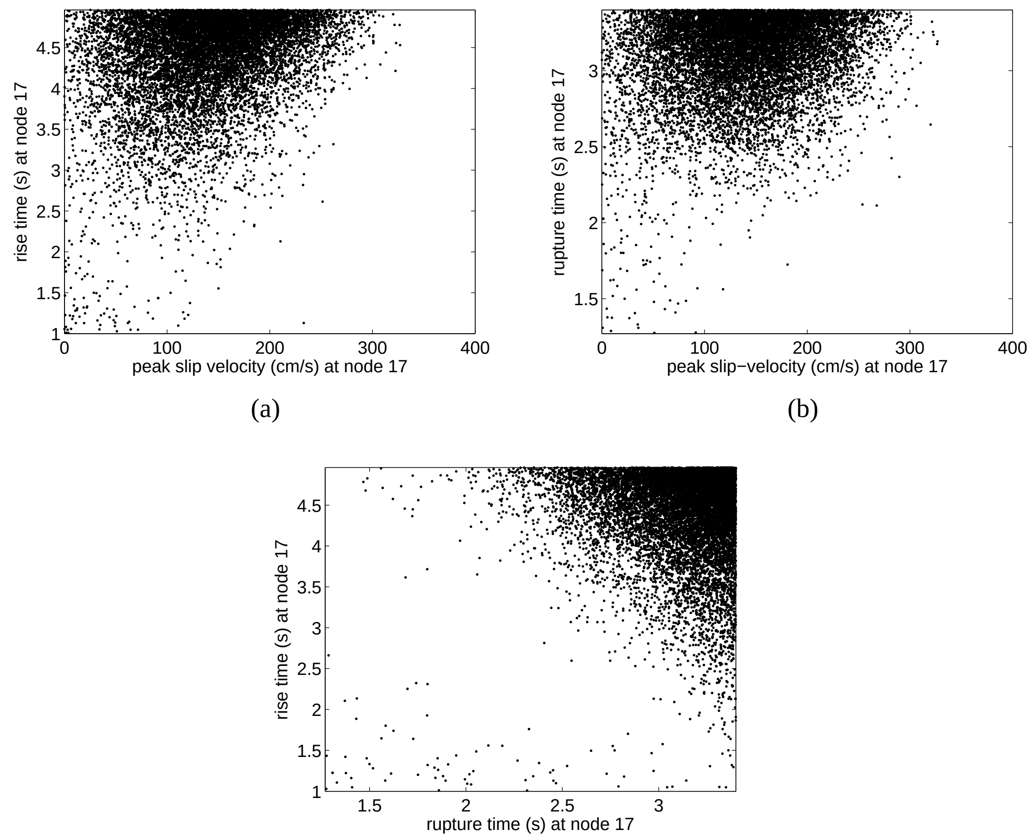

(a) (b) (c)

Figure 2.18: 2D marginals between peak slip velocity, rise time and rupture time values at node 17.

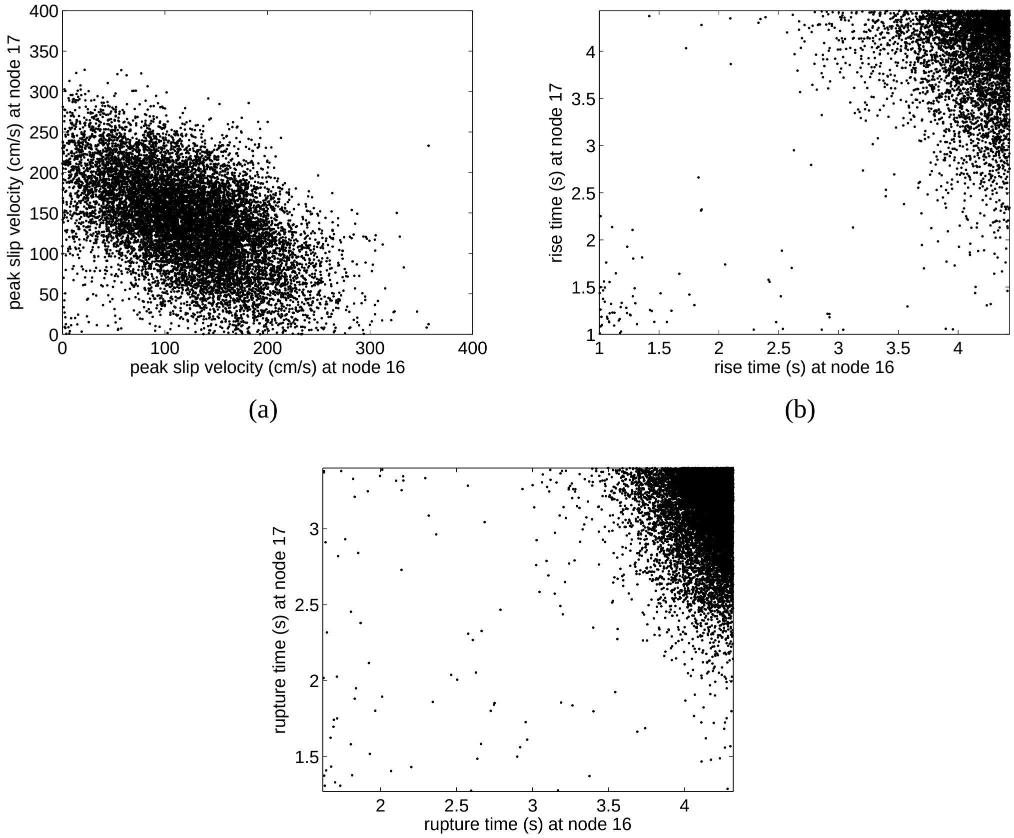

(c)

Figure 2.19: 2D marginals between peak slip velocity, rise time and rupture time values at node 16 and 17.

3. combining values of peak slip-velocity and rise time we infer for the shallow slip patch final displacements of 250 ± 120 cm and 311 ± 140 cm on nodes 16 and 17, respectively.

4. 1D marginals for rupture time indicate that the shallow slip patch is triggered about 3.1 s (mean value of posterior at node 17) after the rupture initiated at the hypocentre. We can therefore estimate an average rupture velocity in the updip direction of about 1.6 km/s.

5. the rake angle is generally poorly resolved in the model space considered. Only on the shallow slip patch (nodes 16, 17) posterior marginals suggest that a positive angle (down-dip component) is more likely then a negative one.

The presence of a high slip patch near the top edge of the fault has also been recognized in previous studies (Semmane et al. [2005], Festa & Zollo [2006], Piatanesi et al. [2007]). Their models indicate a maximum value of slip of about 4 m, roughly in agreement with our estimates (311 ± 140 cm). We do not identify any significant slip at the bottom of the fault. For the deepest nodes (from node 46 to 54) posterior 1D marginals of slip from $\sigma_M^{sm,gps}$ exhibit a skewed distribution with maximum attained at the minimum allowed slip (0 cm) (see Fig 2.14). Assuming that standard deviations represent the range of most likely values, we infer for the deepest nodes values of slip between 0 and ∼80 cm. Our inferences for the final slip distribution are therefore more consistent with the preferred model of Semmane et al. [2005], which does not show significant slip at the bottom, rather than with the models proposed by Festa & Zollo [2006] and Piatanesi et al. [2007], which suggest the presence of significant deep slip (up to 2.5 m).

Regarding the rupture timing we infer a value of about 1.6 km/s for the rupture velocity in the updip direction. Festa & Zollo [2006] and Piatanesi et al. [2007] inferred values equal to 2.1 and 2.2 km/s, respectively. These higher values may be due to the deeper hypocentre assumed in these studies (13.5 km Festa & Zollo [2006] and 12.5 km Piatanesi et al. [2007]) with respect to the one we adopted (9.6 km).

Another difference from previous studies concerns the rise time pattern. Our results show that rise time values are well resolved only in the vicinity of the shallow high slip patch. At these locations (nodes 16, 17 for instance) the rise time values equal $\sim$ 4 s. Semmane et al. [2005]'s preferred model shows at the same locations lower values between 0.5 and 1.5 s. Piatanesi et al. [2007]'s average model shows instead more comparable values between 2.5 s and 3 s.

As recognized in all studies (including this work), a peculiar feature of the Tottori earthquake is the presence of considerable slip at shallow depth (311 ± 140 cm at 4.5 km depth) without any evident surface rupture. Identifying the reasons why the slip did not reach the surface is beyond the scope of this paper and requires dynamic modeling of the earthquake rupture process. Qualitatively, we can imagine that possible reasons impeding slip propagation to the surface can be a velocity-strengthening behaviour of the shallow layers or low pre-stress in the upper-most part of the fault, or a combination of these two effects.

Also, the Tottori earthquake is not the only event showing shallow slip with no surface breaks. An earthquake showing similar behaviour is the 2003 $M_W = 6.5$, Bam (Iran) earthquake. From the inversion of radar data Fialko et al. [2005] showed how the Bam earthquake is characterized by right-lateral displacements having a maximum amplitude of about 2 m at a depth of 3 to 7 km. However both radar data and field investigations confirm lack of surface rupture associated with the faulting event.

Finally, we stress that all the results we show in this study depend and are limited by the chosen model space. For instance, in our study we find that for some parameters (e.g. concerning rise time and rupture time), the posterior marginals are skewed towards the maximum allowed value, suggesting that the solution, for these parameters, is located beyond the upper bound of the considered range of values. We acknowledge therefore that a natural extension of this work would be considering a larger model space (e.g. by removing constraints on rise time), and checking if the inference results remain stable or if new solutions are found.

2.7 Conclusions

In this study we investigate the rupture process of the 2000 Western Tottori earthquake through fitting of strong motion and GPS data. Our inversion methodology is based on a Bayesian approach. We state our inferences in terms of marginal pdfs derived from two distinct posterior pdfs: one that considers only strong motion data and one that considers both strong motion and GPS data.

With both posteriors, we identify as a stable feature of the earthquake rupture process the presence of a high slip patch between the hypocentre and the top edge of the fault. This feature is common with previous studies. The analysis of the 1D marginals for rupture time, rise time and rake angle indicates that these parameters are well resolved only where this shallow slip patch is located, meaning that the signal emitted by this patch determines most of the wavefield that we fitted.

When using both strong motion and GPS data, we do not identify any significant slip (> 1 m) at the bottom of the fault. For this aspect, our inference results disagree with some previous studies (Festa & Zollo [2006] and Piatanesi et al. [2007]).

We compare inferences obtained considering strong motion data only with ones derived considering both strong motion and GPS data. In our study we notice that the main effect of GPS data is in reducing the precence of spurious slip on the fault which in turn has a strong influence on the estimate of the final seismic moment.

A clear point in our analysis is that resolution on kinematic rupture parameters cannot be explained generally using the Gaussian uncertainty hypothesis. In our study most of the 1D posterior marginals do not show a Gaussian distribution. Understanding the actual resolution requires taking into account the non-linearity of the problem and therefore dealing with non-Gaussian distributions.

Acknowledgments

We thank K-net and KiK-net for providing strong motion data. This study was founded through ETH-grant TH-16/05-1. Some figures were made using Generic Mapping Tools free software.

Chapter 3

Estimation of dynamic parameters from an uncertain kinematic rupture model: Application to the 2000 Western Tottori (Japan) earthquake

Abstract

Estimating dynamic source parameters from past earthquakes is important to investigate the weakening process of real faults, and to derive realistic dynamic rupture models for ground motion simulations of future earthquakes.
Dynamic parameters can be estimated from the on-fault stress generated by a kinematic slip model. However, multiple kinematic rupture models may satisfy the observations for a given earthquake and therefore uncertainties in kinematic parameters propagate into the estimation of dynamic parameters.
In this study we investigate how the estimation of dynamic parameters is affected by uncertainties in the kinematic source model. For this purpose we consider the 2000 Western Tottori earthquake for which we previously obtained an ensemble of 3000 kinematic models through Bayesian inference (i.e. samples of the posterior probability density function) which are consistent with the observed strong motion and GPS data. For each model of this ensemble we compute the spatio-temporal evolution of stress over the fault. We therefore obtain an ensemble of dynamic rupture models, which all explain the observations, and from which we can statistically explore the resolution of dynamic parameters.
We statistically analyse resolution of static stress drop. We find that on the same locations where stable high slip is inferred, frequency distributions of static stress drop values have an approximately Gaussian shape with positive mean values indicating that on average these locations undergo a weakening process. However, we find standard deviation values of the same order of magnitude of the estimated mean values indicating therefore large uncertainties in the actual intensity of static stress drop. We show how these large uncertainties are due to a correlation between stress drop values at neighboring points of the source model which is inherited from a correlation between slip values. This shows how a correlation between kinematic parameters limits resolution of dynamic parameters. Despite the difficulty in constraining the rupture process locally on the fault, we find that a global quantity like radiated energy can be well inferred instead. The 95 percent confidence level indicates that the final radiated energy lies in between 2.1×10^{14} J and 4.0×10^{14} J, with a mean value equal to 2.9×10^{14} J. This is consistent with previous independent studies which estimate radiated energy to be about 3.0×10^{14} J.

3.1 Introduction

A major goal for earthquake seismology is to understand the physics governing the fault rupture process. This is a complex phenomenon controlled by various factors: the fault geometry, the stress acting on the fault, the material properties surrounding the fault and the constitutive law, that is the physical law relating stress to slip, slip velocity and other factors, like pressure, temperature and chemical effects, for instance.

When using seismic or geodetic data, the earthquake source is usually approximated as a shear crack propagating dynamically over a zero-thickness fault surface

[Scholz, 2002]. Within this approximation, the earthquake rupture process can be described in terms of kinematic and dynamic parameters. Kinematic parameters are those defining the slip process at each location on the fault: maximum slip (or slip-velocity), rupture time (time at which the slip process starts), rise time (duration of slip) and rake angle (direction of slip). Kinematic parameters are directly linked to the observed ground motion through the representation theorem [Aki & Richards, 2002]. By posing the representation theorem as a linear inverse problem, kinematic parameter estimates can be obtained through linear inversion of seismic data (e.g. Olson & Apsel [1982], Hartzell & Heaton [1983]). Over the years, estimation of kinematic parameters improved with considering additional data sets (GPS, InSar) (e.g. Wald et al. [1996], Delouis et al. [2002], Salichon et al. [2003]) and with abandoning the linear approximation (e.g. Liu & Archuleta [2004]).

Together with this improvements, it became clear that the same earthquake can be explained by different kinematic rupture models (Cohee & Beroza [1994], Beresnev [2003], Ide et al. [2005], Custodio et al. [2005], Hartzell et al. [2007]). This is also evident in the on line database of earthquake rupture models (http://www.seismo-.ethz.ch/srcmod). Some of the observed discrepancies are due to different model parameterizations, inversion schemes, and data-sets, for instance. However, independently of the particular approach, intrinsic reasons render imaging the earthquake source a problem with multiple solutions: uncertainties in data and in forward modeling (which allow multiple models to be considered acceptable), and lack of resolution (due to the always limited data coverage). To describe this multiplicity of solutions, several innovative methods have been proposed recently (Emolo & Zollo [2005], Piatanesi et al. [2007], Monelli & Mai [2008], Monelli et al. [2009]). These studies recognise that the kinematic image of the earthquake rupture process cannot be expressed in terms of a single best-fitting model but rather in terms of a set of models which show certain statistical properties.

Dynamic parameters describe instead the stress evolution at each location on the fault. The most common used dynamic parameter is the final stress drop (difference between initial and final stress), which is often referred to as "static" stress drop. For those locations on the fault undergoing a weakening process, the stress evolution is characterised also in terms of dynamic stress drop (difference between initial and minimum stress) and strength excess (difference between peak stress and initial stress). Some attempts to infer dynamic parameters directly through fitting seismic data have been made (Peyrat & Olsen [2004], Corish et al. [2007]). However, the commonly used approach requires first estimating the kinematic parameters and then solving the elastodynamics equation for the spatio-temporal evolution of on-fault stress using the kinematic parameters as a boundary condition (e.g. Ide & Takeo [1997], Bouchon [1997], Dalguer et al. [2002], Tinti et al. [2005b]). With this approach dynamic parameters can be determined from the kinematic source characterization.

As mentioned above multiple kinematic rupture models for a given earthquake may be consistent with the corresponding seismic and geodetic observations. To our knowledge no study has been published that investigates how uncertainties in kinematic parameters propagate into the estimation of dynamic parameters. The usual procedure is to consider only the best-fitting model to derive a dynamic image of the rupture process.

The major goal of this paper is to investigate how uncertainties in a kinematic rupture model map into the corresponding dynamic rupture parameters, and to investigate how well constrained is the spatio-temporal evolution of stress over the fault. Estimating resolution of dynamic parameters is an important aspect in understanding how reliably we can image the constitutive law from seismic data and related quantities (e.g. fracture energy).

In this study we consider a real event, the 2000 Western Tottori earthquake. We use a Monte Carlo approach to propagate uncertainties from kinematic into dynamic parameters. We make use of the ensamble of models derived by Monelli et al. [2009] which are consistent with the observed strong motion and GPS data. To reduce the computational demand, we select a sub-ensemble of models which show approximately the same statistical properties of the original ensemble. For each model of this sub-ensemble we compute the spatio-temporal evolution of stress over the fault. We therefore obtain an ensemble of dynamic rupture models from which we can statistically investigate resolution of dynamic parameters.

3.2 Computation of dynamic parameters

For a given kinematic model we compute the corresponding spatio-temporal evolution of on-fault stress using a velocity-stress staggered-grid finite difference scheme, based on the Staggered-Grid Split-Node (SGSN) method to simulate the fault rupture [Dalguer & Day, 2007]. We use a grid spacing of 250 m and a time step of 0.01 s. Monelli et al. [2009] show that after approximately 10 s the rupture is almost complete. To ensure that the on-fault stress field reaches a stationary condition we simulate a time window of 20 s. We consider the same velocity model used by Monelli et al. [2009].

Monelli et al. [2009] defined kinematic parameters on a 4 by 4 km grid over the fault surface (Figure 3.1). To avoid stress singularities, we use a bicubic interpolation scheme to derive kinematic parameters values on the finite difference grid. In some cases, we find that the bicubic interpolation scheme produces negative values when interpolating peak slip-velocity values. For those points having negative values we force the peak slip-velocity to be zero. We assume the absolute initial traction to be equal to an arbitrary value of 70 MPa and collinear with the slip vector.

3.3 An uncertain slip model for the 2000 Western Tottori earthquake

Using a Bayesian approach, Monelli et al. [2009] inferred kinematic rupture parameters for the 2000 Western Tottori (Japan) earthquake through fitting of strong

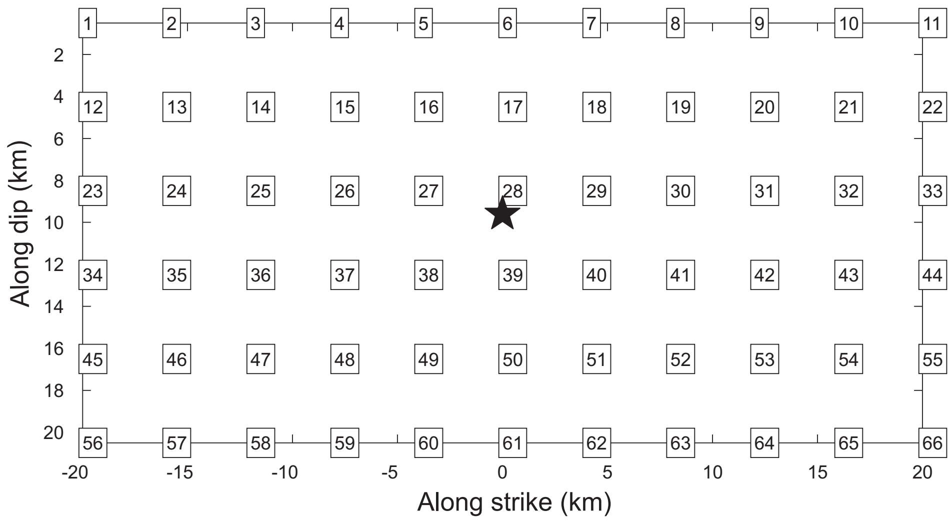

Figure 3.1: Fault discretization used by Monelli et al. [2009]. Numbered labels indicate node locations. The grid spacing is 4 km. The black star represents the hypocentre location according to Fukuyama et al. [2003].

motion and GPS data. The rupture parameters investigated are peak slip velocity, rise time, rupture time and rake angle. They are defined on a regular grid of nodes on the fault surface and their values at inner points are derived through bilinear interpolation. The assumed source time function is an isosceles triangle.

Monelli et al. [2009] expressed inferences on rupture parameters in terms of marginal probability density functions (PDFs) derived from an ensemble of models which are samples of the posterior PDF. This ensemble has been generated simulating 4 random walks each of them producing 3000 samples. In Figures 3.2, 3.3, 3.4 and 3.5 we present the corresponding 1D marginals computed from the ensembles of models.

Examining the 1D marginals for peak slip-velocity we note that the Tottori earthquake is characterised mainly by a single high slip-velocity patch (nodes 16 and 17) located between the hypocentre and the top edge of the fault. In all other locations we cannot identify other stable patches of high slip-velocity. For a more detailed analysis and interpretation of the 1D marginals we refer to the work of Monelli et al. [2009]. For this study, the important point to notice is that each random walk produces approximately the same results. We can therefore consider the ensemble of 3000 models produced by a single random walk to be sufficient to represent uncertainties on kinematic rupture parameters.

The selected ensemble of models truly represents the solution of the inverse problem in the sense that all models produce very similar data predictions and should be all considered as plausible models. In Figures 3.6 and 3.7 we show the observed strong ground motion waveforms and we compare them with the 95 percent confidence levels of the predicted strong ground motion waveforms. In other words,

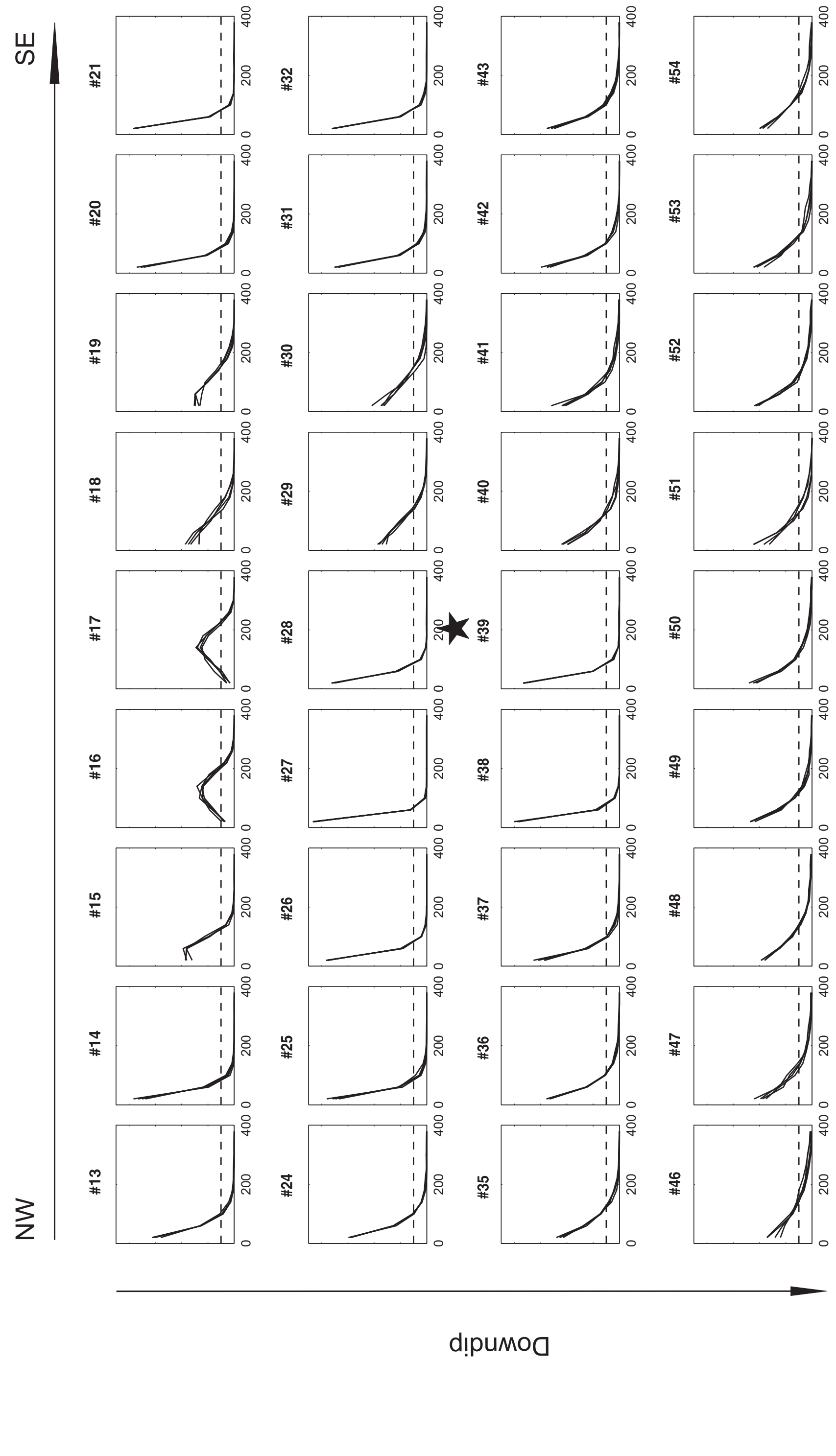

Figure 3.2: 1D posterior marginals for peak slip-velocity (cm/s) generated by each random walk. Each subplot corresponds to a node position. Dashed lines represent priors, solid lines posterior marginals. For each subplot we indicate the node number. The black star represents the hypocentre location.

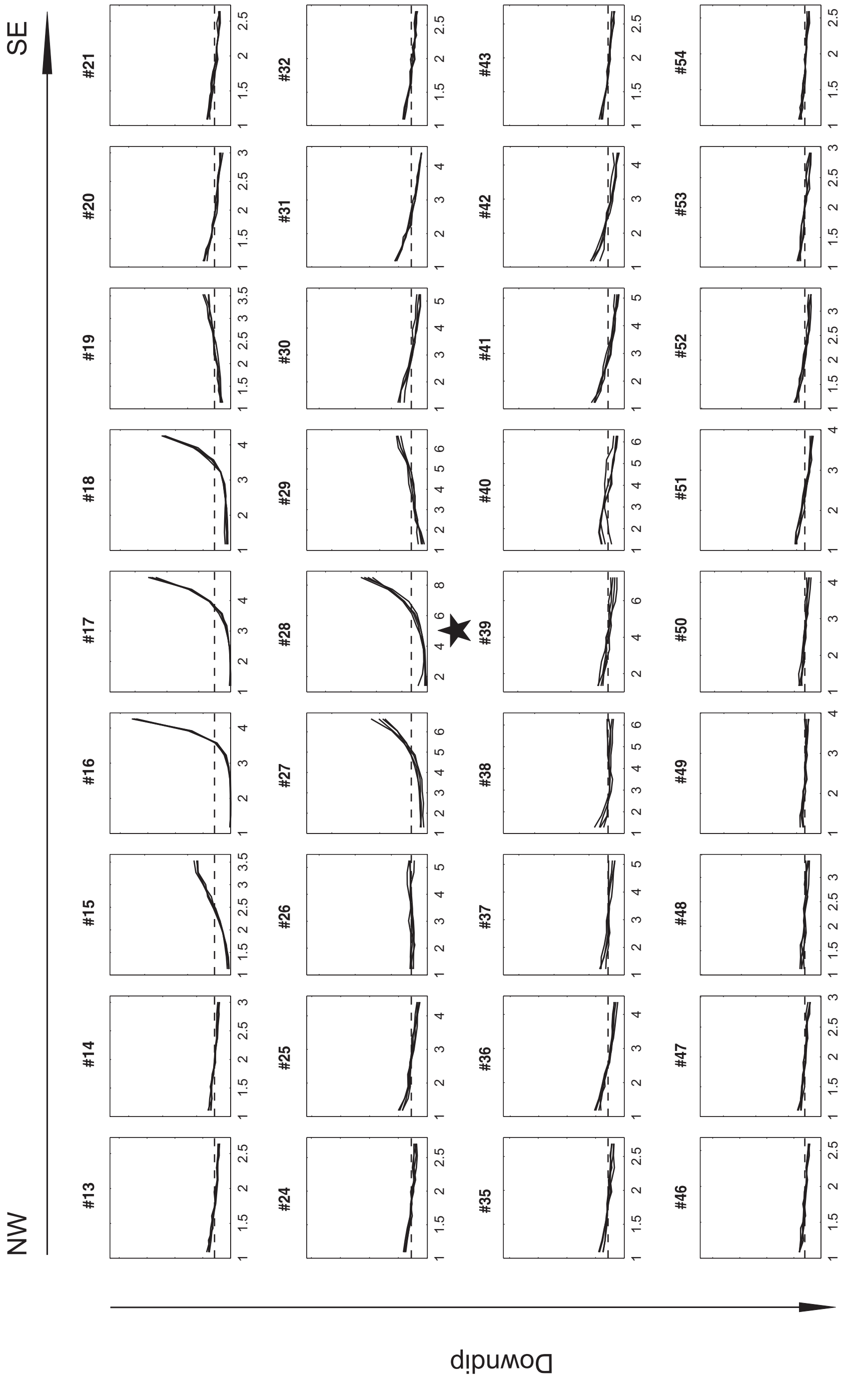

Figure 3.3: 1D marginals for rise time (s). Same notation as in Fig 3.2

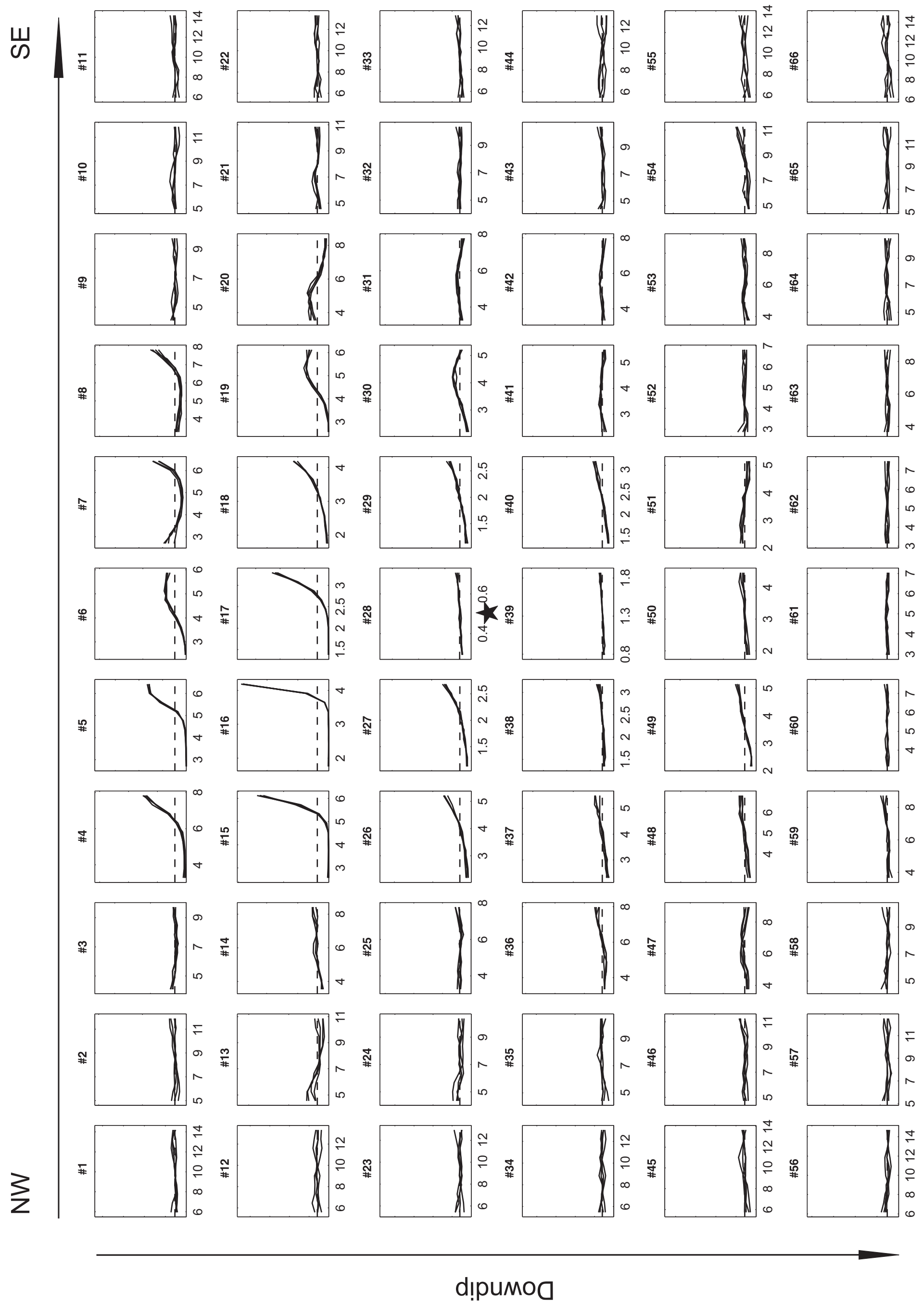

Figure 3.4: 1D marginals for rupture time (s). Same notation as in Fig 3.2

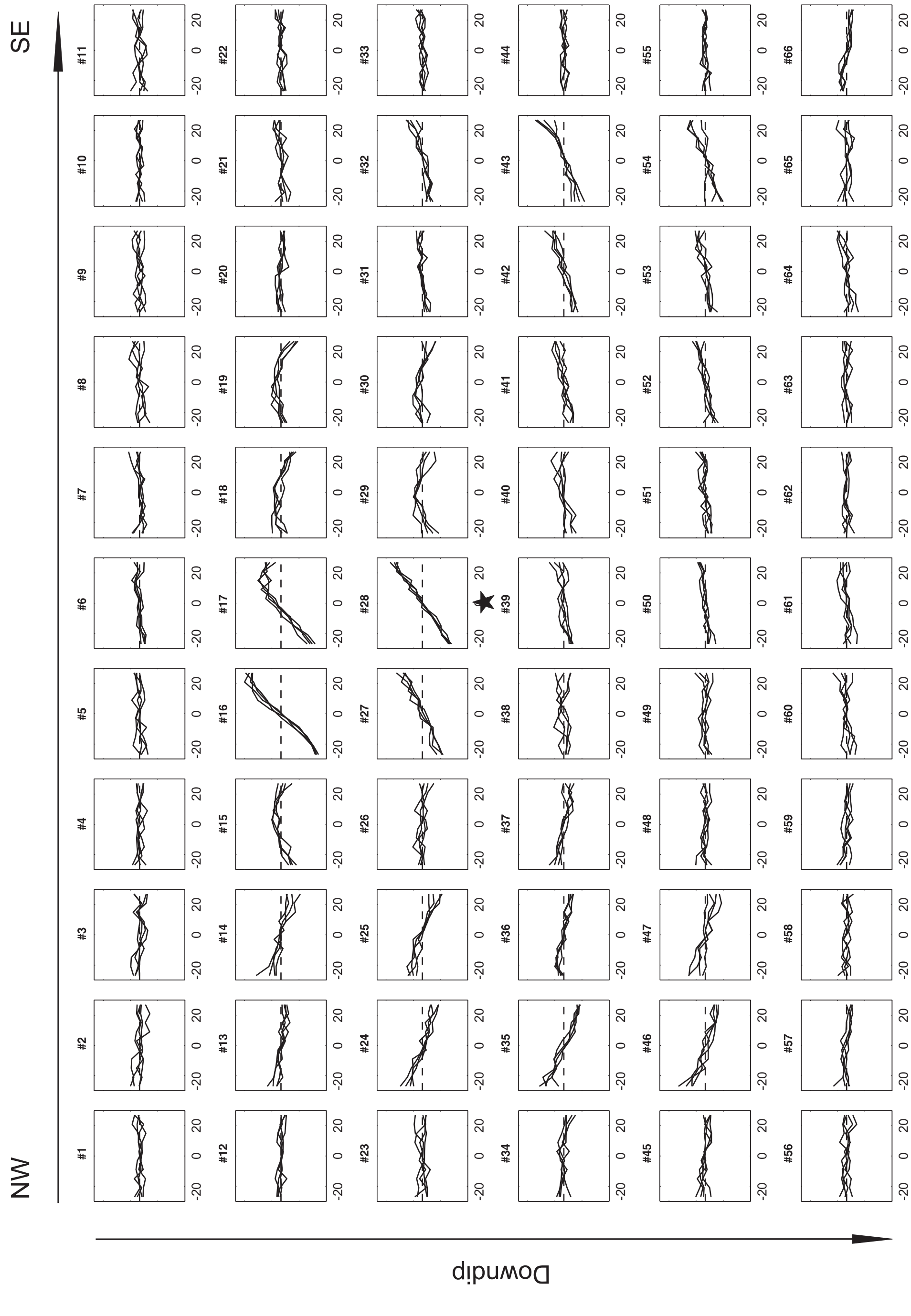

Figure 3.5: 1D marginals for rake angle (degree). Same notation as in Fig 3.2

for each component we compute at each time step the 0.025 and 0.975 quantiles of the distribution of predicted ground motion values. In this way, we statistically compare the observations with the predictions of all the models constituting the ensemble. We perform a similar analysis to compare observed with predicted surface static displacement (Figure 3.8).

Looking at strong motion data, we see that all the ensemble of models produce very similar waveforms which capture the essential features of the observed wavefield. Also for GPS data, we see that the 95 percent confidence levels of data predictions overlap with the 95 percent confidence levels of data observations, at all station. We find therefore that all models in the considered ensemble produce similar data. We hence propose that robust conclusions about the rupture process of the 2000 Tottori earthquake should be drawn analysing the entire ensemble of kinematic models and not only the best-fitting one. In other words, given the uncertainties in the data and the simplifications in the modeling, no strong reasons exist to consider the best-fitting model as the only model able to explain the data. Hence, only those features which appear to be statistically significant in all the ensemble of models should be considered as well resolved.

Before statistically investigating the resolution of dynamic parameters we want to show explicitly how uncertainties in kinematic models affect the estimation of dynamic parameters. In Figure 3.9 and 3.10 we show two kinematic rupture models (both samples of the posterior PDF defined by Monelli et al. [2009]) producing very similar ground motions. These two models show the essential features of the Tottori earthquake: near the hypocentre, in the NW direction, low slip/slip-velocity values are inferred. A high slip/slip-velocity patch is located instead between the hypocentre and the top edge of the fault. Together with these large scale common features the two models present also several differences (e.g. high slip-velocity patches at the bottom of the fault in model 1, which are not present in model 2; significant slip right of the hypocentre in model 1, which is shifted to the bottom in model 2).

The two kinematic models are significantly different in terms of the on-fault stress evolution. In Figure 3.11 we show the temporal evolution of shear traction produced by models 1 and 2. We show only the inner nodes, because on the fault edges the slip is assumed to be zero and stresses are therefore forced to increase in both models. We see how the differences in the kinematic rupture models produce several differences in the spatio-temporal evolution of on-fault stress. At nodes 16 and 17, where a stable high slip patch is inferred [Monelli et al., 2009], model 1 predict a decrease of shear stress of about 50 and 10 MPa, respectively, whereas model 2 predict values of 10 and 30 MPa, respectively. It also happens that at the same nodes (e.g. nodes 29, 36, 37, 40) the two models predict static stress drops of opposite sign. These differences are reflected also in the spatial distribution of static stress drop (Figure 3.12 (a) and (b)). As a common feature, both models show significant positive stress drop above the the hypocentre. However, model 2 shows a positive stress drop patch just right of the hypocentre, which is not present in model 1. Moreover, model 1 presents a deep positive stress drop patch which is absent in

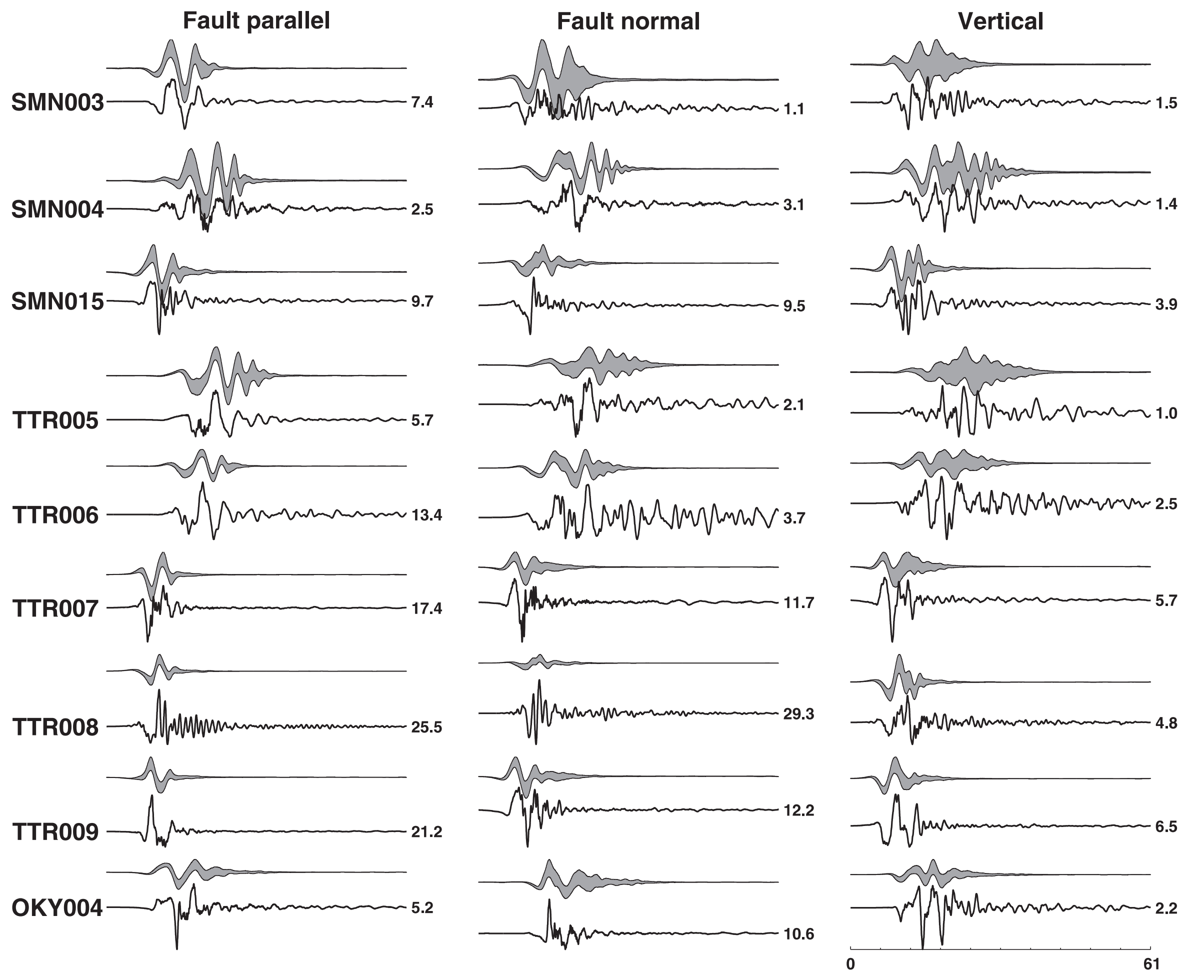

Figure 3.6: Observed strong ground motion waveforms (black) compared with 95 percent confidence levels (gray) of predicted ground motion. For the station location see Monelli et al. [2009].

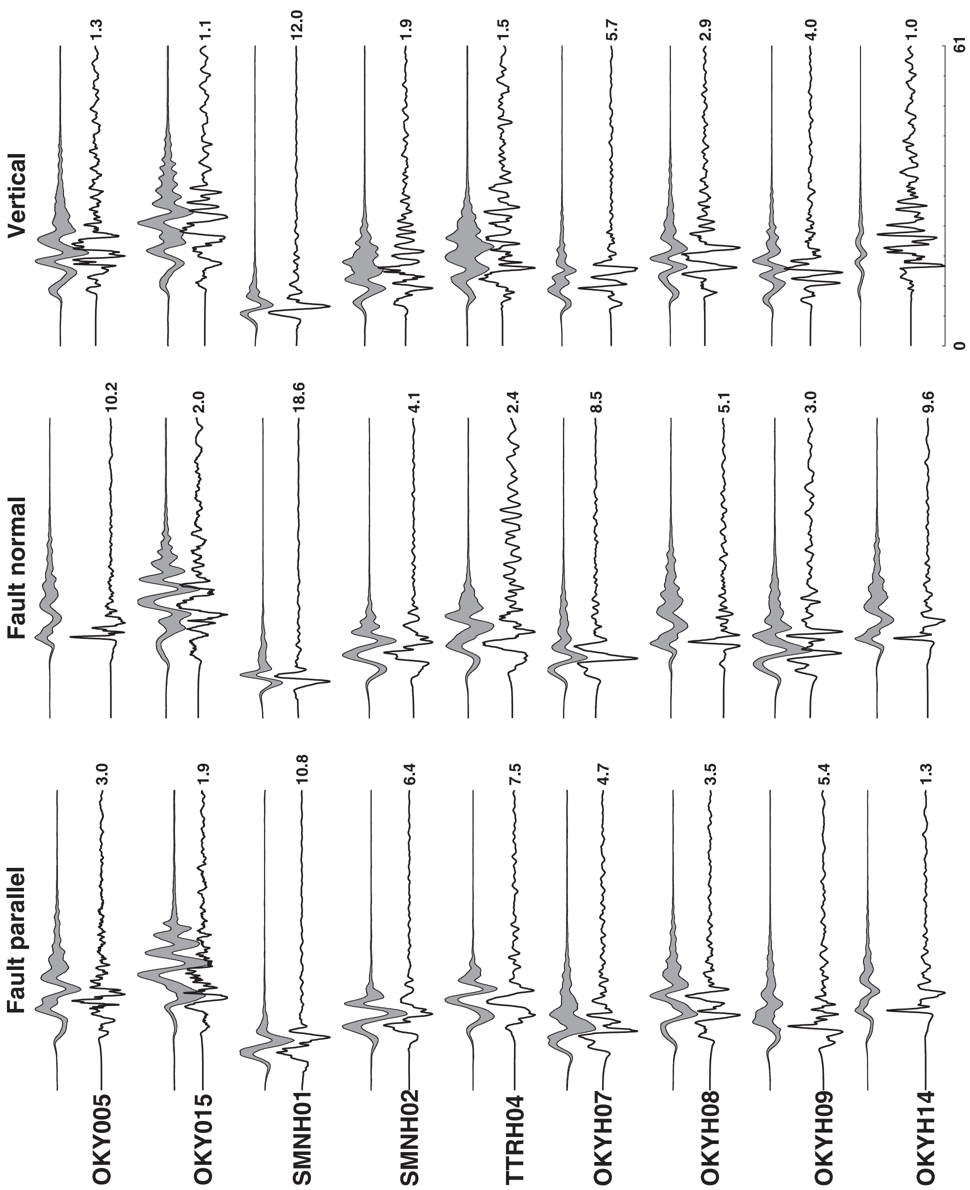

Figure 3.7: Same as Figure 3.6.

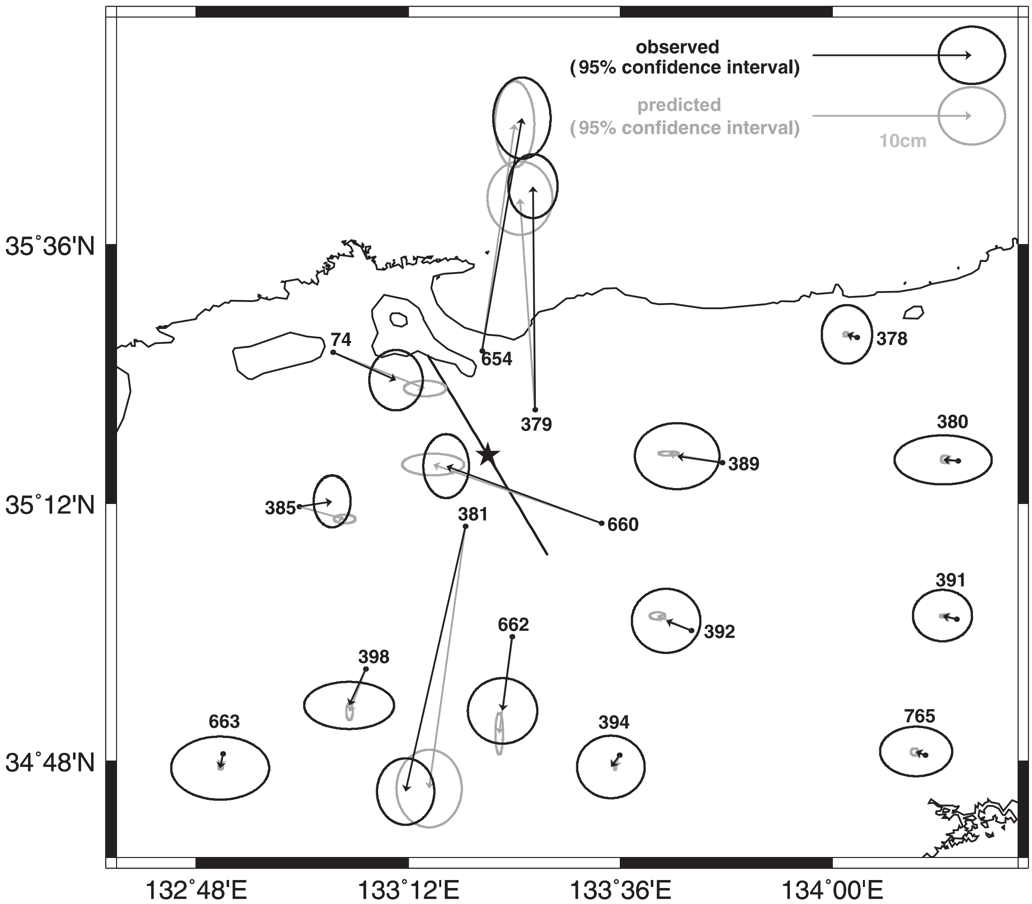

Figure 3.8: Surface static displacement produced by the selected ensemble of models (gray) compared with the one deduced from GPS data (black).

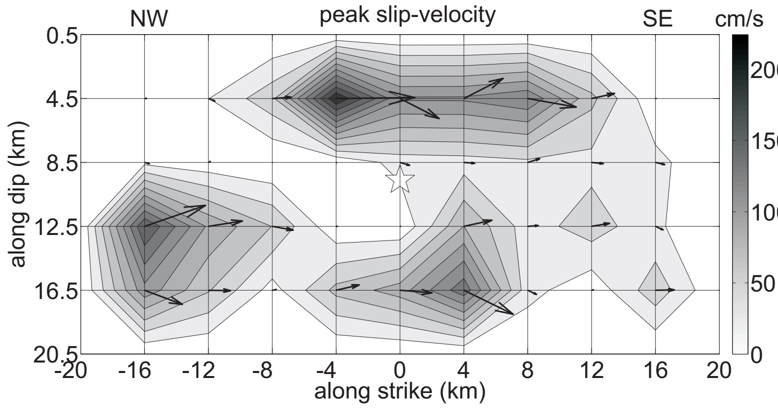

(a)

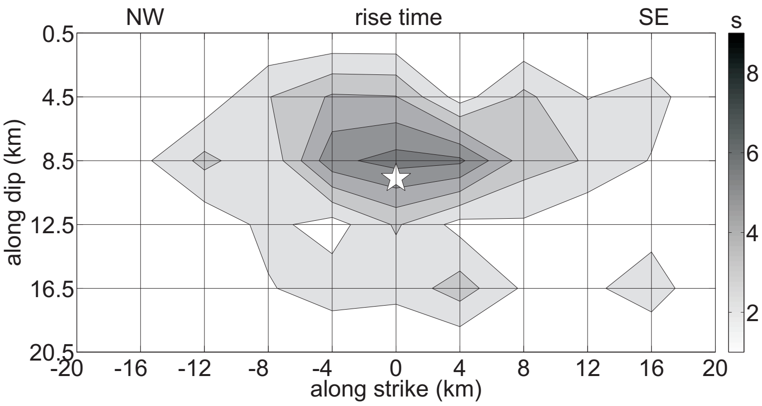

(b)

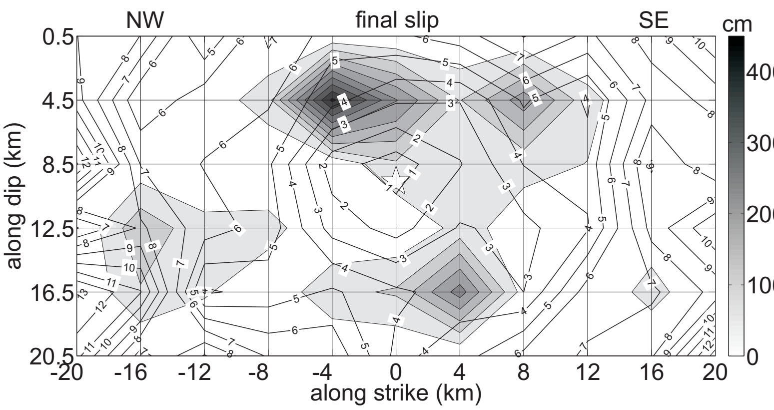

(c)

Figure 3.9: Kinematic rupture model 1.

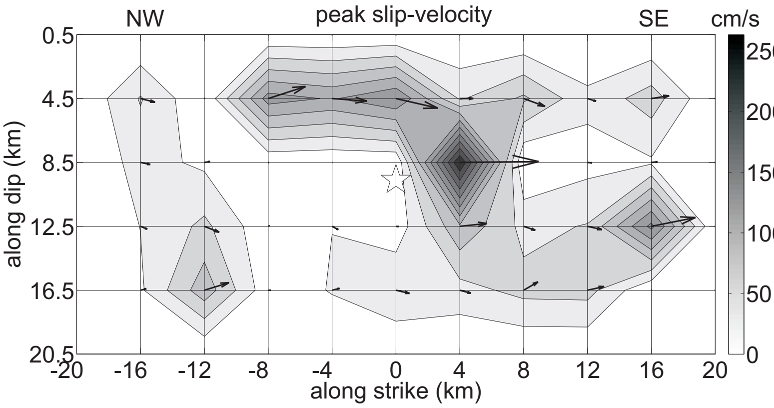

(a)

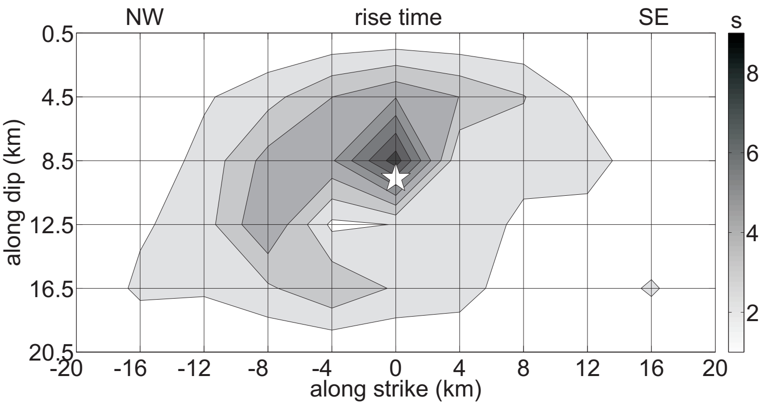

(b)

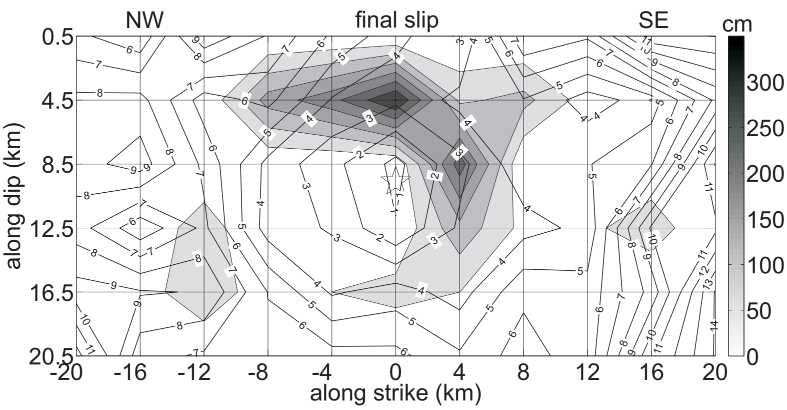

(c)

Figure 3.10: Kinematic rupture model 2.

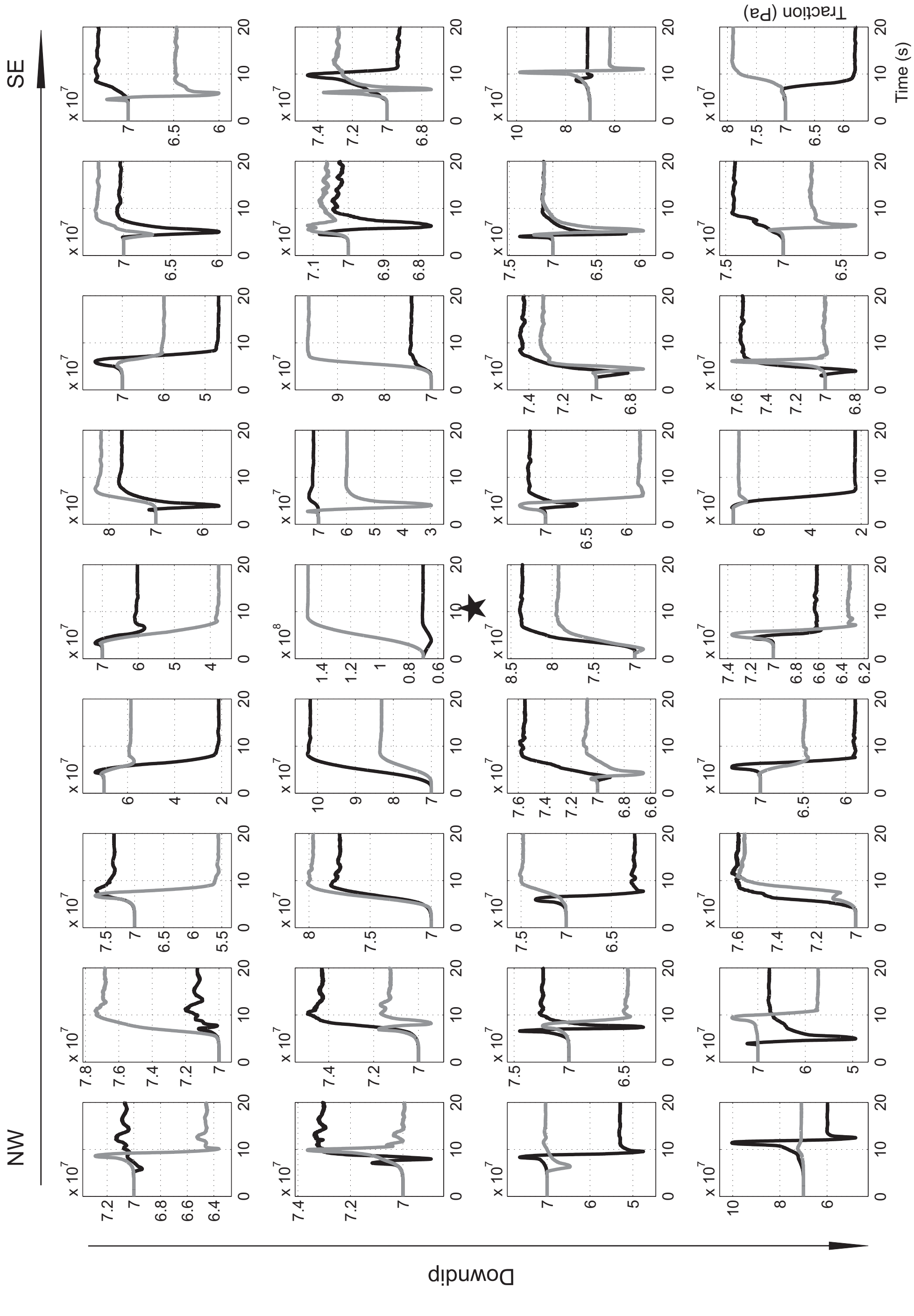

Figure 3.11: Temporal evolution of shear traction (Pa) at fault nodes produced by model 1 (black) and model 2 (gray). The black star represents the hypocentre location.

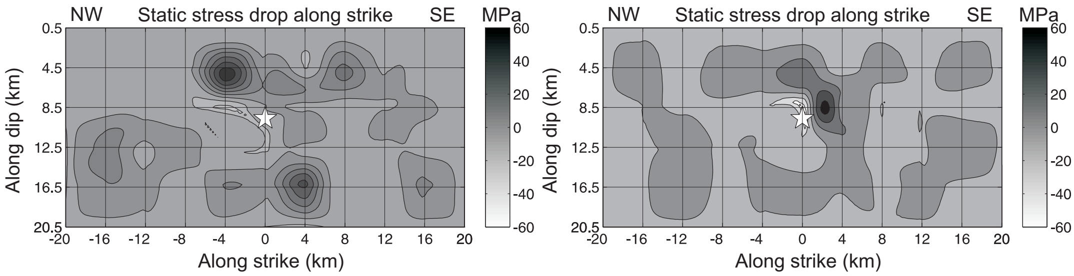

(a) (b)

Figure 3.12: Static stress drop (MPa) in the strike direction produced by model 1 (a) and model 2 (b).

model 2.

These two models illustrate how uncertainties in the estimation of a kinematic slip model propagate into the calculation of dynamic parameters. They show also how estimating uncertainties is important to understand to which degree of detail we should interpret kinematic and dynamic images of an earthquake source.

3.4 Uncertainties on static stress drop

In the previous section we have shown the case of two kinematic rupture models which provide approximately the same level of fit with the observed data, but which present several differences in the stress-fields they generate. These two models represent only two realizations of the kinematic parameters, but still illustrate the associated uncertainties. As explained in section 3.3, we now consider a set of 3000 slip models which provide a more comprehensive representation of the uncertainties that map into the variability of the dynamic source parameters. For each of these kinematic models we compute the corresponding dynamic source representation, and then examine their statistics.

The first dynamic parameter we investigate is the static stress drop. Depending only on the final slip distribution, static stress drop is less dependent than other parameters (like strength excess and dynamic stress drop) on the temporal evolution of traction which is affected by uncertainties in rise time and rupture time also.

The Tottori earthquake is mainly a strike-slip event (Fukuyama et al. [2003], Monelli et al. [2009]), with negligible or unresolved rake variability. We hence consider the static stress drop in the strike direction, which contributes most to the overall static stress drop. In Figure 3.13 we show frequency distributions of static stress drop values on the same locations where kinematic rupture parameters have been defined by Monelli et al. [2009]. We see how at the fault edges the frequency distributions are defined over negative values of stress drop and are mainly skewed toward zero. This is consistent with the condition of zero slip at the fault edges that Monelli et al. [2009] assume in their study. We see that at nodes 16 and 17, where a stable high slip patch is inferred, the frequency distributions assume approximately

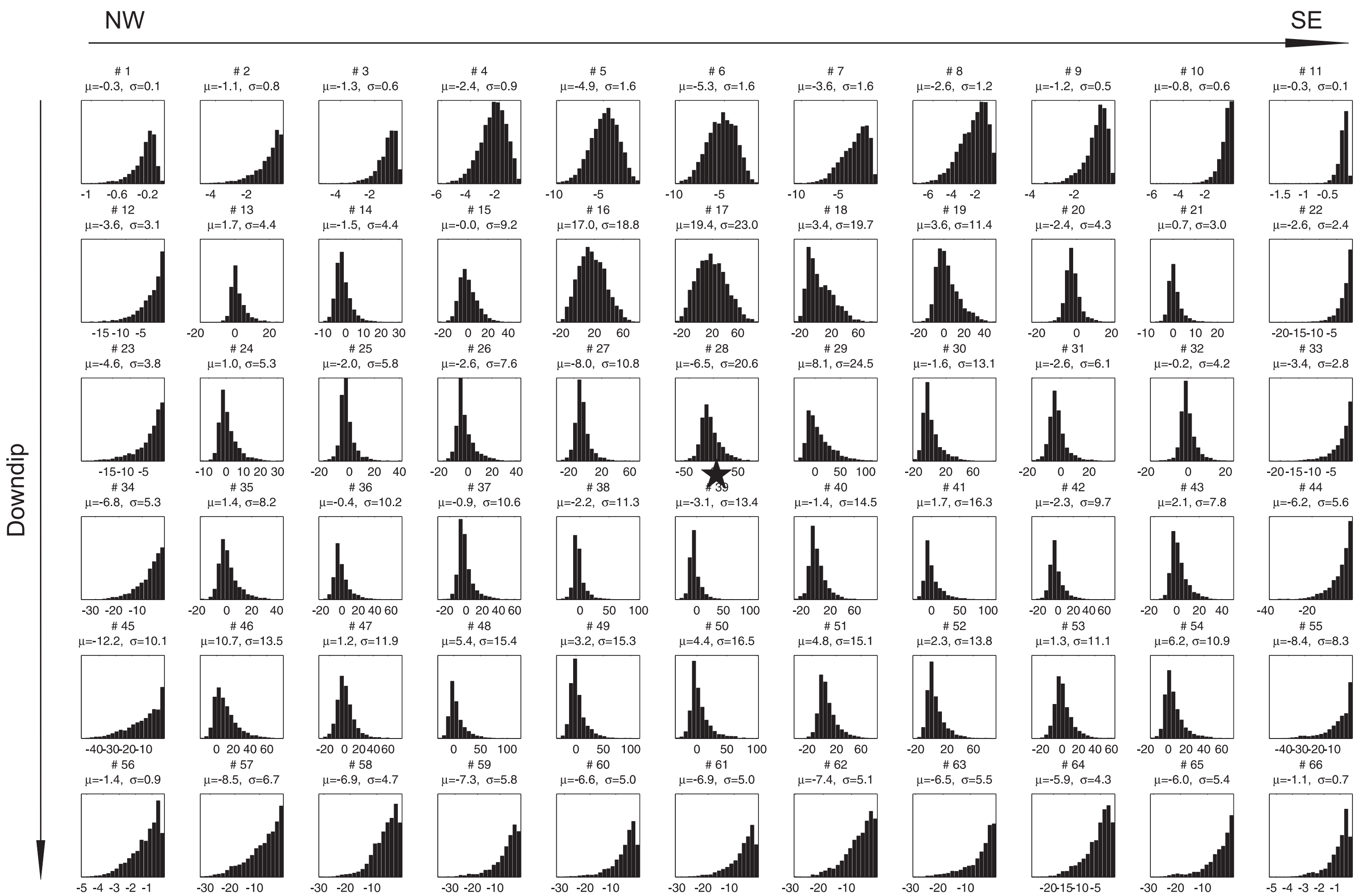

Figure 3.13: Frequency distributions for static stress drop (MPa) in the strike direction at each node location. The black star represents the assumed hypocentre location.

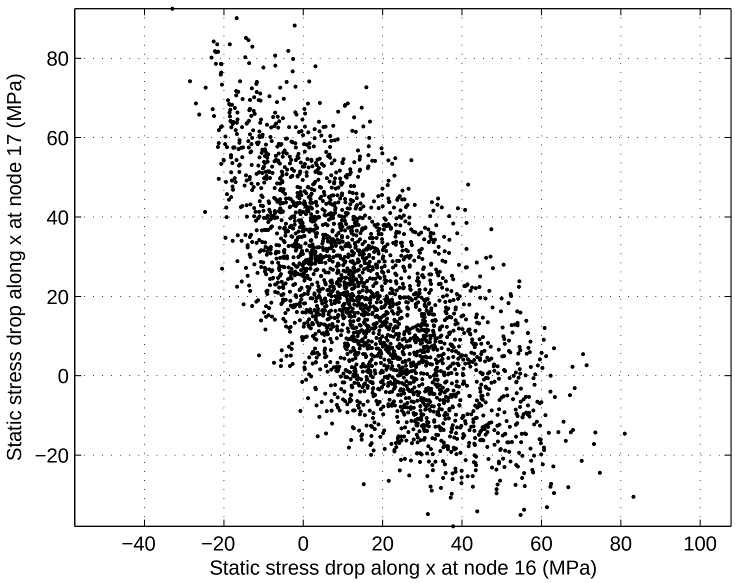

Figure 3.14: Scatter plot of static stress drop values in the strike direction at nodes 16 and 17.

a Gaussian shape with mean values and standard deviations of 17 ± 19 MPa and 19 ± 23 MPa, respectively. This means that on average these two nodes undergo a positive stress drop. However, the large standard deviations (for both nodes the relative error–ratio between standard deviation and mean value–is greater than 1) show the large uncertainties affecting the estimation of the static stress drop in these two nodes. This is also evident from the shear traction evolutions predicted by model 1 and 2 [see Figure 3.11]. We also see that at nodes 4, 5 and 6 the frequency distributions do not show a strongly skewed shape (like on the other nodes located on the edges of the fault) but rather a bell shape. For these nodes we estimate static stress drop values of -2.4 ± 0.9 MPa, -4.9 ± 1.6 MPa and -5.3 ± 1.6 MPa, respectively. For these three nodes we infer well resolved values of negative stress drop, indicating that these nodes undergo a fault restrengthening process not only because of the zero slip condition but also because they are sensitive to the stress increase due to the positive stress drop undergoing on nodes 16 and 17.

The large uncertainties associated with stress drop on nodes 16 and 17 can be explained in terms of the anti-correlation existing between static stress-drop values on these two nodes (Figure 3.14). In fact, Monelli et al. [2009] identified an anti-correlation between peak slip-velocity values defined on nodes 16 and 17. This produces an anti-correlation between final slip values (final slip = (peak slip-velocity $\times$ rise time)/2), for an isosceles triangle source time function) which translates into an anti-correlation between static stress drop values. This shows clearly how correlations between kinematic parameters map into correlations between dynamic parameters.

3.5 Uncertainties on temporal evolution of shear traction

Dynamic parameters like dynamic stress drop and strength excess are more sensitive on the temporal evolution of the shear traction. Resolution of these parameters is therefore dependent on how well we can constrain the temporal evolution of on-fault stress. To investigate this point, we compute the distribution of shear traction values at each time step on the same fault nodes used to define kinematic parameters. Due to the general non-Gaussian shape of these distributions, we characterize the range of possible values of shear traction at each time step in terms of quantiles. More precisely, we compute, at each time step, the 0.025 and 0.975 quantiles of the corresponding distribution of shear traction values. This approach allows us to specify, at each time step, the 95 percent confidence level. We show the results of this analysis in Figure 3.15. To understand if these confidence levels really capture the uncertainties affecting the shear traction temporal evolution, we plot also the shear traction time histories produced by model 1 and 2. We see that for all nodes except nodes 27, 28 and 30, the traction time histories from both models lie inside the confidence levels. We see also that the confidence levels are wide enough to contain the large differences in traction evolution we see on nodes 15, 16, 51 and 62, for instance.

From this analysis we see that the estimation of the shear traction temporal evolution on a certain location on the fault is subject to large uncertainties. On all the inner nodes, the 95 percent confidence level extends from shear traction values lower than the initial value to values greater than initial value, indicating therefore that there is always a finite probability of having both a fault weakening or a fault strengthening process.

3.6 Uncertainties on radiated energy

From the previous section, we see that imaging the rupture process on a single location on the fault is subject to large uncertainties. We hence explore resolution of global quantities, which reflect the rupture process on the whole fault surface. A global quantity which reflects the spatio-temporal evolution of both slip and traction over the entire fault is the radiated energy. The radiated energy E_R is defined as the amount of energy that would be carried to the far field in the form of seismic waves if an earthquake occurred in an infinite and non-attenuating medium. It can be calculated from either the far-field seismic waves or the stress and displacement on the fault plane. Rivera & Kanamori [2005] show that the radiated energy E_R can be computed as:

$$E_R = \frac{1}{2}\int_{\Sigma}(\sigma^1_{ij} - \sigma^0_{ij})\Delta u_i \nu_j dS - \int_{\Sigma} 2\gamma_{eff} dS - \int_{t_0}^{t_1} dt \int_{\Sigma(t)}(\sigma_{ij} - \sigma^0_{ij})\Delta \dot{u}_i \nu_j dS \tag{3.1}$$

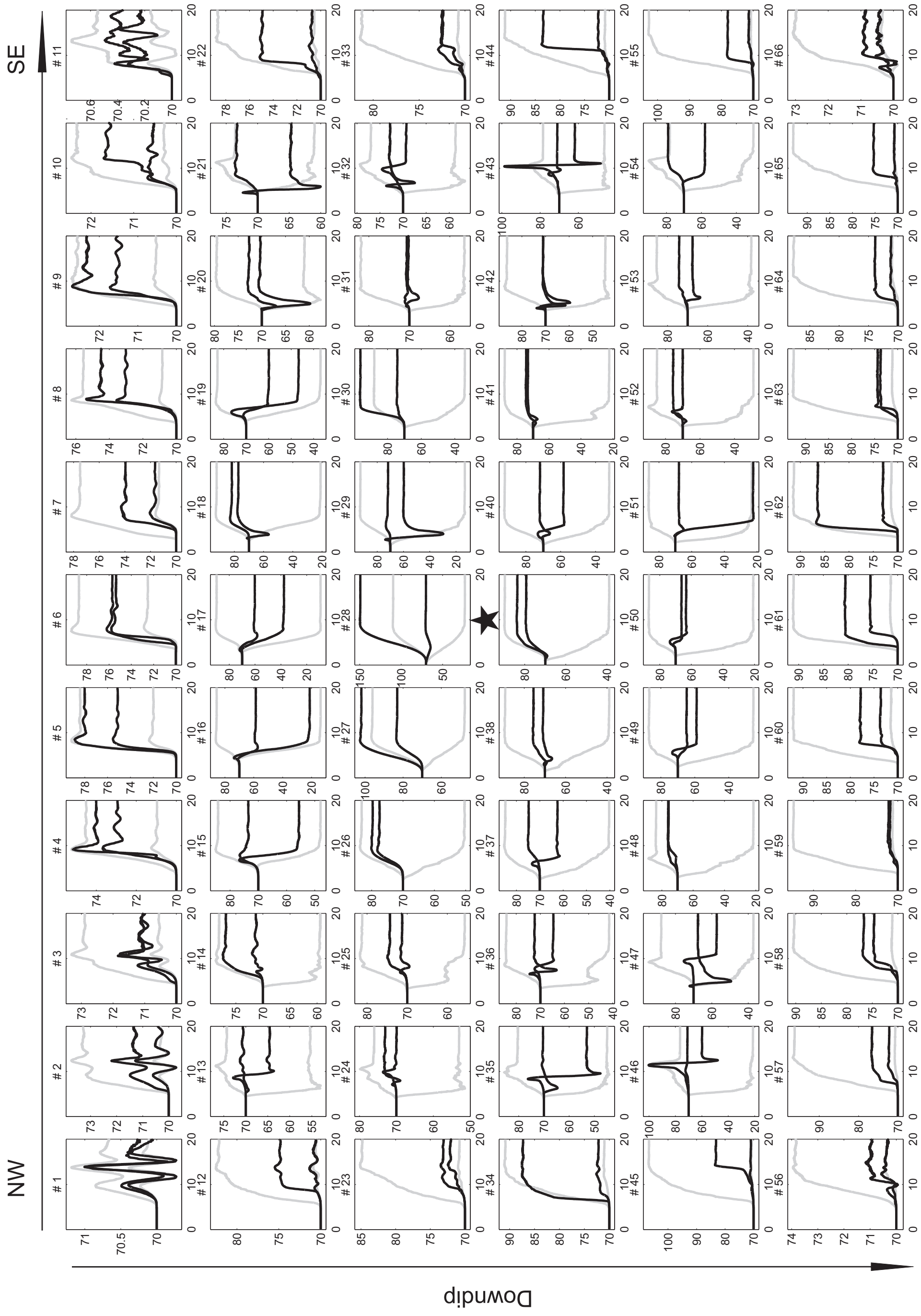

Figure 3.15: 0.025 and 0.975 quantiles (solid gray lines) computed from the distribution of traction values at each time step, for each node. We show also shear traction time evolutions (black solid lines) produced by model 1 and 2.

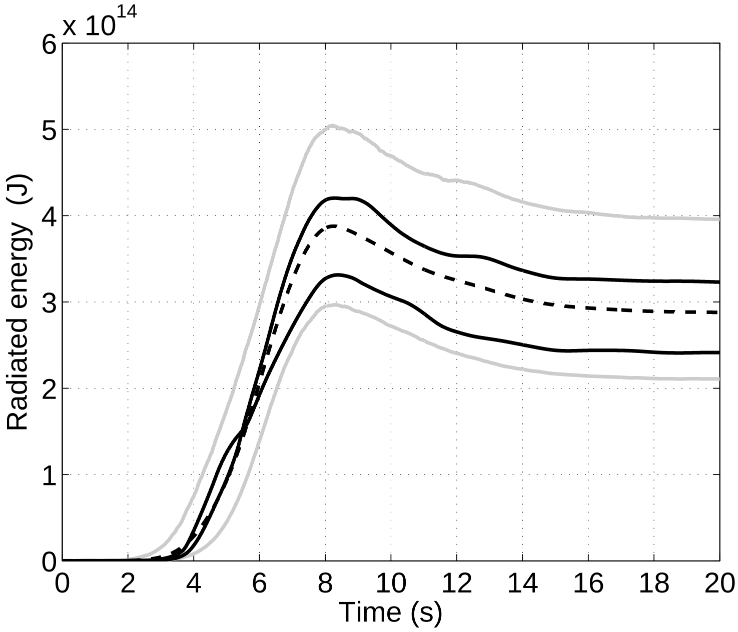

Figure 3.16: 0.025 and 0.975 quantiles (solid gray lines) computed from the distribution of radiated energy values at each time step. We show also the average radiated energy (dashed black line) and the radiated energy produced by model 1 and 2 (solid black lines).

where Σ represents the fault surface, σ_{ij}^0 the initial stress at a reference time t_0, σ_{ij}^1 the stress acting at time t_1, u_i the slip, $\dot{u}_i$ the slip-velocity and ν_j the unit vector normal to Σ. γ_{eff} is the effective surface energy, a lumped parameter including all dissipation within the process zone at the crack-tip. That is, it includes not only surface energy, but also other dissipative mechanisms such as heat. Cocco et al. [2006] pointed out that for crack models in which the stress is not singular at the crack tip (like in our case), the effective surface energy is zero. In our study, we compute therefore the radiated energy for each kinematic model using Equation 3.1, neglecting the second term on the right-hand side.

In Figure 3.16 we show the 0.025 and 0.975 quantiles computed from the distribution of radiated energy values at each time step. We show also the average radiated energy, and the radiated energy produced by models 1 and 2. In this case uncertainties allow us to identify a clear temporal evolution for radiated energy. We see that only between 2 and 4 s E_R starts increasing. This is consistent with the fact the main slip patch is triggered on average only 3 s after the earthquake nucleated [Monelli et al., 2009]. Radiated energy reaches a maximum value at around 8 s and then decreases reaching approximately a stationary level. The final average radiated energy is equal to 2.9×10^{14} J which is consistent with the estimates of Izutani & Kanamori [2001] (3.0×10^{14} J) and of Jin & Fukuyama [2005] (3.1×10^{14} J). The decrease of radiated energy is due to the rupture termination. In other words, the reduction of radiated energy during the later stages of the rupture process is due to those regions of the fault surface which experience a strengthening process and therefore absorb energy without emission of seismic waves.

3.7 Discussion and conclusions

Explaining a given kinematic slip model in terms of dynamic parameters is important to understand how the weakening process occurs on real faults and therefore how we can realistically parameterise a dynamic rupture model to predict a future earthquake. Guatteri & Spudich [2000] discuss the issue of estimating linear slip-weakening parameters from a kinematic slip model obtained trough fitting of strong motion data. They find a trade off between strength excess and slip-weakening distance which do not allow them to identify a unique set of dynamic parameters which explain a given kinematic slip model. They conclude that if static-stress drop is well determined than only fracture energy can be reliably resolved. In other words, if the final slip distribution is well inferred, all the uncertainties on dynamic parameters come from the intrinsic trade off existing between the dynamic parameters themselves.

However, our study shows that uncertainties in kinematic rupture parameters (and on final slip therefore) are not negligible. These uncertainties have immediate consequences on the estimation of dynamic parameters. For the Tottori earthquake, we see that static stress drop is only qualitatively well inferred. Stress drop on locations where high slip is estimated have positive values on average, indicating therefore a weakening process. However, the associated standard deviations are of the same order as the estimated average values indicating therefore large uncertainties which do not allow us to identify well resolved static stress drop values. We see that these large uncertainties are also due to a trade off that is inherited from the estimated kinematic parameters. This is important to notice, because it shows that not only the uncertainties but also the statistical properties of the uncertainties (like correlations) map into the estimation of dynamic parameters. The large uncertainties on static stress drop reflect the large uncertainties in the the temporal evolution of shear traction.

Our study shows that the inference of the on-fault stress evolution during an earthquake rupture is subject to large uncertainties. Resolution of kinematic parameters is not sufficient to infer the stress evolution on a single location of the fault. These large uncertainties are basically due to the limited amount of data and the limited frequency band. We can expect that increasing the spatial coverage of the recording stations and the maximum considered frequency may improve resolution of both kinematic and dynamic parameters. With the available data we find that only parameters characterising the overall rupture process over the entire fault surface (e.g. radiated energy) can be well resolved.

Chapter 4

A linear slip-weakening model for the 2000 Western Tottori earthquake

Abstract

In this study we derive a dynamic rupture model for the 2000 Western Tottori earthquake based on a linear slip-weakening friction law. Our analysis develops in three stages. First, using a Bayesian approach we estimate kinematic rupture parameters (peak slip-velocity, rake angle, rise time, rupture time) by fitting strong motion and GPS data. Second, using a dynamically consistent source time function (regularized Yoffe function), we compute the spatio-temporal evolution of on-fault stress associated with the mean kinematic slip model. Third, estimating dynamic stress-drop, strength excess, and slip-weakening distance, we derive a linear slip-weakening model for the rupture process. We obtain a dynamic rupture model able to reproduce the observed kinematic parameters. We compare also the predicted ground motion with the near-field strong motion and GPS data. We find that the level of fit provided by the dynamic model is comparable to that of the best-fitting kinematic model. We consider this result of particular practical importance, because the dynamic model has been obtained without an explicit optimization procedure but rather interpreting a mean kinematic slip model by using a dynamically consistent source time function.

4.1 Introduction

The ground motion produced by an earthquake on a certain location on the Earth surface is due to three main effects: the source, the path and the site. To realistically model all these factors, state-of-the-art ground motion simulations employ 3D Earth structures and finite fault dynamic rupture models (Olsen et al. [2008], Olsen et al. [2009]).

In a dynamic rupture model the spatio-temporal evolution of slip results from solving the elastodynamics equations, and by assuming a friction law to describe the fault slip process. Parameters, usually referred as “dynamic”, are required to define the initial state of stress and the friction law itself.

To derive realistic dynamic rupture models, dynamic parameters are usually constrained from past earthquakes. Two approaches are possible. One requires estimating kinematic parameters first. The inferred spatio-temporal evolution of slip is then used as a boundary condition to solve the elastodynamics equations for the on-fault stress, from which dynamic parameters can be estimated (Ide & Takeo [1997], Bouchon [1997], Dalguer et al. [2002], Tinti et al. [2005b]). As noticed by Piatanesi et al. [2004], in this methodology the estimation of dynamic parameters can be biased by the assumed source time function. An alternative approach is to perform a dynamic inversion, that is a search for the sets of dynamic parameters which produce the best level of fit with the observed ground motion. In this approach the source time function at each location on the fault is not chosen a priori but is a solution of the dynamic rupture problem. The most common dynamic inversions are based on a trial and error approach, where an initial dynamic model, usually constrained from a previously estimated kinematic model, is manually modified until satisfactory fit with the data is achieved (Peyrat et al. [2001], Favreau & Archuleta [2003], Ma & Archuleta [2006], Ma et al. [2008]). To our knowledge, a systematic dynamic inversion has been performed only for the 2000 Western Torrori earthquake by Peyrat & Olsen [2004]. In their study, the authors use a direct search method based on the Neighbourhood algorithm to estimate stress drop distribution assuming a linear slip-weakening fault model with uniform upper yield stress and slip-weakening distance.

The goal of our study is to extend the work of Peyrat & Olsen [2004] deriving a linear slip-weakening rupture model for the 2000 Western Tottori earthquake with heterogeneous distribution of strength excess, dynamic stress drop, and slip-weakening distance. We first estimate kinematic parameters using a Bayesian approach. This analysis shows that multiple kinematic models may produce satisfactory level of fit with the observed data. We hence consider the mean kinematic slip model as representative of the most likely features of the earthquake rupture process. Using the mean kinematic slip model and a dynamically consistent source time function (regularized Yoffe function proposed by Tinti et al. [2005a]), we compute the spatio-temporal evolution of on-fault stress, from which we estimate strength excess, dynamic stress drop, and slip-weakening distance distributions on the fault surface. These estimates are then used to define a linear slip-weakening model for the rupture process. The predicted ground motion is then compared with the observed strong motion and GPS data.

4.2 Bayesian inference of kinematic rupture parameters

Monelli et al. [2009] inferred kinematic rupture parameters for the 2000 Western Tottori earthquake using a Bayesian approach. In this study we repeat their analysis using the same methodology, same data (strong motion+GPS), same modeling scheme, but considering a larger model space. Monelli et al. [2009] observed that for some parameters the solution converged toward the upper bound of the considered range of values, possibly suggesting that the solution is located above the imposed upper limit.

We refer to Monelli et al. [2009] for the details of the inversion procedure. Here we recall the main results. The solution of the inverse problem is stated in terms of a posterior probability density function (PDF) which represents the conjunction of prior information on model parameters and information derived through fitting of the observed data. The posterior pdf is expressed as:

$$\sigma^{sm,gps}(\mathbf{m}) = k\rho(\mathbf{m})L^{sm}(\mathbf{m})L^{gps}(\mathbf{m}). \tag{4.1}$$

where k is a normalization constant, $\rho(\mathbf{m})$ is the PDF representing prior information on model parameters $\mathbf{m}$ (a uniform PDF in this study), and $L^{sm}(\mathbf{m})$ and $L^{gps}(\mathbf{m})$ are the likelihood functions (measuring how well a model $\mathbf{m}$ explains the data) for strong motion and GPS data, respectively [Eq. 8 and 11 in Monelli et al. [2009], respectively]. Information on a single model parameter can be expressed in terms of a 1D posterior marginal PDF, given by:

$$M(m^{\alpha}) = \int ... \int \sigma^{sm,gps}(\mathbf{m}) \prod_{\substack{k=1 \\ k \neq \alpha}}^{M} dm^k \tag{4.2}$$

where m^{α} is the considered model parameter. Eq. 4.2 requires integrating the posterior PDF over all dimensions of the model space (M) except the one corresponding to the parameter of interest.
Data consist of ground velocity waveforms from 18 strong motion stations and surface static displacements from 16 GPS stations (Fig 4.1). Original strong motion data were bandpass filtered in the frequency band 0.1-1 Hz, whereas coseimic static offset at each GPS station was estimated as the difference between mean values of daily positions during the 5 days before and the 5 days after the earthquake.

We represent the fault as a 24 km long and 16 km deep, vertically dipping plane surface, with a strike of $150°$ degrees. The fault upper edge is at 0.5 km depth. Monelli et al. [2009] used a longer and deeper fault plane. However, they noticed that good resolution on model parameters is achieved mostly in the central and upper part of the fault. In this study, we consider therefore a smaller fault surface, which helps in decreasing the total number of parameters.
On the fault surface, we define a regular grid of nodes, with a spacing of 4 km along-strike and along-dip. The total number of nodes on the fault is therefore 35. At each node we define 4 parameters: peak slip-velocity, rake angle, rise time, rupture time. The total number of parameters is therefore 140.

We compute ground velocities using the frequency-domain representation theorem [Spudich & Archuleta, 1987]:

$$\dot{u}_m\left(\mathbf{y},\omega\right) = \iint_{\Sigma} \dot{\mathbf{s}}\left(\mathbf{x},\omega\right) \cdot \mathbf{T^m}\left(\mathbf{x},\omega;\mathbf{y},\mathbf{0}\right) \mathbf{d\Sigma} \tag{4.3}$$

where $\dot{u}_m$ is the m^{th} component of ground velocity at the receiver location $\mathbf{y}$, $\dot{\mathbf{s}}$ is the slip-velocity function, $\mathbf{T^m}$ is the traction exerted across the fault surface Σ at point $\mathbf{x}$ generated by an impulsive force applied in the m^{th} direction at the receiver ($\omega = 2\pi f$: angular frequency). Tractions $\mathbf{T^m}$ are computed, up to a frequency of 1 Hz, using a Discrete Wavenumber / Finite Element method [Compsyn package, [Spudich & Xu, 2002]], for a 1D flat layered Earth model without attenuation. A trapezoidal-rule quadrature of the product $\dot{\mathbf{s}} \cdot \mathbf{T^m}$ is performed separately for each frequency, with the quadrature points being the sample points where $\mathbf{T^m}$ have been computed. Rupture-parameter values at integration points are derived through bilinear interpolation of values at surrounding grid nodes.

We assume the slip-velocity function to be an isosceles triangle. With this parametrization the peak-slip velocity corresponds to the height of the triangle and the rise time to the base length. Rupture time corresponds to the first point of the base segment.

Following Eq 4.3, we convolve tractions with the assumed slip-velocity function to compute ground velocity at the strong motion station locations. We compute

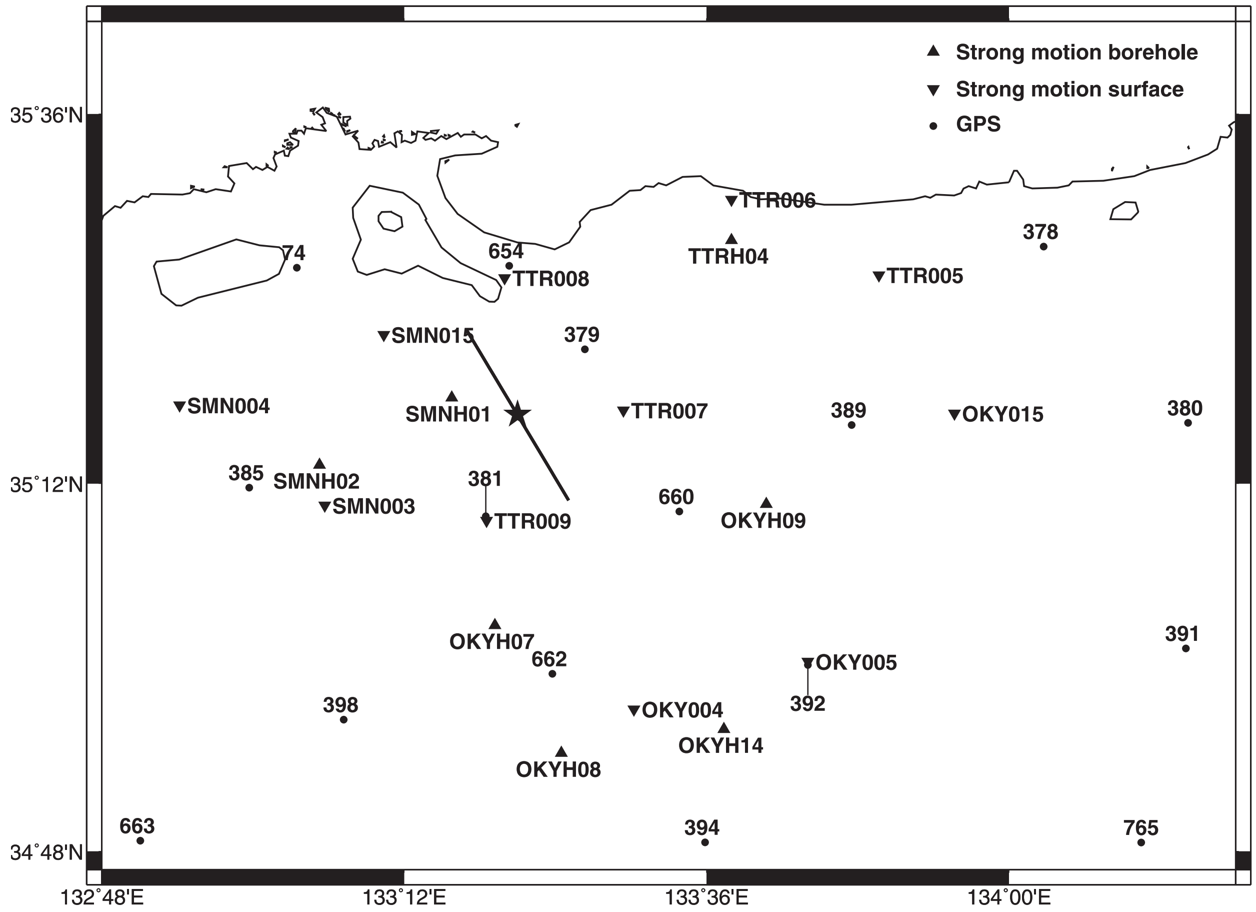

Figure 4.1: The observational network consists of 18 strong motion stations (black triangles) and 16 GPS stations (black dots) located within about 90 km from the epicentre (black star). We use 7 borehole stations (upward-pointing triangles) and 11 surface stations (downward-pointing triangles). The black solid line indicates the assumed fault strike (150°).

GPS data predictions by integrating ground velocities to ground displacements and then selecting the final static offsets.

The posterior PDF is defined over the model space. Inferences on model parameters are therefore dependent on the chosen model space. Monelli et al. [2009] find that the computed 1D posterior marginals are skewed toward the upper limit of the considered range of values for some parameters (especially for rise time and rupture time), suggesting that the solution is located above the imposed upper limit. To test this hypothesis we consider a larger model space in this study. As in Monelli et al. [2009], peak slip-velocity can vary between 0 and 400 cm/s on the inner nodes of the fault. On the fault edges we assume a zero-slip condition (peak slip-velocity is forced to be zero therefore). Rake angle can vary between $-90°$ to $+90°$ degrees (Monelli et al. [2009] assumed $-30°$ to $+30°$ degrees). The range of rupture times at each grid node is defined as the interval between the arrival times of two circular rupture fronts, propagating from the hypocenter [at 9.6 km depth [Fukuyama et al., 2003]] at two limiting rupture velocities: 1 and 4 km/s (Monelli et al. [2009] considered 1.5 and 4 km/s). Rise time can vary between 1 and 10 s on all the inner nodes (Monelli et al. [2009] assumed minimum value equal to 1 s and a maximum value decreasing as the distance from the hypocenter of the considered node increases). Rise time on the fault edges is assumed equal to 1 s (to generate rise time distributions which are tapered to the minimum value at the fault edges). Considering the zero-slip condition and the minimum rise time assumption at the fault edges, the number of free parameters is 104.

4.3 1D marginals for kinematic parameters

We estimate 1D marginals using a Markov Chain Monte Carlo (MCMC) method, based on the Metropolis algorithm [Monelli et al., 2009]. We simulate three random walks, each of them producing 890000 samples. To get approximately independent samples we collect models every 100 steps. From each random walk we extract therefore 8900 models. All the produced samples are then merged into a single ensemble to estimate 1D marginals.

In Fig. 4.2 we show 1D marginals for peak slip-velocity. They show the same pattern obtained by Monelli et al. [2009]: that is an evident high slip-velocity patch (peak value of 206 ± 89 cm/s) located between the hypocenter and the top edge of the fault (nodes 2 and 3). On the other nodes posterior marginals are skewed toward the minimum allowed value (0 cm/s). This means that, except nodes 2 and 3, we cannot identify any other node slipping with a clear high slip-velocity value. This does not mean that a node cannot slip with an high slip-velocity, but rather that we have not enough resolution to say which node is slipping with high slip-velocity. We see also that the skewness of the posterior marginals is not uniform on the fault surface. In particular, we observe that on the nodes located SE of the hypocenter the posteriors skewness is lower than in the NW. This means that the probability of having nodes slipping with high slip-velocity values is higher in the SE section of the fault rather than in the NW. This features are consistent with the kinematic images obtained for this earthquake (Semmane et al. [2005], Festa & Zollo [2006], Piatanesi et al. [2007]), which show significant slip above the hypocenter and elongated toward SE.

The fact that the observed wavefield is dominated by the energy coming from the high slip-velocity patch located on nodes 2 and 3 is confirmed by the good resolution of the rake angle for these two nodes (Fig. 4.3). On nodes 2 and 3 we clearly see that the slip process is mainly strike-slip, in agreement with the focal mechanism estimation [Fukuyama et al., 2003]. We see also that posterior marginals located SE of the hypocenter (nodes 4, 5, 10) show a broad peak around +10/+15 degrees (in our modeling corresponding to a down-dip movement). However, the large uncertainties (standard deviations of the order of 40 degrees) do not allow us to draw definite conclusions. We observe also that NW of the hypocenter, at the bottom of the fault (nodes 11, 12), the posterior marginals are evidently skewed toward negative values of the rake angle (corresponding to an up-dip movement). We see therefore that posterior marginals for rake angle show clear (although broad) peaks on nodes where the posterior marginals for peak slip-velocity do not identify clear high slip-velocity values. We can interpret this fact saying that even if the posterior PDFs for peak slip velocity assign the highest probability near 0, there is still finite probability of having non-zero, significant, slip-velocities. If this occurs then the rake angle can be inferred.

The 1D marginals for rise time (Fig. 4.4) do not show exactly the same pattern as in Monelli et al. [2009]. This differences are produced by the different model space. However, we still see that in the central part of the fault, near the hypocenter (nodes 7 and 8), the posterior marginals show a broad peak around 5.5 and 6.2 s, respectively. On the other nodes posteriors are mostly skewed toward the minimum allowed value (1 s). We observe therefore a pattern where higher values of rise time are more likely to appear in the central part of the fault, near the hypocenter, whereas lower values are more likely approaching the edges of the fault.

Rupture time results to be well inferred (Fig. 4.5). We see evident peaks above the hypocenter and SE of it. On nodes 2 and 3, the rupture time is about 4.7 ± 0.8 and 3.8 ± 0.7 s, respectively. The percentage errors are about 17 and 18 percent, respectively. For rupture time we see clearly what we noticed for the rake angle, that is posterior marginals show evident peaks even on those nodes for which no clear high slip-velocity is identified.

Fig. 4.6 show 1D marginals for final slip. We see that the prior PDF is not uniform anymore because it represents information on a combination of the original model parameters. We see again that at nodes 2 and 3, the inferred high slip-velocity values produce an high slip-patch (mean value of about 3 m), consistent with the estimate provided by Monelli et al. [2009]. We also see that the probability of having high values of final slip is higher in the SE section of the fault rather than in the NW (compare posteriors at nodes 4, 5, 9, and 10, with posteriors at nodes 1,6, and 7, for instance).

To compute the spatio-temporal evolution of on-fault stress we use a velocity-stress staggered-grid finite difference scheme, based on the Staggered-Grid Split-

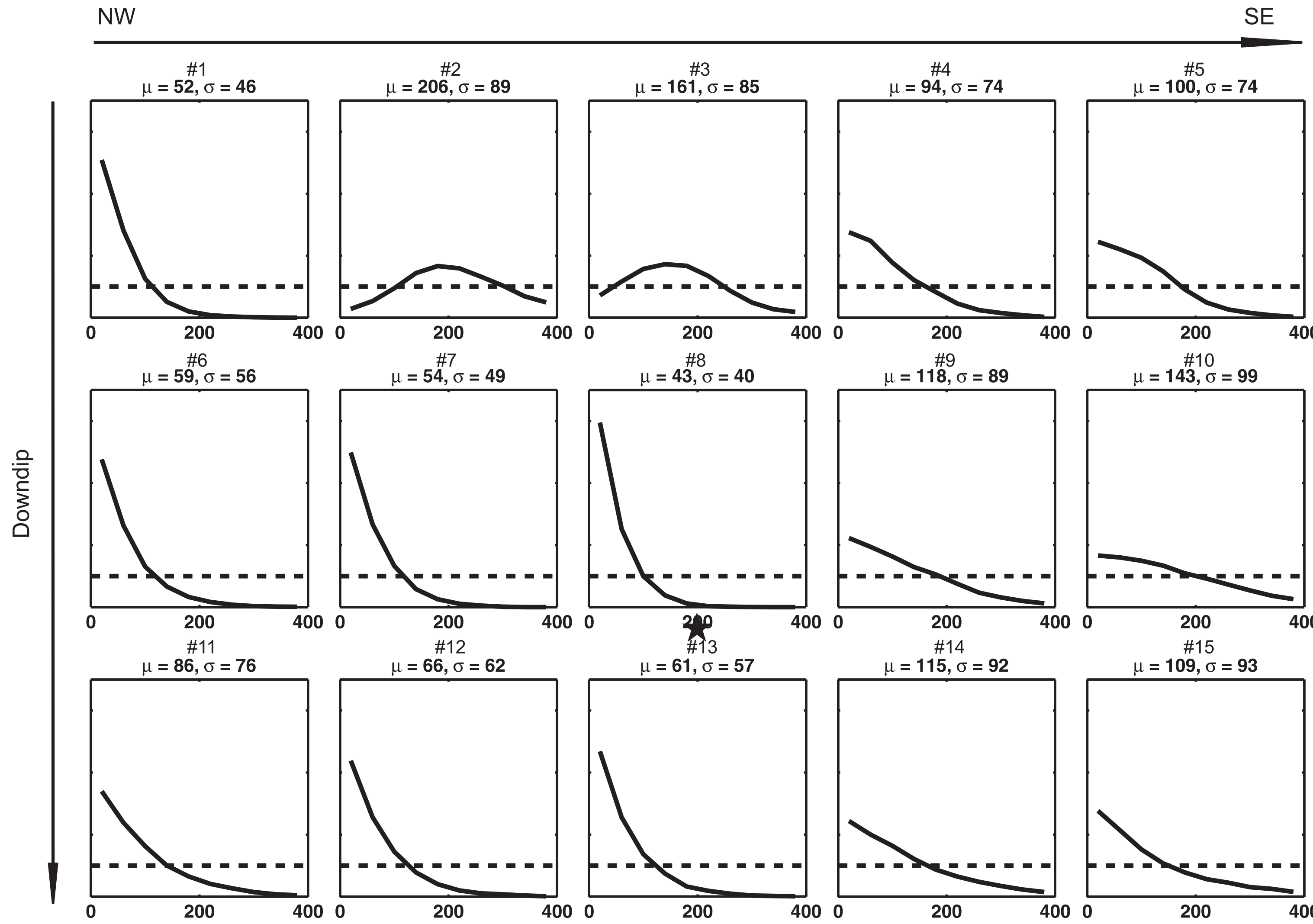

Figure 4.2: 1D marginals for peak slip-velocity (cm/s). Each subplot corresponds to a inner node position. Dashed lines represent priors, solid lines posterior marginals. For each subplot we indicate the node number, mean value (μ) and standard deviation (σ). The black star represents the hypocentre location.

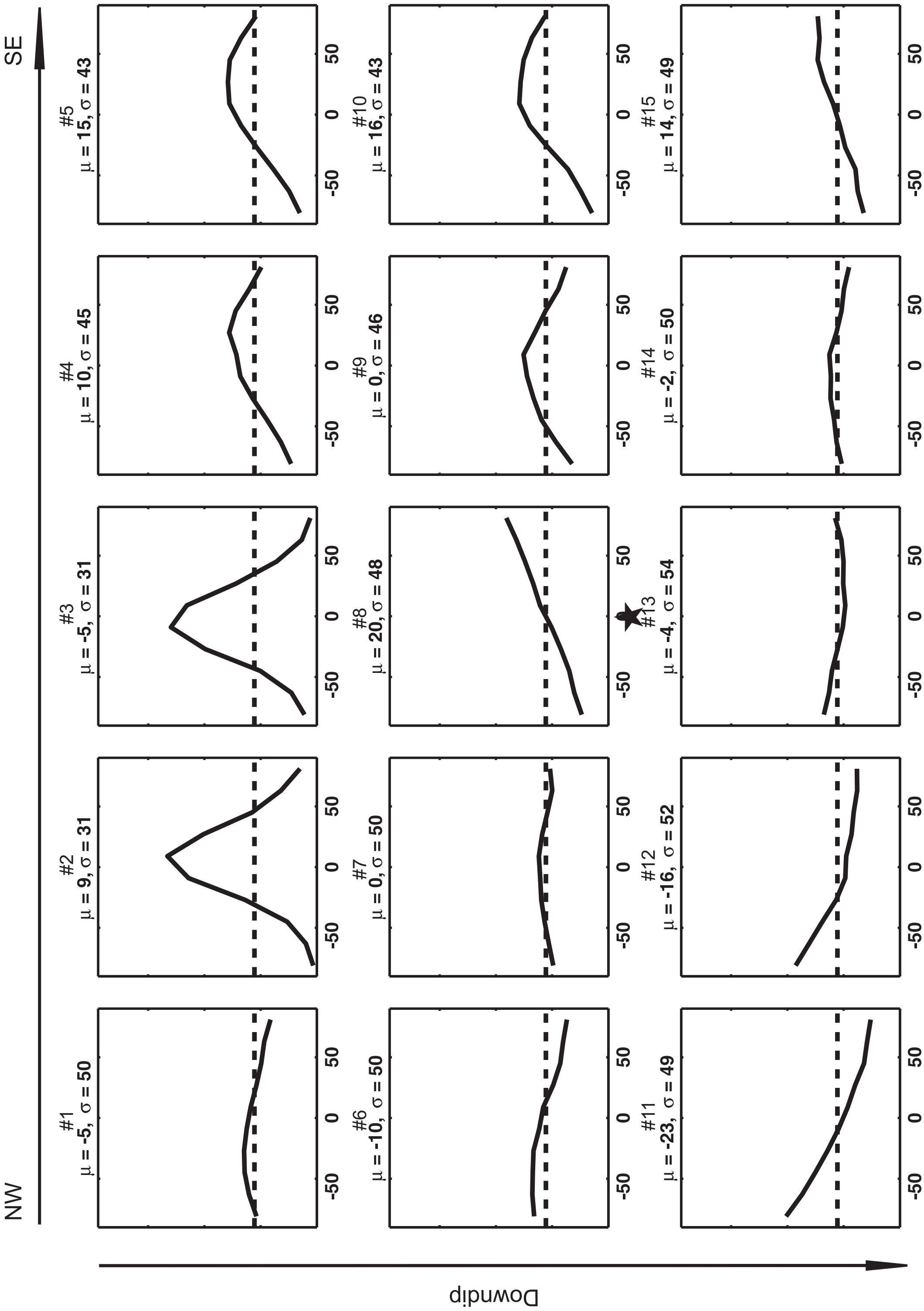

Figure 4.3: 1D marginals for rake angle (degree). Same notation as in Fig 4.2

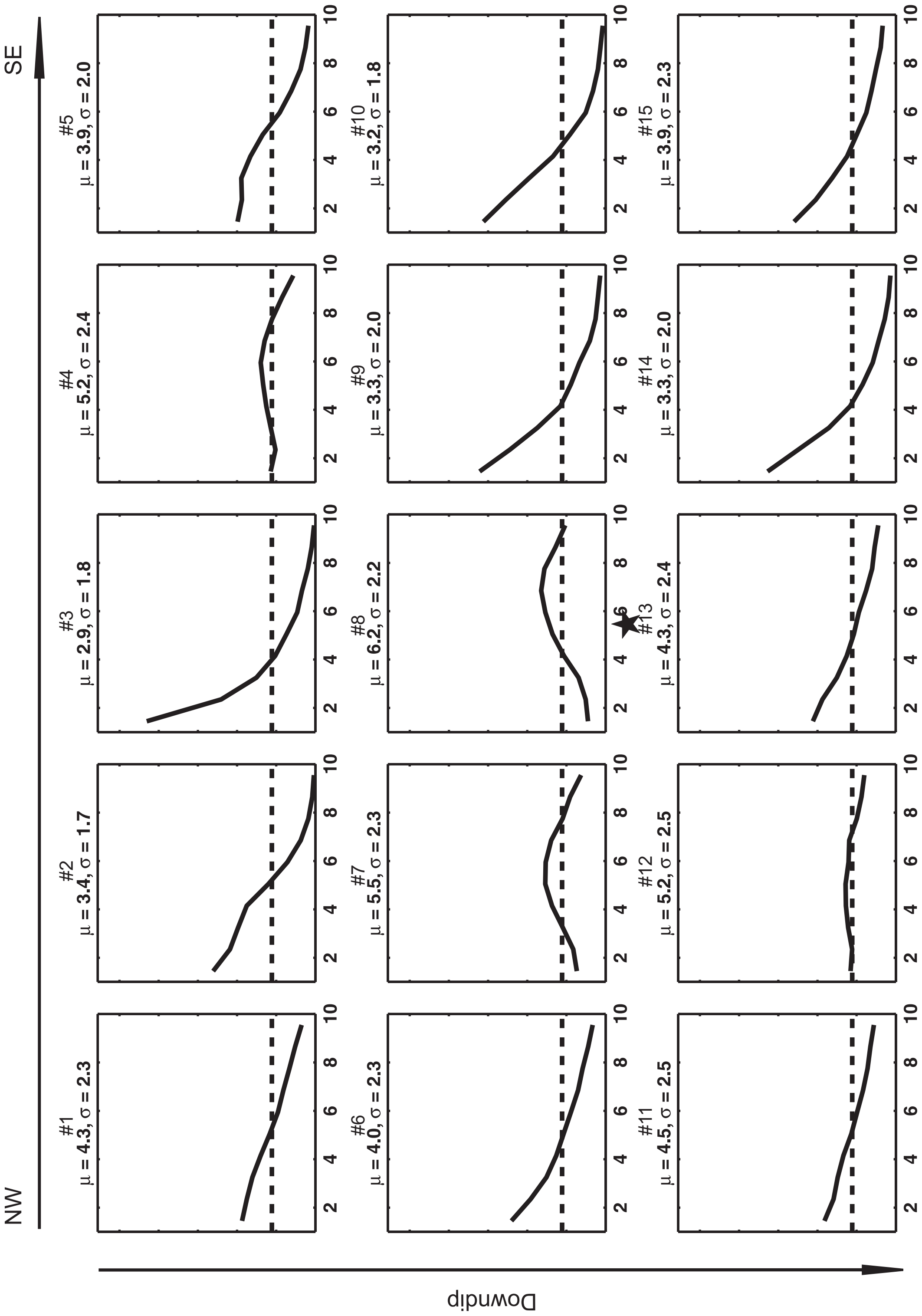

Figure 4.4: 1D marginals for rise time (s). Same notation as in Fig 4.2

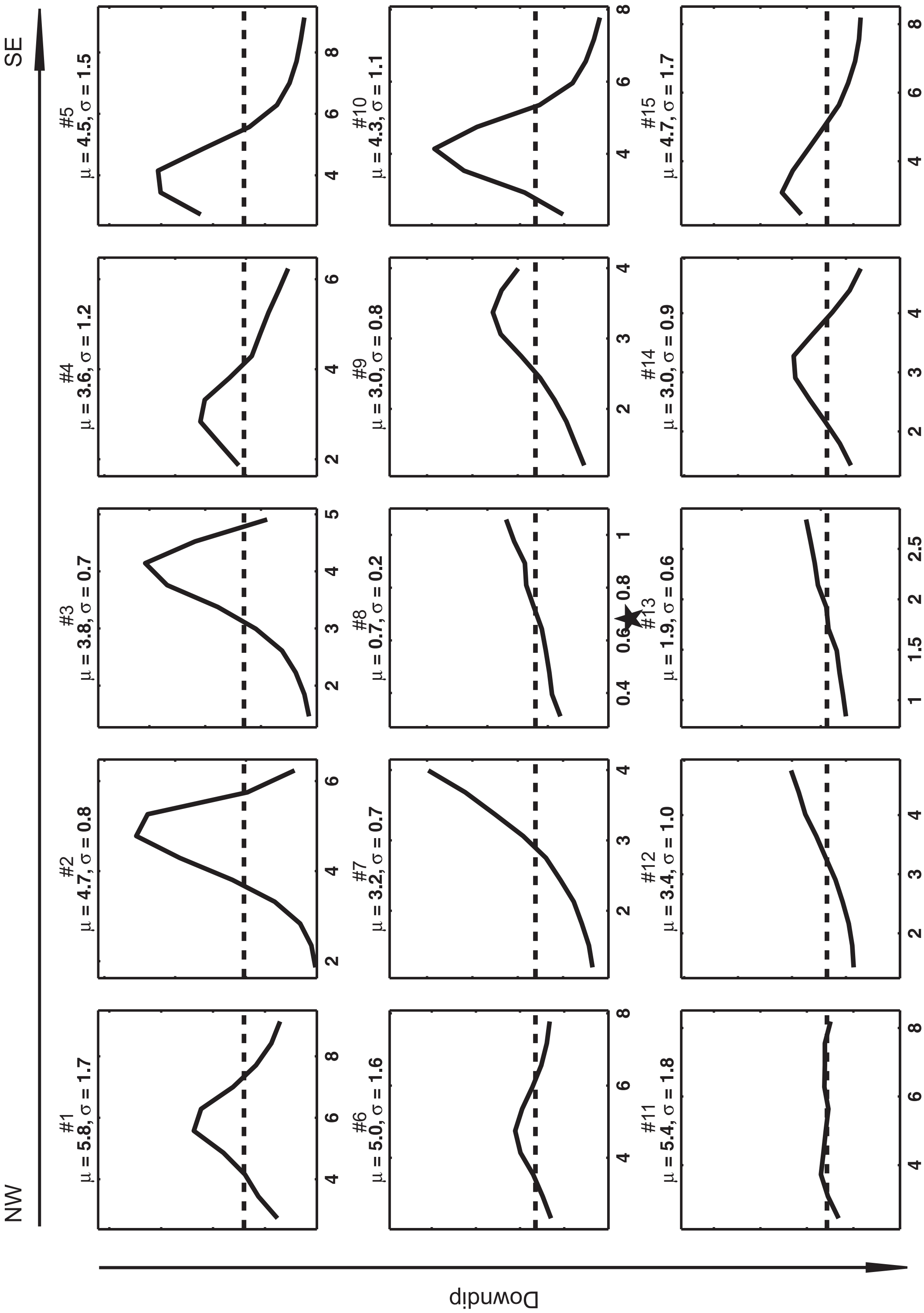

Figure 4.5: 1D marginals for rupture time (s). Same notation as in Fig 4.2

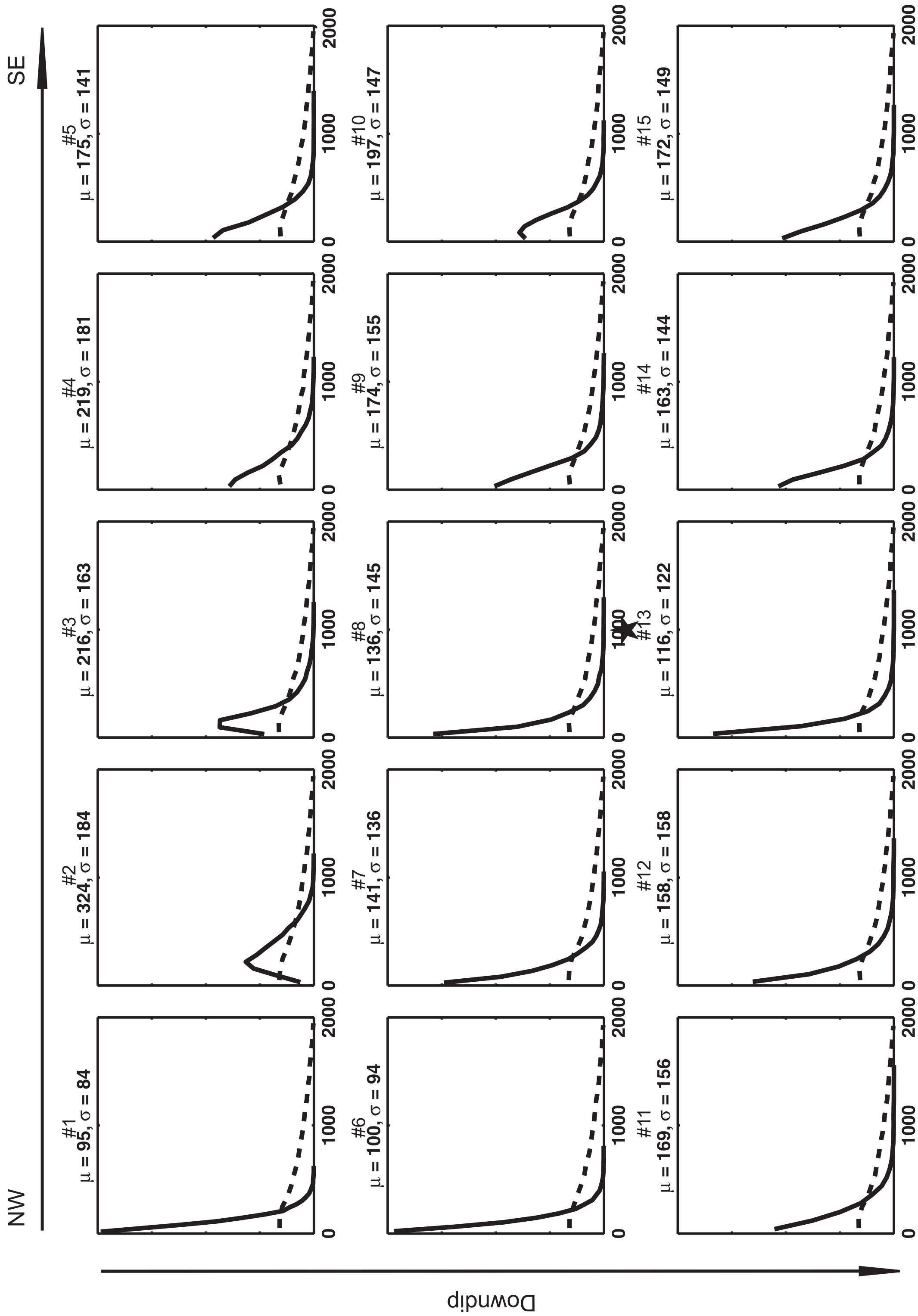

Figure 4.6: 1D marginals for final slip (cm). Same notation as in Fig 4.2

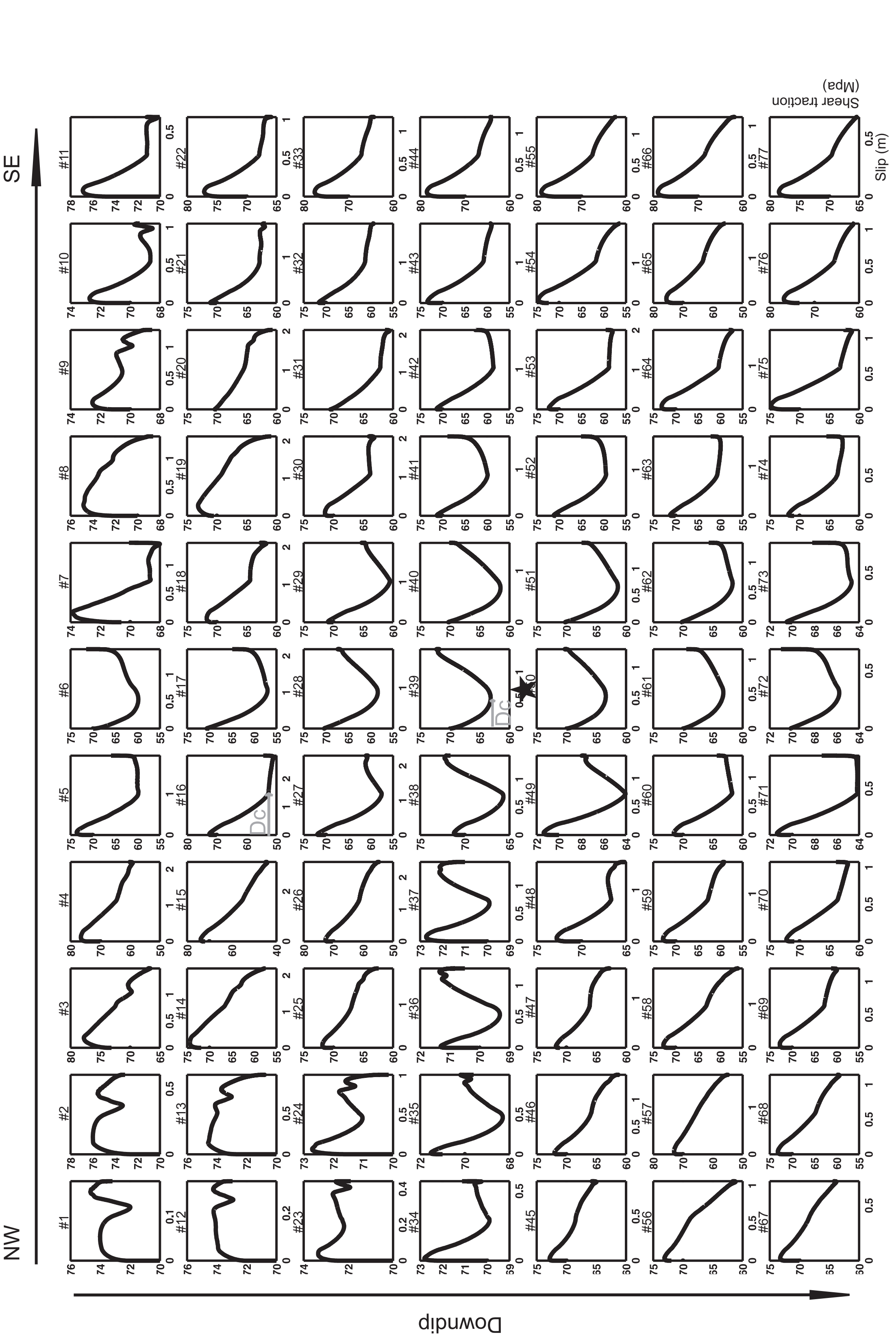

Figure 4.7: Shear traction (MPa) versus slip (m) at a 2 by 2 km fault grid points. Only the inner nodes are shown. The gray arrows indicate examples of estimated slip-weakening distances (D_C).

Node (SGSN) method to simulate the fault rupture [Dalguer & Day, 2007]. We use a grid spacing of 100 m and a time step of 0.00625 s, and map the slip model into the finite difference grid using bicubic interpolation. We simulate a time window of 20 s, applying the same velocity model used by Monelli et al. [2009].

In Fig.4.7 we show the computed shear traction versus slip curves on a 2 by 2 km grid on the fault surface, for inner grid nodes only. From each curve we visually estimate strength excess, dynamic stress drop, and slip-weakening distance. We define the slip-weakening distance as the amount of slip corresponding to a change in the traction weakening rate. To clarify this approach, we show two examples. At node 39, near the hypocenter, we can identify a clear minimum in the traction vs. slip curve. We identify the slip-weakening distance as the slip corresponding to the minimum. At node 16, located where the highest slip is inferred, we can identify a clear change in the weakening rate at a slip value of about 1.5 m, which we assume as the local slip-weakening distance. For most of the grid nodes it's possible to identify a clear change in the traction weakening rate, and therefore to apply the described procedure to estimate the slip-weakening distance. However, for some nodes, especially for those located near the fault edges where low slip is inferred (e.g. nodes 1, 2, 12, 13, 23, 24), the traction versus slip curves appear to be rather complex. For those nodes, we assume the slip-weakening distance to be equal to the final slip.

4.4 A linear slip-weakening model

In Fig. 4.8 we show the linear slip-weakening parameters (dynamic stress drop, strength excess, slip-weakening distance) estimated from the traction vs. slip curves in Fig. 4.7, interpolated (through bicubic interpolation) on the finite difference grid ($dx = 100$ m) on the fault surface. We see that the highest dynamic stress drop (about 15 MPa) is located at the same locations where the highest slip/slip-velocity is inferred. Significant dynamic stress drop is located also SE of the hypocenter. The strength excess pattern results to be very close to zero in a narrow region extending from the bottom to the top edge of the fault and centered around the hypocenter. A region of low strength-excess is located also SE of the hypocenter. The slip-weakening distance distribution results to be correlated with the final slip. The highest value is reached where the highest final slip is inferred. Slip-weakening distance values vary mostly between 0.5 and 1.5 m. In Fig. 4.8 (d) we show the resulting fracture energy density distribution.

To perform the dynamic rupture simulation we assume the upper yield stress to be uniform on the fault surface. The normal stress is assumed equal to 125 MPa (a representative value for effective normal stress for crustal earthquakes, Rice [2006]). The static friction coefficient is assumed equal to 0.85 (from Byerlee's law at low normal stress, Scholz [2002]). The upper yield stress is therefore 106.25 MPa. The initial stress is given by the upper yield stress minus the strength excess. This implies that regions of low strength excess match with regions of pre-stress close to the yield stress, and therefore near to a critical state.

We start the numerical rupture simulation by means of a circular nucleation patch centered on the hypocenter. By trial and error, we found that a nucleation patch of radius equal to 0.8 km and subject to an applied stress of 109.3 MPa, provide the best temporal alignment between the predicted and observed strong motion data.

The resulting slip-velocity temporal evolution is depicted in Fig. 4.9. We identify three main phases. In the initial phase, soon after the breaking of the nucleation patch, the rupture quickly expands (with low slip-velocities), mostly toward SE and toward the bottom edge of the fault. This initial expansion phase stops at about 1.5 s. In the second phase (from about 1.5 to 3 s), the rupture keeps growing, but with low rupture velocity and still with low slip-velocities (few tens of cm/s). In the third phase, after about 3 s, the rupture accelerates, and reaches the highest slip-velocities toward SE and the top edge of the fault (peak slip-velocity of about 2 m/s). We see also that NW of the hypocenter the rupture propagate with lower slip-velocities (about 0.5 m/s).

The peak slip-velocity distribution [Fig: 4.10 (a)] is consistent with the results of the Bayesian analysis. We see that near and NW of the hypocenter the rupture develops with low peak slip-velocities (of the order of 0.5 m/s or less). The highest slip-velocities are reached in the SE section of the fault (about 1 m/s) and below the top edge of the fault (about 2 m/s). The final slip distribution [Fig: 4.10 (a)] shows a maximum value of about 2.5 m, between 4 and 6 km depth. We observe an elongation of the slip distribution also to SE, whereas NW of the hypocenter we find the lowest values of slip. The rise time distribution (computed at each grid point as the time interval between 10 and 90 percent of the final slip) [Fig: 4.10 (c)] shows a pattern where long rise times (maximum value about 6 s) are located near the hypocenter, and then decrease approaching the edges of the fault. The rupture time distribution (computed at each grid point as the time when the slip-velocity exceeds a value of 1 mm/s) [Fig: 4.10 (c)] shows an initial phase during which the rupture propagates fast (until about 1.5 s), then slows-down (from 1.5 to 3-3.5 s), and then accelerates again.

To test the validity of the dynamic model we compare the predicted ground motion with the observed strong motion and GPS data, and with the predictions of the best-fitting kinematic model found during the sampling procedure for the Bayesian analysis. In Fig. 4.11 we compare the ground velocity predicted by the dynamic and the best-fitting kinematic models with the observed one, at a set of four near-field stations. These stations are the only included in the computational domain used for the dynamic rupture simulation. For this set of stations, we see that the dynamic model produces almost the same level of fit of the best-fitting kinematic model. For the fault normal component of station SMN015, the dynamic model can reproduce the observed waveform even better than the kinematic model. We also compute the surface static offset at a set of four stations (654, 660, 379, and 381, Fig. 4.12). At stations 654, and 660 the horizontal displacement vectors produced by the dynamic model reproduce the observations inside the error ellipses. However, at stations 379

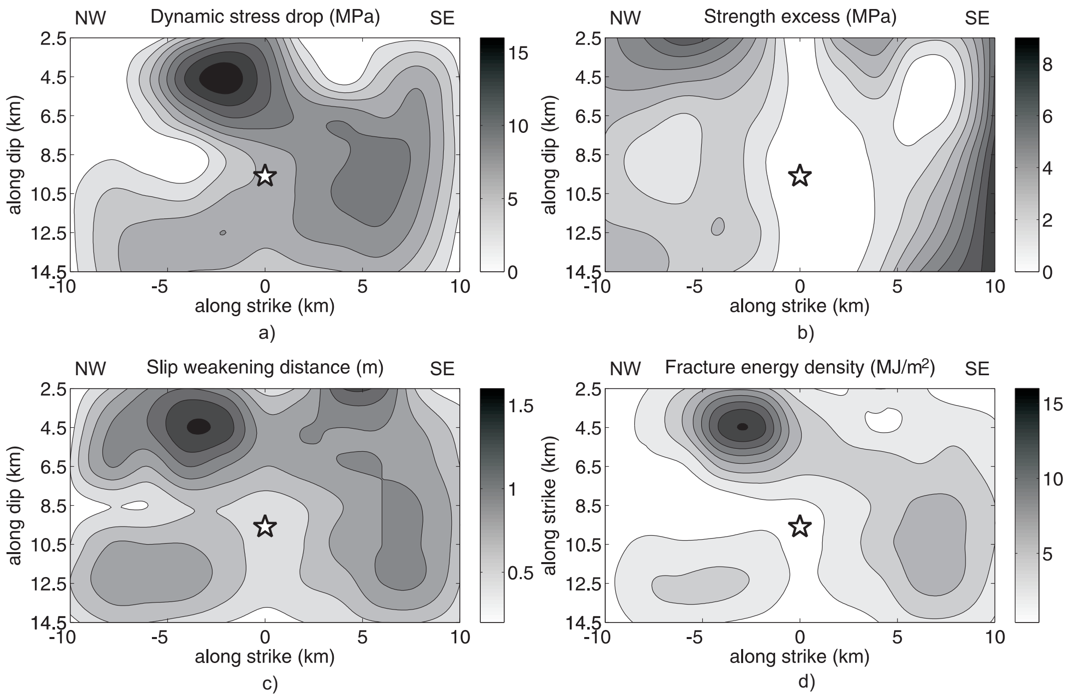

Figure 4.8: Dynamic stress drop (a), strength excess (b), and slip-weakening distance (c) estimated from traction vs. slip curves in Fig. 4.7 and interpolated on the fault surface. We show also the corresponding fracture energy density distribution (d).

and 381, the dynamic model predictions lie outside the error ellipses, although we do not observe large discrepancies.

4.5 Discussion and conclusions

Peyrat & Olsen [2004] performed a dynamic inversion for the 2000 Western Tottori earthquake, using a direct search method based on the Neighbourhood algorithm. They consider a linear slip-weakening fault model, and assume uniform upper yield stress and slip-weakening distance (equal to 28 cm). They search for the on-fault distribution of dynamic stress drop, which is allowed to vary between -2 and 5 MPa at each subfault. The best-fitting model shows a slip pattern extending from the hypocenter to the top edge of the fault (at 1 km depth), where the maximum slip (about 2 m) is reached. The maximum slip-velocity is about 0.5 m/s, and the maximum stress drop is 5 MPa.

Although the model by Peyrat & Olsen [2004] produces a satisfactory level of fit in the considered frequency range (0.05-0.5 Hz), it differs with what is usually shown in kinematic images. First of all, there is no evident asymmetry of the slip pattern with respect to the hypocenter, that is no elongation of slip toward SE. This feature is shown in all published kinematic images (Semmane et al. [2005], Festa & Zollo [2006], Piatanesi et al. [2007], Monelli et al. [2009]), and also confirmed in

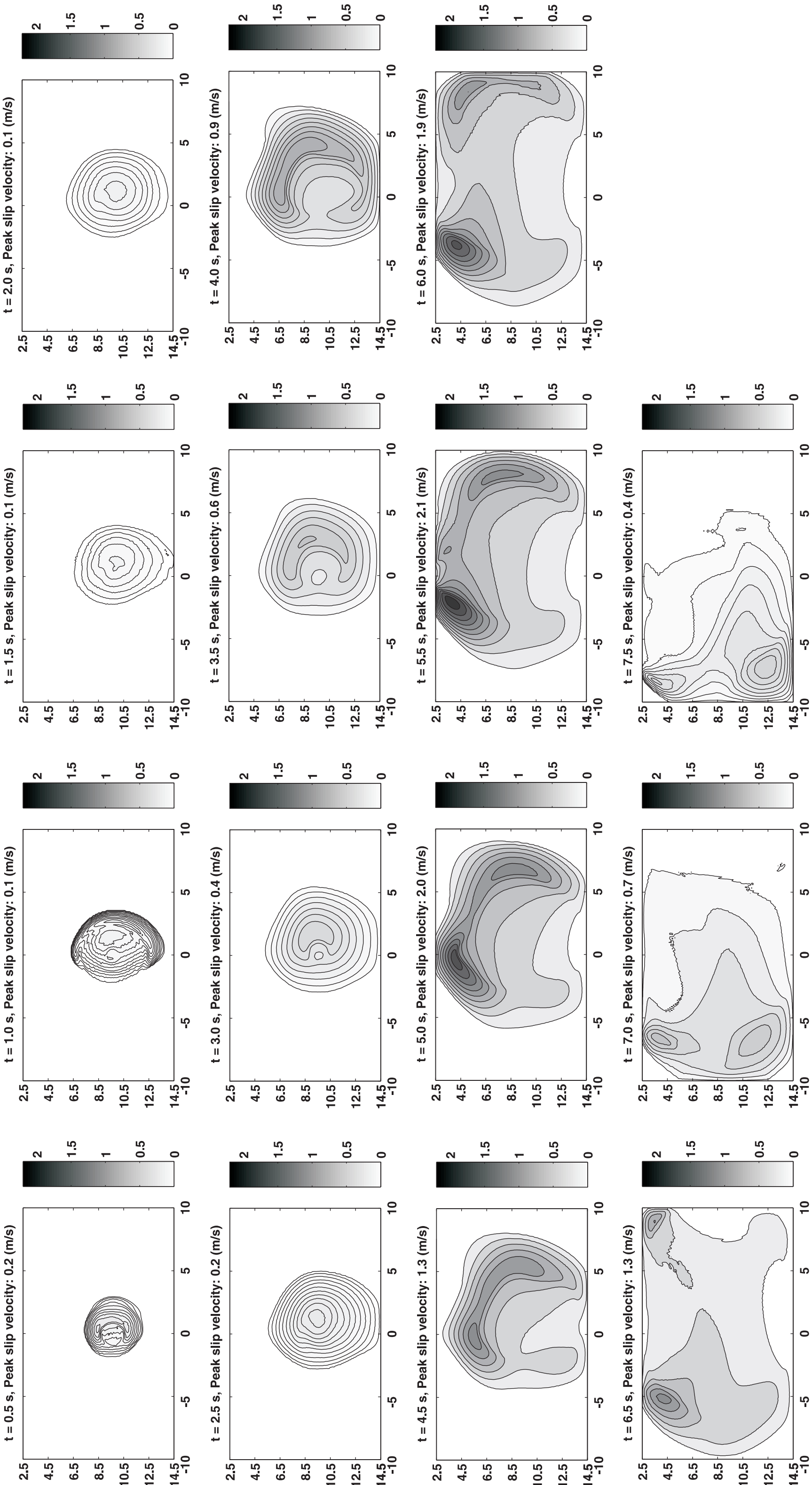

Figure 4.9: Slip-velocity evolution (m/s) resulting from the estimated dynamic rupture parameters.

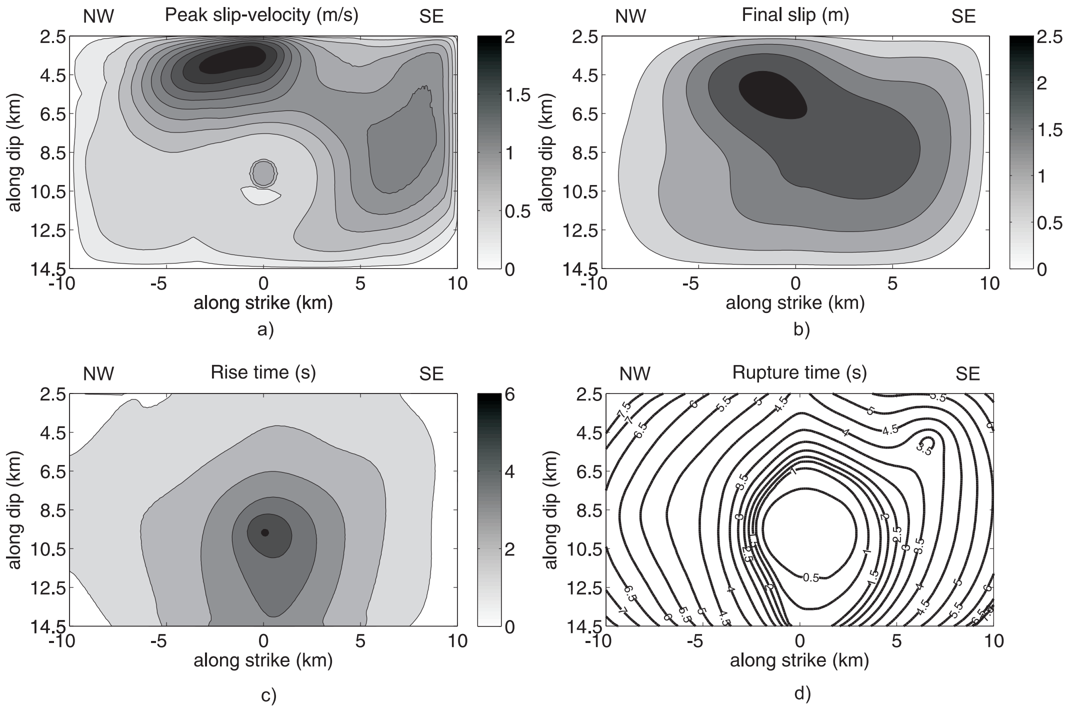

Figure 4.10: Peak slip-velocity (m/s), final slip (m), rise time (s), and rupture time (s) distributions, resulting from dynamic rupture simulation.

this study. The maximum slip-velocity is less than what estimated in this study and by Piatanesi et al. [2007] (about 2 m/s). The maximum stress-drop is lower than what we infer (about 15 MPa) and what computed by Dalguer et al. [2002] (about 30 MPa) from a kinematic image of the rupture process.

Differently to the model proposed by Peyrat & Olsen [2004], the linear slip-weakening model we derive in this study does not assume a uniform slip-weakening distance. Moreover, it can explain better what is usually observed in kinematic images. More importantly, it has been obtained without an explicit optimization procedure but rather interpreting a mean kinematic slip model using a dynamically consistent source time function. For the considered set of strong motion stations, we show that the dynamic model performs practically at the same level of the best-fitting kinematic model. For the considered set of GPS stations, the dynamic model is not able to reproduce all the observations inside the error bars, however we do not see large discrepancies.

We acknowledge that to better understand how well the dynamic model is able to explain the observations, a larger number of strong motion and GPS stations should be considered. We plan to perform this analysis as a future work. Moreover, the fact the static offset of two of four GPS stations cannot be fitted inside the 95 percent confidence level may indicate that the rupture model can still be improved. The dynamic model we derived can be easily used as a starting model for a gradient based optimization procedure.

Estimating dynamic parameters from past earthquakes is necessary to derive re-

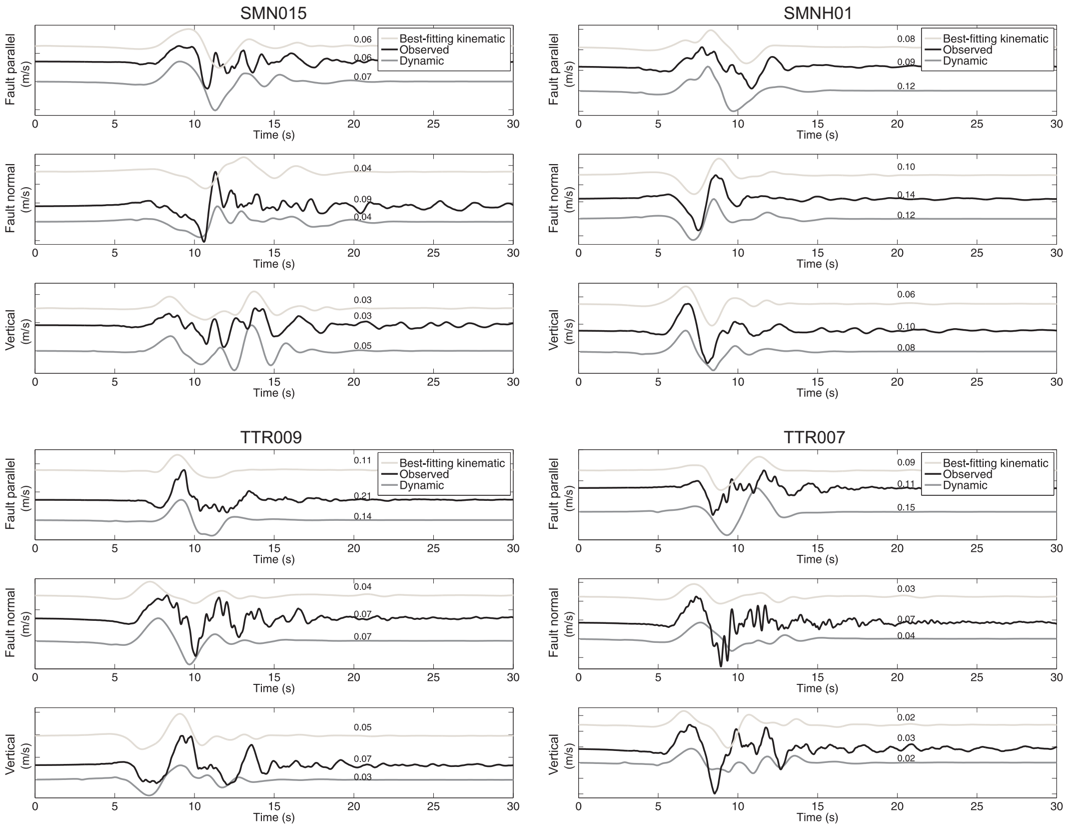

Figure 4.11: Near-field ground velocity predicted by the best-fitting kinematic model (light gray) and dynamic model (dark gray) compared with the observed one (black).

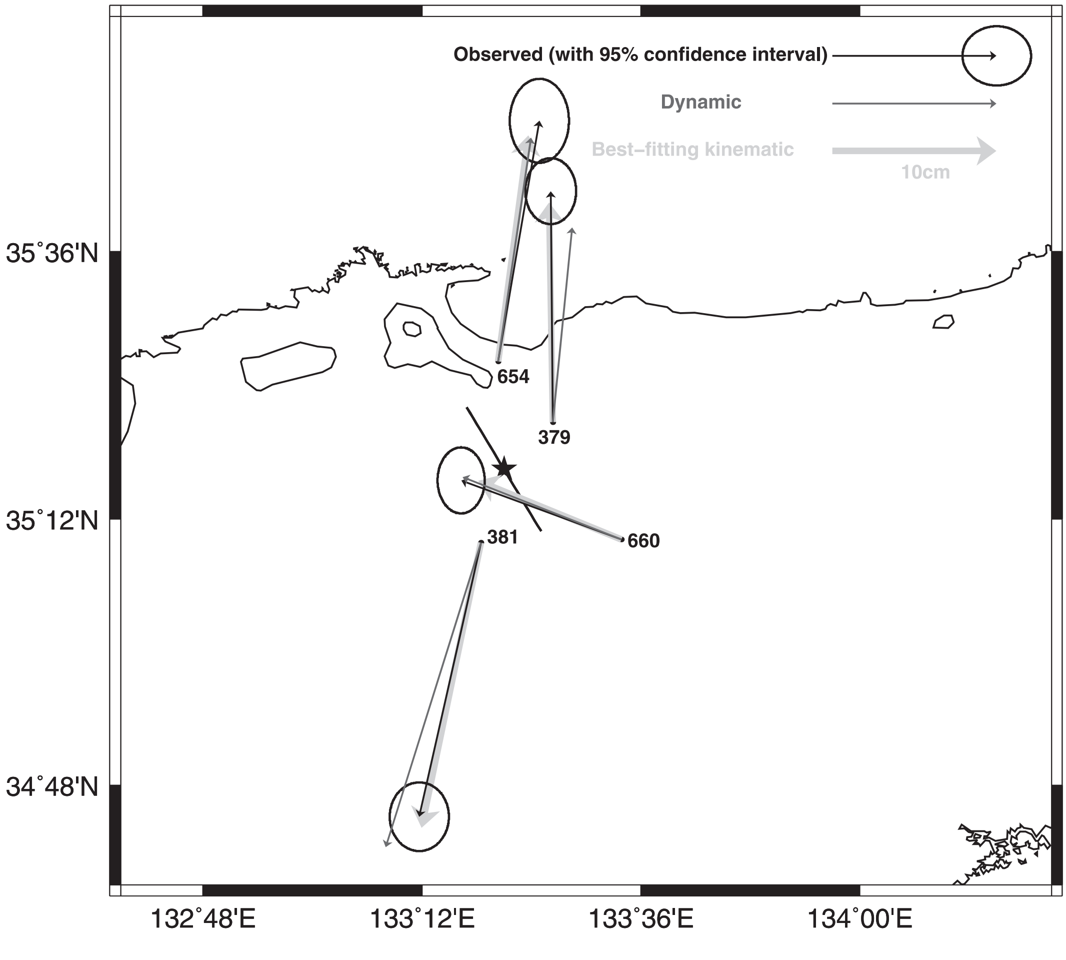

Figure 4.12: Surface coseismic offsets predicted by the best-fitting kinematic model (thick light gray) and dynamic model (thin dark gray) compared with the observed ones (black). The limited computational domain used for the dynamic rupture simulation allowed us to compute surface displacements only at stations 654, 660, 379, and 381.

alistic dynamic rupture models for ground motion simulations of future earthquakes. Dynamic rupture simulations are computationally expensive and therefore systematic dynamic inversions are still of limited applicability. It is important therefore to derive strategies helping in inferring dynamic rupture parameters, limiting the number of dynamic rupture simulations, and at the same time limiting the number of assumptions (e.g. allowing slip-weakening distance to be heterogeneous). Our study shows that using a mean kinematic slip model (representing the most likely features of the rupture process) and a dynamically consistent source time function may help in deriving a dynamic model which, without trial and error modifications, produce a level of fit which is comparable to that of a best-fitting kinematic model.

Conclusions and Outlook

Conclusions

In this thesis I present a methodology for the estimation of kinematic earthquake source parameters based on a Bayesian approach. The main benefit of using a Bayesian approach is that it allows to give comprehensive estimate of errors associated with kinematic rupture parameters taking into account the full non-linearity of the problem. From uncertainty estimates for kinematic parameters I also provide uncertainty estimates for dynamic parameters. In the following I summarize the main findings of each study.

In Chapter 1 I use the Bayesian approach to infer kinematic rupture parameters by fitting strong motion waveforms produced by a synthetic rupture model. By using an optimization algorithm, it is shown explitly how multiple rupture models are able to reproduce the observed waveforms within the same level of fit, suggesting therefore that the solution of the inversion should not be expressed in terms of a single model but rather as a set of models which show certain statistical properties. I show how in general inferences on rupture parameters cannot be expressed in terms of Gaussian probability density functions, rendering the usual characterization of uncertainties in terms of mean values and standard deviations not correct. I also show that an optimization algorithm cannot be used to estimate uncertainties, because the set of models found by optimization do not reflect the topology of the misfit function.

In Chapter 2 I consider a real event: the 2000 Western Tottori earthquake. Kinematic parameters are inferred by fitting strong motion and GPS data. Inference results indicate that the best resolved feature of the rupture process is a major slip patch located between the hypocentre and the top edge of the fault. The presence of this shallow slip patch is common to all previous studies. In contrast to some previous studies no significant slip is identified at the bottom of the fault. I also compare inferences from both strong motion and GPS data with inferences derived from strong motion data only. In both cases the shallow slip patch is identified. At other locations, the main effect of the GPS data is in reducing the probability associated with high values of slip. GPS data reduce the presence of spurious fault slip and therefore strongly influence the resulting final seismic moment.

In Chapter 3 I investigate how the estimation of dynamic parameters is affected by uncertainties in the kinematic source model. Considering the 2000 Western Tottori earthquake, I select an ensemble of kinematic models obtained through Bayesian inference which are consistent with the observed strong motion and GPS data. For each model of this ensemble the spatio-temporal evolution of on-fault stress is computed. I statistically analyse resolution of static stress drop. I find that on the same locations where stable high slip is inferred, frequency distributions of static stress drop values have an approximately Gaussian shape with positive mean values indicating that on average these locations undergo a weakening process. However, standard deviation values are of the same order of magnitude of the estimated mean values indicating therefore large uncertainties on the actual intensity of static stress drop. I show how these large uncertainties are due to a correlation between stress drop values which is inherited from a correlation between slip values. This shows how the statistical properties of the uncertainties affecting kinematic parameters are mapped into the estimation of dynamic parameters. Despite the difficulty in constraining the rupture process locally on the fault, I find that a global quantity like radiated energy can be well inferred instead.

In Chapter 4 I derive a linear slip-weakening model for the 2000 Western Tottori earthquake by using a mean kinematic slip model, and a dynamically consistent source time function (regularized Yoffe function). I obtain a dynamic rupture model able to reproduce the observed kinematic parameters. I compare the predicted ground motion with the near-field strong motion and GPS data. I find that the level of fit provided by the dynamic model is comparable to that of the best-fitting kinematic model. I consider this result of particular practical importance, because the dynamic model has been obtained without an explicit optimization procedure.

Outlook

The wavefield generated by an earthquake rupture in the real Earth is a complex signal: its analysis can potentially provide detailed knowledge of the physics of the earthquake source, however even state-of-the-art inversion methods can only extract a small portion of the information contained in real waveforms.

The major limitation in imaging the details of the earthquake rupture comes from the narrow frequency band (0-1 Hz) which can be used for waveform fitting. This is due to the often very poor knowledge of the velocity structure surrounding the earthquake source, and to the large computational demand required by numerical wave propagation simulations at high frequencies. With the frequency band limitation, the spatial resolution that can be achieved on the rupture process is of the order of kilometers.

The modeling of the earthquake source is another important factor especially for the quality of the rupture parameter estimates. Ideally, a dynamic description of the rupture process is preferable over a kinematic one. A dynamic modeling allows to generate spatio-temporal evolutions of slip which satisfy, at least, very basic physical laws. Kinematic models do not satisfy any physical constrain in general, and given the little information that band limited waveforms can provide, there can be many kinematic models compatible with the same earthquake. Again, the large computational demand required by dynamic rupture simulations put a strong pratical limit in the use of this approach for estimating rupture parameters.

With the present limitations, kinematic inversions are the only effective tool to image the earthquake rupture. Despite the fact that kinematic source inversions started almost 30 years ago (beginning of the 80s), the kinematic imaging of the earthquake source is a problem which is not yet fully solved. First of all, the non-linearity of the problem has been taken into account only in a very approximate way up to now (most of the time by providing a best-fitting model obtained using a non-linear optmization algorithm with very crude uncertainty estimations). The large discrepancies between source images for the same earthquake provided by different and indipendent studies show that this is not enough. Without a careful quantification of the parameter uncertainties it is not possible to understand which features of the rupture process are well constrained and which are not, or how different data sets contributes in constraining rupture parameters.

The Bayesian approach proposed in thesis offers a possible way to image the earthquake rupture taking into account the full non-linearity of the problem and to give comprehensive estimates of parameter uncertainties. To better achieve these goals, several improvements can be foreseen.

Imaging the earthquake source by using a Bayesian approach explicitly shows that inferring rupture parameters implies combining prior information (independent of the measured data), with information extracted from observations. Two key quantities must be therefore defined: the prior PDF, quantifing our prior knowledge on model parameters, and the likelihood function, expressing how well a given model explains the observations.

In this thesis, the prior PDF has been always assumed to be uniform over the model space. With this approach, the parameters defining the prior PDF are the minimum and maximum value for each model parameter. This implies that a good knowledge of plausible values for each parameter is known before the inversion. However, this may not be always possible. For instance, in Chapter 2, it can be seen that for rupture parameters like rise time and rupture time (Fig. 2.11, Fig. 2.12) posterior marginals are skewed towards the maximum allowed value, which suggest that the solution is actually located outside the imposed search space. In order to avoid the definition of a maximum allowed value, for which prior information may not be available, the use of prior PDFs whitout "hard" boundaries is an advantage. An example of PDF with "soft" boundaries, and which can be suitable for defining prior information for parameters which are only constrained to be positive, is the log-normal PDF. The main property of a log-normal PDF is that the logarithm of the variable has a normal (Gaussian) probability density. When the dispersion parameter goes to infinity, the log-normal distribution tends to a log-uniform distribution, impling that the logarithm of the variable has a uniform distribution. The use of a log-normal PDF avoids therefore the definition of a maximum allowed value, and by considering a large dispersion parameter, a large range of values can be tested.

The prior PDF can also be used to introduce physical constraints in the inverse problem. By defining specific prior PDFs for each fault location and by introducing correlations between neighbouring parameters it is possible to define more physically consistent source models. A possible way to derive a dynamically consistent a priori information is by using a Monte Carlo approach. Given a certain fault geometry and velocity structure, given a certain hypocenter locations, it is possible to generate an ensamble of dynamic rupture models (for instance by using heterogenous initial stress distributions), whose statistical properties can be used as prior information to constrain kinematic parameters.

Together with the prior information, the posterior PDF requires the definition of the likelihood function which quantifies how well a model explains the observations. As expressed in Eq 1.2, the likelihood function should take into account the uncertainties in both data and forward modeling.

In this thesis, the likelihood function used in the analysis of the Tottori earthquake quantifies the "quality" of a model only in terms of the L_2 norm of the difference $(observations - predictions)$. Uncertainties were not included in the calculation of the data misfit for ground motion waveforms because of limited knowledge of both data and modeling errors. Developing strategies for the estimation of uncertainties in both data and modeling would be therefore a significant improvement towards a more correct computation of the data misfit function.

When fitting strong ground motion waveforms, uncertainties in data (due for instance to seismic noise) are usually negligible with respect to uncertainties in forward modeling. The latter are responsible for most of the misfit and can be both aleatory (e.g. due to intrinsic uncertainties in the estimation of wave velocities), and epistemic (e.g. due to an insufficient knowledge of the velocity model). Therefore, together with velocity model uncertainties, the proper computation of the likelihood function requires removing epistemic uncertaintis from data. The use of 3D velocity models which can take into account 3D path effects and site effect is therefore high desirable in this regard. A more realistic modeling can be also achieved by using empirical Green's functions. If reliably estimateed, empirical Green's functions may also help in expanding the frequency band used for waveform fitting and potentially provide better resolution on the earthquake rupture process.

List of Tables

List of Figures

Bibliography

Aki, K. & Richards, P. G., 2002. *Quantitative Seismology*, Universitary Science Books, Sausalito, California.

Beeler, N. M., Tullis, T. E., & Weeks, J. D., 1994. The roles of time and displacement in the evolution effect in rock friction, *Geophys. Res. Lett.*, **21**, 1987–1990.

Beresnev, I. A., 2003. Uncertainties in Finite-Fault Slip Inversions: To What Extent to Believe? (A Critical Review), *Bull. Seism. Soc. Am.*, **93**, 2445–2458.

Beroza, G. C. & Spudich, P., 1988. Linearized inversion for fault rupture behavior: application to the 1984 Morgan Hill, California, earthquake, *J. Geophys. Res.*, **93**, 6275–6296.

Beyer, H. G., 2001. *The Theory of Evolution Strategies*, Springer, Berlin, Heidelberg.

Bouchon, M., 1997. The state of stress on some faults of the San Andreas system as inferred from near-field strong motion data., *J. Geophys. Res.*, **102**, 11,731–11,744.

Bouchon, M., Tosöz, N., Karabulut, H., Bouin, M.-P., Dietrich, M., Aktar, M., & Edie, M., 2000. Seismic Imaging of the 1999 Izmit (Turkey) Rupture Inferred from the Near-Fault Recordings., *Geophys. Res. Lett.*, **27**, 3013–3016.

Chester, F. M. & Chester, J. S., 1998. Ultracataclasite structure and friction processes of the Punchbowl fault, san Andreas system, California, *Tectonophysics*, **295**, 199–221.

Chester, F. M., Evans, J. P., & Biegel, R., 1993. Internal structure and weakening mechanism of the San Andreas fault, *J. Geophys. Res.*, **98**, 771–786.

Cocco, M. & Tinti, E., 2008. Scale dependence in the dynamics of earthquake propagation: Evidence from seismological and geological observations, *Earth Planet. Sci. Lett.*, **273**, 123–131.

Cocco, M., Spudich, P., & Tinti, E., 2006. On the Mechanical Work Absorbed on Faults During Earthquake Ruptures, in *Earthquakes: Radiated Energy and the Physics of Faulting*, vol. 157, pp. 237–254, eds Abercrombie, R., McGarr, A., Di Toro, G., & Kanamori, H., Geophysical Monograph Series.

Cohee, B. P. & Beroza, G, C., 1994. A comparison of two methods for earthquake source inversion using strong motion seismogram, *Ann. Geof.*, **XXXVII**, 1515–1538.

Corish, S. M., Bradley, C. R., & Olsen, K. B., 2007. Assessment of a Nonlinear Dynamic Rupture Inversion Technique Applied to a Synthetic Earthquake, *Bull. Seism. Soc. Am.*, **97**(3), 901–914.

Cotton, F. & Campillo, M., 1995. Frequency domain inversion of strong motions: application to the 1992 Landers earthquake, *J. Geophys. Res.*, **100**, 3961–3975.

Custodio, S., Liu, P., & Archuleta, R. J., 2005. The 2004 $M_W 6.0$ Parkfield, California, earthquake: Inversion of near-source ground motion using multiple data sets, *Geophys. Res. Lett.*, **32**(L23312), 10.1029/2005GL024417.

Dalguer, L. A. & Day, S. M., 2007. Staggered-grid split-node method for spontaneous rupture simulation., *J. Geophys. Res.*, **102**, doi:10.1029/2006JB004467.

Dalguer, L. A., Irikura, K., Zhang, W., & Riera, J. D., 2002. Distribution of Dynamic and Static Stress Changes during 2000 Tottori (Japan) Earthquake: Brief Interpretation of the Earthquake Sequences; Foreshocks, Mainshock and Aftershocks, *Geophys. Res. Lett.*, **29**, doi:10.1029/2001GL014333.

Day, S., 1982. Three-dimensional simulation of spontaneous rupture: the effect of nonuniform prestress, *Bull. Seism. Soc. Am.*, **72**, 1881–1902.

Delouis, B., Giardini, D., Lundgren, P., & Salichon, J., 2002. Joint inversion of InSAR, GPS, Teleseismic, and Strong-Motion data for the spatial and temporal distribution of earthquake slip: Application to the 1999 Izmit mainshock, *Bull. Seism. Soc. Am.*, **92**, 278–299.

Di Toro, G., Goldbsby, D. L., & Tullis, T., 2004. Friction falls toward zero in quartz rock as slip velocity approaches seismic rates, *Nature*, **427**, 436–439.

Dieterich, J. H., 1979. Modeling of rock friction. 1. Experimental results and constitutive equations, *J. Geophys. Res.*, **84**, 2161–2168.

Emolo, A. & Zollo, A., 2005. Kinematic source parameters for the 1989 Loma Prieta earthquake from the nonlinear inversion of accelerograms, *Bull. Seism. Soc. Am.*, **3**, 981–994.

Favreau, P. & Archuleta, R. J., 2003. Direct seismic energy modeling and application to the 1979 Imperial Valley earthquake, *Geophys. Res. Lett.*, **30**, doi:10.1029/2002GL015968.

Festa, G. & Zollo, A., 2006. Fault slip and rupture velocity inversion by isochrone backprojection, *Geophys. J. Int.*, **166**, 745–756.

Fialko, Y., Sandwell, D., Simons, M., & Rosen, P., 2005. Three-dimensional deformation caused by the Bam, Iran, earthquake and the origin of shallow slip deficit., *Nature*, **435**, 295–299.

Fukuyama, E., Ellsworth, W. L., Waldhauser, F., & Kubo, A., 2003. Detailed Fault Structure of the 2000 Western Tottori, Japan, Earthquake Sequence, *Bull. Seism. Soc. Am.*, **93**, 1468–1478.

Gardner, G. H. F., Gardner, L. W., & R., G. A., 1974. Formation velocity and density-the diagnostic basics for stratigraphic traps, *Geophysics*, **39**(6), 770–780.

Goldsby, D. L. & Tullis, T. E., 2002. Low frictional strenght of quarts rocks at subseismic slip rates, *Geophys. Res. Lett.*, **29**, 1844.

Gouveia, W. P. & Scales, J. A., 1998. Bayesian seismic waveform inversion: Parameter estimation and uncertainty analysis, *J. Geophys. Res.*, **103**(B2), 2759–2779.

Graves, R. W. & Wald, D. J., 2001. Resolution analysis of finite fault source inversion using one- and three-dimensional Green's functions 1. Strong motions, *J. Geophys. Res.*, **106**(B5), 8745–8766.

Guatteri, M. & Spudich, P., 2000. What Can Strong-Motion Data Tell Us about Slip-Weakening Fault-Friction Laws?, *Bull. Seism. Soc. Am.*, **90**(1), 98–116.

Hartzell, H. S. & Heaton, T. H., 1983. Inversion of strong ground motion and teleseismic waveform data for the fault rupture history of the 1979 Imperial Valley, California, earthquake, *Bull. Seism. Soc. Am.*, **73**, 1553–1583.

Hartzell, S., Liu, P., & Mendoza, C., 1996. The 1994 Northridge, California, earthquake:investigation of rupture velocity, rise time, and high-frequency radiation, *J. Geophys. Res.*, **101**, 20,091–20,108.

Hartzell, S., Liu, P., Mendoza, C., Ji, C., & Larson, K. M., 2007. Stability and Uncertainty of Finite-Fault Slip Inversions: Application to the 2004 Parkfield, California, Earthquake, *Bull. Seism. Soc. Am.*, **97**(6), 1911–1934.

Ide, S. & Takeo, M., 1997. Determination of constitutive relations of fault slip based on seismic wave analysis., *J. Geophys. Res.*, **102**, 27,379–27,391.

Ide, S., Takeo, M., & Yoshida, Y., 1996. Source Process of the 1995 Kobe Earthquake: Determination of Spatio-Temporal Slip Distribution by Bayesian Modeling, *Bull. Seism. Soc. Am.*, **86**, 547–566.

Ide, S., Beroza, G. C., & McGuire, J. J., 2005. Imaging Earthquake Source Complexity, in *Seismic Earth: Array Analysis of Broadband Seismograms*, vol. 157, pp. 117–135, eds Levander, A. & Nolet, G., Geophysical Monograph Series.

Izutani, Y. & Kanamori, H., 2001. Scale-dependence of seismic energy-to-moment ratio for strike-slip earthquakes in Japan, *Geophys. Res. Lett.*, **28**, 4007–4010.

Jin, A. & Fukuyama, E., 2005. Seismic Energy for Shallow Earthquakes in Southwest Japan, *Bull. Seism. Soc. Am.*, **95**(4), 1314–1333.

Liu, P. & Archuleta, R. J., 2004. A new nonlinear finite fault inversion with three-dimensional Green's functions: Application to the 1989 Loma Prieta, California, earthquake, *J. Geophys. Res.*, **109**(B02318), 10.1029/2003JB002625.

Ma, S. & Archuleta, R. J., 2006. Radiated seismic energy based on dynamic rupture models of faulting, *J. Geophys. Res.*, **111**, doi:10.1029/2005JB004005.

Ma, S., Custodio, S., Archuleta, R. J., & Pengcheng, L., 2008. Dynamic modeling of the 2004 M_W 6.0 Parkfield, California, earthquake, *J. Geophys. Res.*, **113**, doi:10.1029/2007JB005216.

Madariaga, R., Olsen, K., & Archuleta, R., 1998. Modeling Dynamic Rupture in a 3D Earthquake Fault Model, *Bull. Seism. Soc. Am.*, **88**(5), 1182–1197.

Mai, P. M. & Beroza, G. C., 2002. A spatial random filed model to characterize complexity in earthquake slip, *J. Geophys. Res.*, **107**, doi:10.1029/2001JB000588.

Martinez, W. L. & Martinez, A. R., 2002. *Computational Statistics Handbook with MATLAB*, Chapman and Hall/CRC, Boca Raton, Florida.

Menke, W., 1989. *Geophysical data analysis: discrete inverse theory*, Academic press, San Diego, California.

Monelli, D. & Mai, P. M., 2008. Bayesian inference of kinematic earthquake rupture parameters through fitting of strong motion data, *Geophys. J. Int.*, **173**(1), 220–232.

Monelli, D., Mai, P. M., Jónsson, S., & Giardini, D., 2009. Bayesian imaging of the 2000 Western Tottori (Japan) earthquake through fitting of strong motion and GPS data, *Geophys. J. Int.*, **176**(1), 135–150.

Mosegaard, K. & Sambridge, M., 2002. Monte carlo analysis of inverse problems, *Inverse Problems*, **18**, R29–R54.

Mosegaard, K. & Tarantola, A., 1995. Monte carlo sampling of solutions to inverse problems, *J. Geophys. Res.*, **100**(B7), 12,431–12,447.

Ohnaka, M. & Yamashita, T., 1989. A cohesive zone model for dynamic shear faulting based on experimentally inferred constitutive relation and strong motion source parameters, *J. Geophys. Res.*, **94**, 4089–4104.

Olsen, K. B., Day, S. M., Minster, J. B., Cui, Y., Chourasia, A., Faerman, M., Moore, R., Maechling, P., & Jordan, T., 2006. Strong shaking in Los Angeles expected from southern San Andreas earthquake, *Geophys. Res. Lett.*, **33**, L07305,doi:10.1029/2005GL025472.

Olsen, k. B., Day, S. M., Minster, J. B., Cui, Y., Chourasia, A., Okaya, D., Maechling, P., & Jordan, T., 2008. TeraShake2: Spontaneous Rupture Simulations of M_W 7.7 Earthquakes on the Southern San Andreas Fault, *Bull. Seism. Soc. Am.*, **98**(3), 1162–1185.

Olsen, K. B., Day, S. M., Dalguer, L. A., Mayhew, J., Cui, Y., Zhu, J., Cruz-Atienza, V., Roten, D., Maechling, P., Jordan, T. H., Okaya, D., & Chourasia, A., 2009. ShakeOut-D: Ground Motion Estimates Using an Ensemble of Large Earthquakes on the Southern San Andreas Fault With Spontaneous Rupture Propagation, *submitted to Geophys. Res. Lett.*.

Olson, H. A. & Apsel, R. J., 1982. Finite faults and inverse theory with applications to the 1979 Imperial Valley earthquake, *Bull. Seism. Soc. Am.*, **72**, 1969–2001.

Peyrat, S. & Olsen, K. B., 2004. Nonlinear dynamic rupture inversion of the 2000 Western Tottori, Japan, earthquake, *Geophys. Res. Lett.*, **31**(L05604), 10.1029/2003GL019058.

Peyrat, S., Olsen, K., & Madariaga, R., 2001. Dynamic modeling of the 1992 Landers earthquake, *J. Geophys. Res.*, **106**, 26,467–26,482.

Piatanesi, A., Tinti, E., & Cocco, M., 2004. The dependence of traction evolution on the earthquake source time function adopted in kinematic rupture models, *Geophys. Res. Lett.*, **31**(L04609), 10.1029/2003GL019225.

Piatanesi, A., Cirella, A., Spudich, P., & Cocco, M., 2007. A global search inversion for earthquake kinematic rupture history: application to the 2000 western Tottori, Japan earthquake, *J. Geophys. Res.*, **112**(B07314), 10.1029/2006JB004821.

Rice, R. J., 2006. Heating and weakening of faults during earthquake slip, *J. Geophys. Res.*, **111**, doi:10.1029/2005JB004006.

Rivera, L. & Kanamori, H., 2005. Representations of the radiated energy in earthquakes, *Geophys. J. Int.*, **162**, 148–155.

Sagiya, T., 2004. A decade of GEONET:1994-2003-The continuous GPS observation in Japan and its impact on earthquake studies-, *Earth Planets Space*, **56**, xxix–xli.

Salichon, J., Delouis, B., Lundgren, P., Giardini, D., Costantini, M., & Rosen, P., 2003. Joint inversion of broadband teleseismic and interferometric synthetic apertur radar (InSAR) data for the slip history of the mw=7.7, Nazca ridge (Peru) earthquake of 12 november 1996, *J. Geophys. Res.*, **108**(B2,2085, 10.1029/2001JB000913).

Sambridge, M., 1999. Geophysical inversion with a neighbourhood algorithm-ii. Appraising the ensemble, *Geophys. J. Int.*, **138**, 727–746.

Scholz, C. H., 2002. *The Mechanics of Earthquake and Faulting*, Cambridge University Press, Cambridge, UK.

Sekiguchi, H. & Iwata, T., 2002. Rupture process of the 1999 Kocaeli, Turkey, Earthquake Estimated from Strong-Motion Waveforms, *Bull. Seism. Soc. Am.*, **92**, 300–311.

Sekiguchi, H., Irikura, K., & Iwata, T., 2000. Fault Geometry at the Rupture Termination of the 1995 Hyogo-ken Nambu Earthquake, *Bull. Seism. Soc. Am.*, **90**, 117–133.

Semmane, F., Cotton, F., & Campillo, M., 2005. The 2000 Tottori earthquake: A shallow earthquake with no surface rupture and slip properties controlled by depth, *J. Geophys. Res.*, **110**(B03306), 10.1029/2004JB003194.

Sen, M. & Stoffa, P. L., 1995. *Global Optimization Methods in Geophysical Inversion*, Elsevier, Amsterdam, The Netherlands.

Spudich, P. & Archuleta, R., 1987. Techniques for earthquake ground motion calculation with applications to source parametrization of finite faults, in *Seismic strong motion synthetics*, vol. 37, pp. 205–265, ed. Bolt, B. A., Academic Press, Orlando, Florida.

Spudich, P. & Xu, L., 2002. *Documentation of software package Compsyn sxv3.11: programs for earthquake ground motion calculation using complete 1-D Green's functions*, Academic Press, San Diego, California.

Tarantola, A., 2005. *Inverse Problem Theory and Methods for Model Parameter Estimation*, Society for Industrial and Applied Mathematics, Philadelphia.

Tinti, E., Fukuyama, E., Piatanesi, A., & Cocco, M., 2005a. A Kinematic Source-Time Function Compatible with Earthquake Dynamics, *Bull. Seism. Soc. Am.*, **95**, 1211–1223.

Tinti, E., Spudich, P., & Cocco, M., 2005b. Earthquake fracture energy inferred from kinematic rupture models on extended faults., *J. Geophys. Res.*, **110**, doi:10.1029/2005JB003644.

Umeda, Y., 2002. The 2000 western Tottori earthquake, *Earth Planets Space*, **54**, iii–iv.

Vallee, M. & Bouchon, M., 2004. Imaging coseismic rupture in far field slip patches, *Geophys. J. Int.*, **156**, 615–630.

Wald, D. J. & Graves, R. W., 2001. Resolution analysis of finite fault source inversion using one- and three-dimensional Green's functions 2. Combining seismic and geodetic data, *J. Geophys. Res.*, **106**(B5), 8767–8788.

Wald, D. J. & Heaton, T. H., 1994. Spatial and Temporal Distribution of Slip for the 1992 Landers, California, Earthquake, *Bull. Seism. Soc. Am.*, **84**, 668–691.

Wald, D. J., Helmberger, D. V., & Heaton, T. H., 1991. Rupture model of the 1989 Loma Prieta earthquake from the inversion of strong motion and broadband data, *Bull. Seism. Soc. Am.*, **81**, 1540–1572.

Wald, D. J., Heaton, T. H., & Hudnut, K. W., 1996. The Slip History of the 1994 Northridge, California, Earthquake Determined from Strong-Motion, Teleseismic, GPS, and Leveling Data, *Bull. Seism. Soc. Am.*, **86**, S49–S70.

Wibberly, C. A. J. & Shinamoto, T., 2003. Internal structure and permeability of major strike-slip fault zones: The Median Tectonic Line in Mid Prefecture, Southwest Japan, *J. Struct. Geol.*, **25**, 59–78.

Woessner, J., Schirlemmer, D., Wiemer, S., & Mai, P. M., 2006. Spatial correlation of aftershock locations and on-fault main shock properties, *J. Geophys. Res.*, **111**, doi:10.1029/2005JB003961.

Curriculum Vitae

PERSONAL INFORMATION

Surname/First name: Monelli Damiano

Address: Friesenbergstrasse 28, 8055 Zurich, Switzerland

E-mail: monelli@tomo.ig.erdw.ethz.ch

Nationality: Italian

Date of birth (dd/mm/year): 09/07/1981

Status: married since 26/04/2008

EDUCATION

***2005–2009*:** Doctoral student, Inst. of Geophysics, ETH Zurich, Switzerland

***October 2005*:** Laurea in Fisica at the Universita' degli Studi di Bologna (Italy), with points 110/110 cum Laude.

***July 2000*:** Diploma di maturita' scientifica at the Liceo Scientifico "T.C.Onesti" of Fermo (Italy), with points 94/100.

LANGUAGES

***Italian*:** Mother tongue.

***English*:** Fluent.

***German*:** Basic.

COMPUTING SKILLS

***Programming languages*:** good knowledge of C++ and parallel computing with MPI.

***Operating systems*:** good knowledge of Windows and Linux.

***Application software*:** good knowledge of Matlab, Latex, Word, Excel, PowerPoint.

PUBLICATIONS

Monelli, D. and Mai, P.M., 2008. Bayesian inference of kinematic earthquake rupture parameters through fitting of strong motion data, *Geophysical Journal International*, Volume 173, Number 1, April 2008, pp.220-232.

Monelli, D., Mai, P.M., Jonsson, S. and Giardini, D., 2009. Bayesian imaging of the 2000 Western Tottori (Japan) earthquake through fitting of strong motion and GPS data, *Geophysical Journal International*, Volume 176, Number 1, January 2009, pp.135-150.

PARTECIPATION TO CONFERENCES

***December 2008*:** *American Geophysical Union*, S.Francisco, USA.
-Monelli, D., Dalguer, L. A., and Mai, P. M. "Estimating dynamic source parameters from an uncertain rupture model: application to the 2000 Western Tottori (Japan) earthquake". Poster presentation.

***September 2007*:** Workshop on *Numerical Modeling of Earthquake Source Dynamics*, Smolonice Castle, Slovak Republic.
-Monelli, D., and Mai, P. M. "Non-linear source inversion and Bayesian inference for a synthetic test case and the 2000 Western Tottori earthquake". Oral presentation.

***April 2007*:** *European Geoscience Union*, Vienna, Austria.
-Monelli, D., and Mai, P. M. "The 2000 Western Tottori earthquake imaged through inversion of strong motion data". Poster presentation.
-Monelli, D., and Mai, P. M. "Bayesian estimation of kinematic earthquake source parameters through non-linear inversion of strong motion data". Poster presentation.

***July 2006*:** *SPICE (Seismic wave Propagation and Imaging in Complex media: a European framework)* research and training workshop, Kinsale, Ireland.
-Monelli, D., and Mai, P. M. "Non-linear kinematic inversion of a fault rupture using an Evolutionary Algorithm". Poster presentation.

Acknowledgments

Dear reader, I know this page is at the end of the thesis, but I hope you start reading from here. If something useful or interesting is written in this thesis, it's also due to the people I mention here.

First of all I would like to say thanks to Prof. Giardini. He gave me the opportunity to do my Ph.D. at ETH, and therefore made possible the reaserch presented in this work. I'm also grateful for some comments concerning my first results on the Tottori earthquake. The suggestion of expanding the limits of the search space revealed to be fruitful to get more clear and general results.

I want to thank Martin Mai for supervising me. Under his supervision I've never felt like under-pressure. He gave me all the time to follow my interests and a lot of freedom in choosing my research strategy. Thanks for his optimism about my work, which greatly helped me in overcoming difficult times, especially at the beginning of my Ph.D., during which things seemed not to work at all. Thanks also for his comments, for reviewing the articles, and for non-scientific chats.

Thanks to Sigurjon Jónsson. During these years I could appreciate his rigorous attitude in science, and I benefited from it when he reviewed my work. Thanks for useful discussions about error estimates and also for the nice parties in his giant balcony (and for a ride on his Audi TT)!

The third and fourth chapters of the thesis could not be possible without the important contribution of Luis Angel Dalguer. Thanks for the time spent in explaining me how to use the SGSN code, and for discussions about rupture dynamics. Thanks also for the live-music bar in S.Francisco, great place!

When I started my Ph.D. there were much less Italians in the istitute than now: Fabio, Gabriele, Erica, Lapo. Altough limited in number, they made my transition from Italy to Switzerland less dramatic than expected. Thanks!

A “BIG” thanks also to all my German office-mate: Gregor, Johannes, Falko, Henriette. Without them I would be still trying to translate letters written in German! Thanks for your patience and kindness!

Thanks to all people together with I share time in and out of the institute: Banu, Valerio, Matteo, Marta, Walter, Corinne, Manuele, Julie, Julia, Steve, Ilaria.

Thanks to my parents. Thanks for their help, for traveling about 800 km to visit me in Zurich, for always preparing a warm welcome when I'm back.

Finally, thanks to Chiara, my wife. Thanks for having accepted to share her life with me: the most precious gift she could ever made.